3.4 Cooperative Phenomena in Complex Macroscopic Systems

Molecular Simulation Contributions to Biological Membrane and Energy Materials Research

Wataru SHINODA

Research Institute for Interdisciplinary Science, Okayama University

3-1-1 Tsushima-naka, Kita-ku, Okayama 700-8530

In the past fiscal year, our research group leveraged high-performance computing to tackle fundamental questions in biomembrane dynamics, drug delivery, and energy materials via molecular simulations. Our findings, published in ten peer-reviewed articles, highlight how computational modeling reveals mechanisms that are experimentally challenging to access.

A significant achievement was the extension of the pSPICA coarse-grained force field to include polar water and protein models, enabling accurate simulations of electrostatically sensitive biological events such as membrane pore formation and peptide adsorption. This allowed the reproduction of systems like melittin-induced pores and polyarginine adsorption [1]. In parallel, we combined solid-state NMR and simulations to explore lipid-protein interactions, showing how lipid headgroups modulate membrane structure near bacteriorhodopsin [2]. Another study revealed the structure of Amphotericin B-ergosterol channels using isotope labeling and MD simulations, identifying a stable, seven-membered ion-conducting complex that explains antifungal specificity [3].

We also investigated structural changes in lipid carriers during processing. Time-resolved SAXS and MD simulations showed ethanol-induced transitions from unilamellar to multilamellar liposomes, informing nanoparticle formulation strategies [4]. Building on this, we developed a photoresponsive molecule that induces reversible membrane disruption for intracellular delivery of macromolecules, validated experimentally and through simulations [5].

In energy research, we modeled ether-based electrolytes for lithium–sulfur batteries, identifying how subtle structural changes impact ion transport and polysulfide suppression [6]. Another study screened solvate electrolytes with novel anionic structures, achieving high lithium transference numbers nearing 0.9 [7].

In diagnostics, we developed a nanowire-based device that distinguishes miRNA sources via thermal profiling, offering a new route for cancer-related biomarker analysis [8]. We also designed a ZnO nanowire platform that selectively captures unmethylated DNA, aiding

in epigenetic profiling [9]. Lastly, atomistic simulations of photoswitchable lipid bilayers revealed how light-induced phase transitions modulate membrane properties for controlled drug release [10].

These studies underscore the critical role of molecular simulations, enabled by supercomputing, in advancing both fundamental science and practical applications. In the future, we aim to integrate multiscale modeling and AI-driven simulations to further enhance predictive power and experimental synergy.

References

[1] Y. Miyazaki and W. Shinoda, J. Chem. Inf. Model. **64**, 532 (2024).

[2] Y. Umegawa, S. Kato, S. Sangjae, W. Shinoda, S. Kawatake, S. Matsuoka, and M. Murata, Biophys. Chem. **308**, 107204 (2024).

[3] Y. Umegawa, H. Tsuchikawa, W. Shinoda, M. Murata, Org. Biomol. Chem. **23**, 1233 (2025).

[4] M. Maeki et al., Nanoscale Adv. **6**, 2166 (2024).

[5] W. Huo et al., J. Mater. Chem. B, **12**, 4138 (2024).

[6] T. Ishikawa et al., Faraday Discuss. **253**, 385 (2024).

[7] F. Philippi et al., Chem. Sci. **15**, 7342 (2024).

[8] K. CHattrairat et al., Device, **2**, 100363 (2024).

[9] M. Musa et al., Lab Chip, **25**, 1637 (2025).

[10] K. A. Alberto, MN. H. Begam, H. Xiong, W. Shinoda, P. A. Slesinger, Z. Qin, S. O. Nielsen, Nanoscale, **17**, 2032 (2025).

Low-rank tensor ring decomposition and its application to renormalization group

Naoki KAWASHIMA

Institute for Solid State Physics,

The University of Tokyo, Kashiwa-no-ha, Kashiwa, Chiba 277-8581

Artificial intelligence and machine learning has started deeply influencing our daily lives. Compression of tensor-type data is one of the core parts of machine learning. Being closely related to information extraction and classification, it is a technological element with a very high social need. Recently, it has been widely acknowledged that the data compression can be essential also in extracting the critical information from the tensor network representation of various field theoretical models in both continuous and discrete spaces. Numerical methods based on the tensor network representation are now developing a bridge between condensed matter theory and information science.

In [1], we generalized our own method for computing the elementary excitation. The same task had been carried out by extremely cumbersome book-keeping that required a lot of human time and often leads to programming errors. We applied the new method to the S=1/2 J1-J2 model to obtain the dynamical properties of the putative gapless spin liquid phase. This opens up a new avenue of lattice model studies directly comparable to real experiments.

In [2], we studied the model system of cold atoms characterized by the dipole-dipole interaction. We discovered many distinct phases with various spatial patters, e.g., the stripe and kinked phases. There are multiple candidates for the spatial patterns in the classical level. Some of the phases emerge from the quantum "order-by-disorder" effect that lifts the classical degeneracy by the quantum fluctuation.

The information-compression efficiency of the tensor network methods are best represented in their application to real-space renormalization group method. In [3], we revisited the nature of the real-space renormalization group mappings. We focused on the question whether the common real-space RG really retains the fundamental critical information of the system. It is well-known that the fixed-point system of the decimation map is the trivial. On the other hand, the fixed point system of the majority map is not trivial. However, it had not been known whether this fixed point has the same universality as the original model. In [3], we found that the majority map is faithful, i.e., by its repeated application, the system transforms to a fixed

point system that retains all the critical information as the original one.

In [4], we directly addressed the problem of efficient low-rank decomposition of given tensors. In the previous works aiming at a similar goal, such as the loop-TNR and GILT, the redundant representation is compressed through repeated application of contractions and decompositions guided by the intuition based on the physical picture of "redundant loops". In [3], we adopted the nuclear norm regularization, developed in the field of the data science. It was surprizing to see that the new methods based on very different guiding principles produced the results with the same level of the accuracy.

In [5], we investigated the finite-temperature phase diagram of the classical J_1 - J_2 XY model on a square lattice using a tensor network method. Our study reveals an emergent intermediate phase, which is characterized by a Z_2 long-range stripe order without phase coherence in the XY spins, sandwiched by two transitions; a higher-temperature Ising transition and a lower-temperature Berezinskii-Kosterlitz-Thouless (BKT) transition. We also observed that, in smaller J_2 region, two transitions merge into a single first-order phase transition, which had not been predicted before.

In [6], we propose a multi-impurity method for the bond-weighted tensor renormalization group (BWTRG) to compute the higher-order moments of physical quantities in two dimensions. We demonstrate that the accuracy of the proposed method is much higher than the conventional tensor renormalization group for the Ising model and the five-state Potts model. We found that BWTRG with the optimal hyperparameter is more efficient in terms of computational time than alternative approaches based on the matrix product state in estimating the critical temperature.

References

[1] Wei-Lin Tu, Laurens Vanderstraeten, Norbert Schuch, Hyun-Yong Lee, Naoki Kawashima, and Ji-Yao Chen: Physical Review X Quantum 5, 010335 (2024)

[2] Huan-Kuang Wu, Takafumi Suzuki, Naoki Kawashima, Wei-Lin Tu: Physical Review Research 6, 023297(1-12) (2024)

[3] Katsuya O. Akamatsu and Naoki Kawashima: Journal of Statistical Physics 191, 109 (2024)

[4] Kenji Homma, Tsuyoshi Okubo, Naoki Kawashima: Physical Review Research 6, 043102 (1-9) (2024)

[5] Feng-Feng Song, Hanggai Nuomin, and Naoki Kawashima: Physical Review B 111, 104428 (2025)

[6] Satoshi Morita and Naoki Kawashima: Physical Review B 111, 054433 (2025)

Molecular dynamics analysis of ultrasound cavitation

Yuta Asano

Faculty of Global Nursing

Iryososei University, 1-3-4, Koaota, Kashiwa, Chiba 277-0803

When a liquid is irradiated with ultrasound waves, bubbles are generated due to local depressurization. The bubble formation phenomenon is called ultrasound cavitation. Ultrasonic cavitation is a safe and environmentally friendly technology that is applied in various fields, including not only engineering but also food processing, and medical care [1-3]. However, the analysis of ultrasound cavitation is challenging because of the complexity of the multiscale-multiphysics phenomenon. A direct analysis of the interaction between the phase transition and the sound field under non-equilibrium conditions is essential for understanding ultrasonic cavitation. We have been studying the mechanism of ultrasonic cavitation generation and its physical and chemical effects using molecular dynamics (MD) simulations.

Effective transportation of bubbles is necessary for efficient use of the physical and chemical effects of ultrasound cavitation [4]. In FY2024, we performed MD simulations of vortex rings involving cavitation bubbles. Because vortex rings have a propulsive force in the axial direction of the ring, the bubble ring efficiently transports cavitation bubbles. In this study, the bubble ring is generated by large-scale MD simulations, and the formation process is analyzed. In addition, the stability and moving behavior of the bubble ring were also investigated.

The system is composed of monatomic molecules, and the intermolecular interaction is the Lennard-Jones potential. The dimension of the system is $L_x \times L_y \times L_z = 5000\sigma \times 2000\sigma \times 2000\sigma$, where σ is the molecular diameter. The number of liquid atoms in the system is 11,986,332,544, and the liquid is equilibrated near the boiling point. The two walls were placed at $x = 0$ and 5000σ, respectively. For the bubble ring formation, an orifice plate with a hole whose diameter is $D = 800\sigma$ is placed at $x = 250\sigma$. When the wall at $x = 0$ moves toward the positive x-direction, the vortex ring and phase transition occur due to the jet. Bubble rings appear when the vortex ring entrains the cavitation bubbles.

Figures 1(a) and 1(b) show density fields near the bubble rings generated at low and high amplitudes, respectively. Cavitation bubbles generated when passing through the orifice plate are entrained in the vortex ring. The bubble ring then appears. The size of the bubble

ring increased with increasing amplitude. In addition, the shape is distorted for the larger amplitude. The bubble ring moved at an almost constant velocity. We found that a stable bubble ring is generated by the MD simulation containing 10 billion atoms.

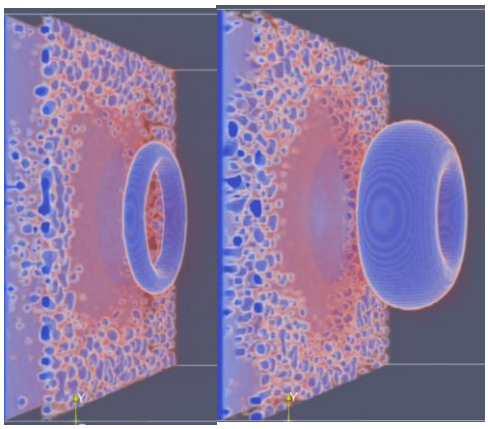

Fig. 1: Density fields of bubble ring simulations.

References

[1] Y. Yao, Y. Pan, and S. Liu, Ultrason. Sonochem. **62**, 104722 (2020).

[2] S. Kentish and H. Feng, Annu. Rev. Food Sci. Technol. **5**, 263 (2014).

[3] Z. Izadifar, P. Babyn, and D. Chapman, J. Med. Biol. Eng. **39**, 259 (2019).

[4] Z. Wang, Z. Shi, L. Liu, Chem. Eng. J. 465 143070 (2023).

Looking at bare transport coefficients in fluctuating hydrodynamics

Hiroyoshi NAKANO
Institute for Solid State Physics, University of Tokyo
Kashiwa-no-ha, Kashiwa, Chiba 277-8581

The Navier-Stokes equation quantitatively describes macroscopic fluid motion, accurately predicting behaviors ranging from streamlined flow over airplane wings to complex turbulence. However, at the mesoscopic scale, significant fluctuations necessitate incorporating noise terms for an accurate description. This leads to the framework of fluctuating hydrodynamics [1].

The fundamental equations of fluctuating hydrodynamics in d dimensions are:

$$\frac{\partial \rho}{\partial t} = -\nabla \cdot (\rho \boldsymbol{v}) \tag{1}$$

$$\rho \left[\frac{\partial \boldsymbol{v}}{\partial t} + (\boldsymbol{v} \cdot \nabla)\boldsymbol{v} \right] = -\nabla p + \eta_0 \nabla^2 \boldsymbol{v} + \left[\zeta_0 + \left(1 - \frac{2}{d} \right) \eta_0 \right] \nabla(\nabla \cdot \boldsymbol{v}) - \nabla \cdot \boldsymbol{\Pi}^{\mathrm{ran}} \tag{2}$$

Here, $\rho(\boldsymbol{r}, t)$, $\boldsymbol{v}(\boldsymbol{r}, t)$, and $p(\boldsymbol{r}, t)$ are the density, velocity, and pressure fields, respectively. The pressure p is a function of density and temperature, $p = p(\rho, T)$, determined by thermodynamics. $\boldsymbol{\Pi}^{\mathrm{ran}}(\boldsymbol{r}, t)$ is the stochastic momentum flux representing thermal fluctuations due to the random motion of constituent particles (e.g., atoms or molecules). Without $\boldsymbol{\Pi}^{\mathrm{ran}}(\boldsymbol{r}, t)$, Eq. (2) reduces to the standard Navier-Stokes equation. $\boldsymbol{\Pi}^{\mathrm{ran}}(\boldsymbol{r}, t)$ is typically modeled as Gaussian white noise with the correlation:

$$\left\langle \Pi_{ij}^{\mathrm{ran}}(\boldsymbol{r}, t) \Pi_{mn}^{\mathrm{ran}}(\boldsymbol{r}', t') \right\rangle = 2 k_B T \Delta_{ijmn} \delta^d(\boldsymbol{r} - \boldsymbol{r}') \delta(t - t') \tag{3}$$

with

$$\Delta_{ijmn} = \eta_0 \left(\delta_{im}\delta_{jn} + \delta_{in}\delta_{jm} \right) + \left(\zeta_0 - \frac{2}{d}\eta_0 \right) \delta_{ij}\delta_{mn} \tag{4}$$

Fluctuating hydrodynamics is characterized by the noise term $\boldsymbol{\Pi}^{\mathrm{ran}}(\boldsymbol{r}, t)$ and the associated bare transport coefficients (η_0, ζ_0), which govern mesoscopic dissipation and transport. The bare coefficients differ fundamentally from the macroscopic transport coefficients found in the deterministic Navier-Stokes equation. For instance, in two-dimensional (2D) fluids, macroscopic coefficients are known to exhibit logarithmic divergence with increasing system size [2]. In contrast, the bare coefficients (η_0, ζ_0) are expected to be constants determined by microscopic properties such as atomic structure, temperature, and density (or pressure).

Fluctuating hydrodynamics provides the fundamental framework for describing the coupling between fluid flow and thermal fluctuations. However, major challenges remain: how do the bare transport coefficients manifest in macroscopic observables, and how can their values be determined using practical methods? To date, obtaining precise values for these bare coefficients has proven challenging.

To address this challenge, we performed numerical simulations of the fluctuating hydrodynamic equations, Eqs. (1) and (2) [3]. Our simulations focus on a two-dimensional fluid confined between two parallel walls moving in opposite directions (Fig. 1(a)), creating shear

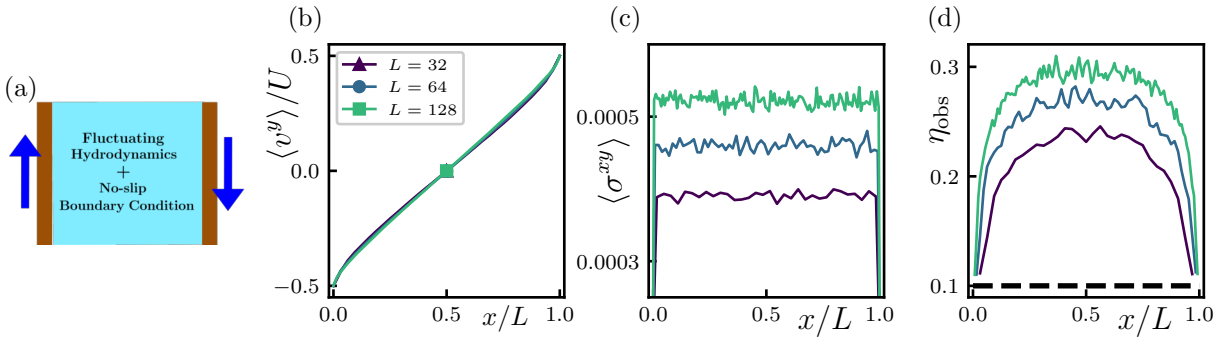

Figure 1: Simulation results for the system-size dependence of observables for Couette geometry in fluctuating hydrodynamics. Colored lines represent simulation results for different system sizes: $L = 32$ (purple), $L = 64$ (blue), and $L = 128$ (green). (a) Scaled velocity profiles $\langle v^y(x) \rangle / U$ as a function of the scaled position x/L. (b) Shear stress profiles $\langle \sigma^{xy}(x) \rangle$ as a function of x/L. (c) Observed viscosity profiles $\eta_{\rm obs}(x)$ as a function of x/L. Parameters are fixed at $\rho_0 = 0.765$, $T = 1.0$, $\eta_0 = 0.10$, $U/L = 0.002$, and $\zeta_0 = 1.0$. The pressure is given as the relation $p = c_T^2 \rho$ with $c_T^2 = 1000$ (approximating an incompressible fluid).

flow. Standard no-slip boundary conditions were applied at the walls ($x = 0, L$):

$$v^x = 0 \tag{5}$$

$$v^y = \mp U/2 \tag{6}$$

$$\partial_x \rho = 0 \tag{7}$$

Here, U is the relative wall velocity.

Figure 1(b)-(d) shows the simulation results (parameters are summarized in the figure caption). Figure 1(b) presents the time-averaged steady-state velocity profile $v^y(x)$ while Fig. 1(c) displays the corresponding shear stress profile $\langle \sigma^{xy}(x) \rangle$. In these plots, the coordinate x is normalized by the system size L, and the velocity $v^y(x)$ is normalized by $U/2$. As shown in Fig. 1(c), the shear stress $\langle \sigma^{xy}(x) \rangle$ is spatially uniform, consistent with force balance requirements.

Interestingly, Fig. 1(b) reveals that the velocity profile deviates from the linear shape expected for ideal uniform shear flow (Couette flow). This deviation from linearity can be characterized by an observed viscosity $\eta_{\rm obs}$, defined locally as:

$$\eta_{\rm obs}(x) := \frac{\langle \sigma^{xy} \rangle}{\partial_x \langle v^y(x) \rangle} \tag{8}$$

This quantity is plotted in Fig. 1(d). The figure shows that $\eta_{\rm obs}$ varies with the distance from the walls, increasing away from them. Far from the walls (in the bulk), $\eta_{\rm obs}$ exhibits system-size dependence; this bulk value is often interpreted as the macroscopic viscosity.

Remarkably, near the walls, $\eta_{\rm obs}$ closely approaches $\eta_0 = 0.10$, the input value for the bare viscosity in our simulations. This key finding suggests that the bare viscosity directly governs the fluid dynamics near the walls. We attribute this observation to the strong suppression of hydrodynamic fluctuations by the no-slip walls. Notably, similar behavior has been observed in atomic-level simulations.

Thus, our results confirm that fluctuating hydrodynamics incorporating the bare viscosity is essential for accurately predicting fluid motion near solid boundaries.

References

[1] L. D. Landau and E. M. Lifshitz, Fluid Mechanics: Volume 6 (Elsevier, 1959)

[2] D. Forster, D. R. Nelson, and M. J. Stephen, Phys. Rev. A 16, 732 (1977).

[3] H. Nakano, Y. Minami, and K. Saito, arXiv:2502.15241 (2025).

Fluctuation of a Bilayer Composed by Amphipathic Molecules

Shunta KIKUCHI and Hiroshi WATANABE
Faculty of Science and Technology, Keio University
Yokohama, Kanagawa 223-8522, Japan

We investigated the thermal fluctuation properties of bilayers composed of amphipathic molecules using molecular dynamics simulations [1]. To model these molecules, we employed a simple diatomic structure and constructed bilayers in a solvent environment. Our main objective was to analyze how membrane fluctuations depend on temperature by examining the Fourier spectrum of the membrane surface. We found that at high temperatures, the fluctuation spectrum is dominated by a q^4 dependence. This suggests that bending elasticity primarily governs the restoring force. At lower temperatures, we observed a crossover from q^4 to q^2 behavior, which indicates that interfacial tension becomes the dominant restoring force in this regime. This result complements our previous findings for monolayer membranes, where a transition from q^2 to q^4 was observed as the interfacial tension decreased [2].

To further understand the bilayer structure, we calculated radial distribution functions of the amphipathic molecules. We discovered that the molecular arrangement within the bilayer depends on temperature in the horizontal direction but remains mostly unchanged in the vertical direction. This means that bilayers preserve their membrane structure even under thermal agitation, allowing increased fluctuations primarily in-plane.

Our results highlight the distinct roles of elasticity and interfacial tension in regulating bilayer fluctuations. At high temperatures, membranes are flexible and their shape is stabilized by bending elasticity. At low temperatures, however, the membrane becomes stiffer due to the influence of interfacial tension. This temperature-dependent crossover deepens our understanding of membrane mechanics and provides a useful framework for analyzing bilayer behavior.

We also emphasize the effectiveness of using a coarse-grained model. Although all-atom simulations offer detailed insights, they are computationally demanding. Our approach achieves a balance between physical realism and computational efficiency, allowing us to focus on the essential characteristics of amphipathic self-assembly and fluctuation.

In summary, we demonstrated that the fluctuation properties of bilayers depend strongly on temperature and that the restoring forces can shift from elasticity to interfacial tension depending on the regime. We also showed that the membrane maintains structural stability while allowing enhanced fluctuations in-plane. These findings contribute to the broader understanding of bilayer dynamics and stability, which is relevant to both biological and synthetic membrane systems.

References

[1] S. Kikuchi and H. Watanabe, J. Phys. Soc. Jpn. **93**, 114601 (2024).

[2] S. Kikuchi and H. Watanabe, J. Chem. Phys., **158**, 124901 (2023).

Tensor network study on frustrated magnets

Tsuyoshi OKUBO
Institute for Physics of Intelligence, University of Tokyo
7-3-1 Hongo, Bunkyo-ku, Tokyo, 113-0033

Frustrated magnets are among the most interesting subjects in condensed matter physics. One striking effect is the emergence of a nontrivial ground state due to frustration. Typical examples are spin-liquid states, which are characterized by the absence of long-range magnetic order. Such a spin liquid state appears in the Kitaev model on the honeycomb lattice, which has a nontrivial ground state called the Kitaev spin liquid [1, 2]. The Hamiltonian of the Kitaev model is given by $\mathcal{H} = \sum_\gamma \sum_{\langle i,j\rangle_\gamma} \left(S_i^\gamma S_j^\gamma\right)$, where γ is the direction of the interaction, and $\langle i,j\rangle_\gamma$ denotes the nearest neighbor sites in the γ direction. Another example is the Kagome lattice Heisenberg model, for which the possibility of a spin-liquid ground state in zero magnetic field has been widely discussed. In addition, under the applied magnetic field, several magnetization plateaus are stabilized [3, 4]. Among them, the plateau with 1/9 of the total magnetization has been actively discussed recently.

In our project this year, we investigated properties of such frustrated spin models on two-dimensional lattices. We mainly considered two models: the $S = 1$ Kitaev model with Heisenberg and symmetric off-diagonal interactions, and the Kagome lattice Heisenberg model under magnetic fields with weak Dzyaloshinskii-Moriya (DM) interaction.

For the $S = 1$ Kitaev model with bilinear-biquadratic interactions, we have recently reported the ground state phase diagram calculated using the infinite projected entangled pair states (iPEPS) method [5]. We showed that when the Heisenberg and biquadratic interactions are properly balanced, the spin-liquid state remains stable. This balance can be interpreted as effective interactions between quadrupole degrees of freedom. Furthermore, we found that under these conditions, a direct phase transition occurs between the spin-liquid phase and a quadrupolar ordered phase —a state that lacks conventional magnetic order but exhibits a different type of symmetry breaking. This year, we extended our calculations to include the symmetric off-diagonal interaction, called Γ interaction, defined as

$$\mathcal{H}_\Gamma = \Gamma \sum_\gamma \sum_{\langle i,j\rangle_\gamma} \left(S_i^\mu S_j^\nu + S_i^\nu S_j^\mu\right), \qquad (1)$$

where (μ,ν,γ) is a cyclic permutation of (x,y,z), for example, $(\mu,\nu,\gamma) = (y,z,x)$ for the x-bond. Using the iPEPS method with bond dimensions D up to $D = 8$, we determined the phase diagram of the $S = 1$ Kitaev model with weak Γ and Heisenberg interactions to reveal the stability of the Kitaev spin liquid. We found that in the case of the Kitaev spin liquid with antiferromagnetic Kitaev interaction, the spin-liquid phase is more stable against the Γ interaction, indicating the possibility of finding the antiferromagnetic Kitaev spin-liquid state in the real compounds [6].

For the Kagome lattice Heisenberg model with weak DM interaction, we calculated finite temperature properties of a finite-size cluster using the matrix product operator (MPO) representation of the density matrix. We optimized the density operator at the inverse temperature $\beta = 1/T$ by exponential tensor renormalization group (XTRG) method [7]. In

the XTRG method, we compute the finite-temperature density matrix $\rho(\beta)$ by iteratively applying $\rho(\beta) = \rho(\beta/2)\,\rho(\beta/2)$ starting from $\beta \sim 10^{-7}$. We determined the finite-temperature states below $T \simeq 0.1$ for the Kagome lattice Heisenberg model with a weak DM interaction under several magnetic fields using the XTRG method. We confirmed that the 1/9, 1/3, 5/9, and 7/9 magnetization plateaus are stabilized at sufficiently low temperatures. We also calculated the temperature dependence of the thermal Hall conductivity around the magnetization plateaus [8]. Our preliminary results suggest that the thermal Hall conductivity exhibits characteristic temperature dependence, notably including a sign change, depending on the magnetic field. The understanding of the relationship between the thermal Hall conductivities and the nature of the plateau states is an important topic for future study.

References

[1] A. Kitaev, Ann. Phys. **321** (2006) 2.

[2] Y. Motome and J. Nasu, J. Phys. Soc.Jpn. **89** (2020) 012002.

[3] S. Nishomoto, N. Shibata, and C. Hotta, Nat. Commun. **4** (2013) 2278.

[4] R. Okuma, D. Nakamura, T. Okubo, A. Miyake, A. Matsuo, K. Kindo, M. Tokunaga, N. Kawashima, S. Takeyama and Z. Hiroi, Nat. Commun. **10** (2019) 1229.

[5] T. Mashiko and T. Okubo, Phys. Rev. Research **6** (2024) 033110.

[6] T. Mashiko and T. Okubo, in preparation.

[7] H. Li, D.-W. Qu, H.-K. Zhang, *et al.* Phys. Rev. Research **2** (2020) 043015.

[8] Y. Nakanishi, K. Ido, S. Morita, Y. Yamaji, and T. Okubo, in preparation.

Ground-state phase diagram of frustrated itinerant magnets

Kota IDO

Institute for Solid State Physics,

The University of Tokyo, Kashiwa-no-ha, Kashiwa, Chiba 277-8581

The Kitaev spin liquid has drawn attention as a platform for non-Abelian anyons, expected to be a source for topological quantum computation [1]. α-$RuCl_3$ is a promising candidate for realizing the Kitaev spin liquid because it is reported that half-integer quantized thermal Hall conductivity, expected for the Kitaev spin liquid under magnetic fields, has been observed [2]. However, this quantization appears only within a limited magnetic field range, stimulating further research for proposing other candidates and methods to realize the Kitaev spin liquid more robustly.

One strategy is the use of heterostructures. Combining Kitaev spin liquid candidates with other layered materials may enhance Kitaev interactions through strain and potentially induce novel phenomena via hybridization between conduction electrons and localized spins. Recently, heterostructures of α-$RuCl_3$ and graphene have been realized, spurring rapid progress in both experimental and theoretical studies [3, 4].

In this study, we investigated the ground state of the Kitaev-Kondo model [4], where a Kitaev spin model is coupled to a conduction electron layer via the Kondo coupling, using the variational Monte Carlo method. As the trial wave function, we employed a pair-product wave function with many-body correlation factors [5]. This wave function can accurately describe the Kitaev spin liquid. In addition, it incorporates the hybridization effect between conduction electrons and localized spins while accounting for many-body correlations beyond mean-field approximation. Our results reveal the emergence of rich ground states, including a fractionalized Fermi liquid, a magnetic ordered phase, and a Kondo insulating state. Further investigation has been ongoing, which will be reported elsewhere.

References

[1] A. Kitaev, Ann. Phys. **321**, 2 (2006).

[2] Y. Kasahara et al., Nature **559**, 227 (2018).

[3] S. Mashhadi et al., Nano Lett. **19**, 4659 (2019), B. Zhou et al., Phys. Rev. B **100**, 165426 (2019), Y. Wang et al., Nano Lett. **20**, 8446 (2020).

[4] U. F. P. Seifert, T. Meng, and M. Vojta, Phys. Rev. B **97**, 085118 (2018), W. Choi et al.,, Phys. Rev. B **98**, 155123 (2018).

[5] T. Misawa et al., Comput. Phys. Comm. **235**, 447 (2019).

Fracture process of semicrystalline polymers using large-scale simulation

Yuji HIGUCHI
Research Institute for Information Technology, Kyushu University
Motooka Nishi-ku, Fukuoka 819-0395

By molecular simulations, we have revealed the fracture processes of semicrystalline polymers [1], water dynamics around osmolytes [2], and water dynamics on the phospholipid membrane [3]. This year, we studied the delamination process of semicrystalline polymers from fillers by coarse-grained molecular dynamics simulations on systems B and C.

Semicrystalline polymers are used in automobile parts by adding fillers to improve their rigidity. On the other hand, a decrease in impact strength is a problem to be solved. The impact fracture occurs when voids are generated and grow from the interfacial delamination between the polymer and the filler. However, the delamination process is still unclear at the molecular level. We study the delamination process between the lamellae, which is a basic structure of semicrystalline polymer, and the filler by coarse-grained molecular dynamics simulations. Figure 1 shows the delamination process. In the edge-on model, where the polymer chains are oriented parallel to the filler surface, the voids grow perpendicular to the stretching direction. In the flat-on model, where the polymer chains are oriented perpendicular to the filler surface, voids grow parallel to the stretching direction. The maximum stress against the stretching is higher in the edge-on model than that in the flat-on model. The flat-on model shows that more polymer is adsorbed at high strains. We clarify the effect of differences in the orientation direction of the interfacial polymer on the delamination.

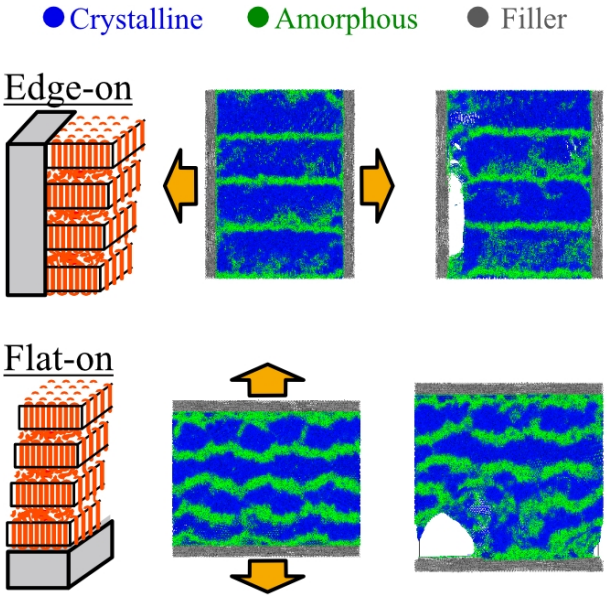

Figure 1: Coarse-grained molecular dynamics simulations on the interfacial delamination between a semicrystalline polymer and a filler in the edge-on and flat-on models.

References

[1] Y. Higuchi and G. Matsubai: Macromol. Chem. Phys. **225**, 2400076 (2024).

[2] Y. Higuchi, M. A. Saleh, T. Anada, M. Tanaka, and M. Hishida: J. Phys. Chem. B **128**, 5008 (2024).

[3] M. K. Rahman, T. Yamada, N. L. Yamada, Y. Higuchi, and H. Seto: J. Phys. Chem. B **129**, 3998 (2025).

Design of Multi-walled CNT Yarns for High-Performance CNT Yarn Composites

Go Yamamoto and Redha A. Ramadhan

Department of Aerospace Engineering, Tohoku University,

6-6-01 Aramaki-Aza-Aoba, Aoba-ku, Sendai 980-8579, Japan

We conducted simulations on approximately 180 multi-walled carbon nanotube yarn (CNTY) models using molecular dynamics (MD) simulations combined with Python-based input scripts [1]. The simulations were conducted on Supercomputer system C at ISSP. From the simulations, we obtained the nominal tensile strength of the CNTY structure with different structural parameters—The number of CNTs in the yarn was set to 3 and 7, and the number of walls ranged from 2 to 5. Both armchair and zigzag chirality were considered. The twist angle was investigated by varying the yarn twist from 0° to 30° in 5° increments. The interwall crosslink density was varied from 0% to 2.0% in 0.2% increments.

The parametric study revealed that the optimal CNTY structure is characterized by the armchair configuration, a small inner tube diameter, a large number of walls, a crosslink density exceeding 1% between each wall, and a low twist angle [1]. To verify these findings, we conducted a series of optimizations of the CNTY structural parameters using machine learning. The primary objective of the optimization was to maximize the nominal tensile strength of the CNTY. The optimization results are presented in Figure 1. Based on the optimization, the structural parameters that yield the highest nominal tensile strength correspond to the armchair-type CNTY, featuring a small inner wall diameter with a [6,6] index, only three CNTs in the yarn, and a near-zero twist angle. The optimized model consists of just two walls with no crosslink density between them.

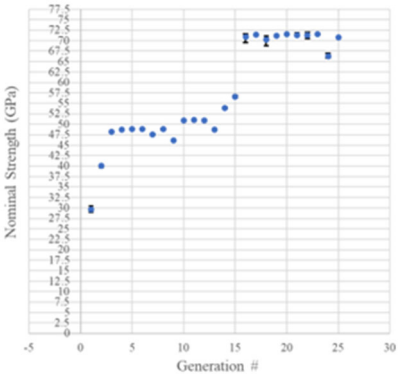

Fig. 1: Plot of the optimization generation vs the nominal strength of CNTY.

The results of this study will be reported in a manuscript. Next, we will conduct an optimization of the CNTY, focusing on the 5-wall CNTY group, with particular emphasis on crosslink density. Optimization of the 10-degree CNTY is also in progress.

References

[1] R.A. Ramadhan, C. Yu, A. Kunitomo, N. Shigemitsu, T. Shindo, G. Yamamoto, Structure-Mechanical Property Relationships in Carbon Nanotube Yarns, Solid State Phenomena 364 (2024) 3–9.

Prediction and Design of Protein Folding and Function

Masataka YOSHIMURA[1], Shunji SUETAKA[1], Koji OOKA[2], Runjing LIU[1], Shinya INOUE[1], Sae KATO[1], Shun NAGAI[3], Shunya OKADA[1], Atsuya WATANABE[1], and Munehito ARAI[1,2,3]

[1]Department of Life Sciences, Graduate School of Arts and Sciences, [2]College of Arts and Sciences, and [3]Department of Physics, Graduate School of Science, The University of Tokyo, Komaba, Meguro, Tokyo 153-8902

Proteins exert their functions after folding into specific three-dimensional structures. Therefore, elucidation of protein folding mechanisms is one of the most important issues in basic life sciences. In recent years, protein structure prediction based on deep learning methods has emerged, such as AlphaFold [1], and the development of AlphaFold was awarded the Nobel Prize in Chemistry in 2024. However, even AlphaFold cannot predict protein folding processes. We have recently developed a statistical mechanical theory called the WSME-L model that can predict folding processes for various types of proteins [2]. To investigate the applicability of this model, we applied it to various proteins to predict folding processes. In the calculations, contact energies between amino acid residues were obtained using the AMBER software [3], and the free energy landscape was calculated using in-house software written in C++ and Python. We compared the predicted results with experimental results in detail and modified the prediction methods to further improve the prediction accuracy and speed. We also tried to extend the theory to predict binding reactions between proteins.

Our WSME-L model can predict the folding reaction processes of various mutant proteins using their structures predicted by AlphaFold (LocalColabFold) [4]. We selected mutant proteins that were predicted to have a different folding pathway than the wild type. We are now investigating the folding processes of the designed proteins experimentally to verify the validity of the predictions.

Aldehyde deformylating oxygenase (ADO) is an enzyme that can synthesize alkanes equivalent to diesel oil and is expected to be useful for biofuel production; however, its activity is low and the mechanism of its function remains unresolved [5]. ADO binds to its upstream enzyme, acyl-ACP reductase (AAR), and efficiently receives aldehyde as substrate from AAR. Previous studies have proposed that ADO synthesizes alkanes upon dissociation from AAR, and the product exits through the substrate entrance [6]. To test this

hypothesis, we investigated whether the alkane product can dissociate from ADO while the AAR and ADO remain bound. Molecular dynamics (MD) simulations with the GROMACS software [7] using the Parallel Cascade Selection (PaCS) MD method [8] revealed that ADO can release the alkane product without dissociation of AAR [9]. Thus, we proposed a new model in which ADO can efficiently produce alkanes while remaining bound to AAR.

Increasing the activity of enzymes is important for the mass production of industrially useful substances. We have previously proposed a universal protocol to rationally increase the activity of enzymes using the physics-based Rosetta software [10]. In this study, we have attempted to use deep learning-based methods to improve the activities of several enzymes based on our protocol. The designed proteins were produced using *Escherichia coli* and experimental verification of their activities is ongoing.

References

[1] J. Jumper, et al.: Nature, **596**, 583-589 (2021).

[2] K, Ooka, and M. Arai: Nat. Commun. **14**, 6338 (2023).

[3] D. A. Case, et al.: AMBER 2022. University of California, San Francisco (2022)

[4] M. Mirdita, K. Schütze, Y. Moriwaki, L. Heo, S. Ovchinnikov, and M. Steinegger: Nat. Methods, **19**, 679-682 (2022).

[5] Y. Hayashi, and M. Arai: Microbial Cell Factories, **21**, 256 (2022).

[6] Y. Gao, et al.: Nat. Commun. **11**, 1525 (2020).

[7] S. Pall, C. J. Smith, B. Hess, E. Lindah: SoftwareX, **1–2**, 19-25 (2015).

[8] S. Ikizawa, et al: J. Phys. Chem. B, **128**, 3631-3642 (2024).

[9] M. Yoshimura, and M. Arai: Biophys. Physicobiol. **22**, e220003 (2025).

[10] J. K. Leman, et al.: Nat. Methods, **17**, 665 (2020).

Creating a quantum computing database for sensor materials

Wataru Mizukami

Center for Quantum Information and Quantum Biology, Osaka University, Osaka 560-0043, Japan

Quantum computers with more than a hundred qubits are now available, and the need for practical algorithms and data sets is growing. Recently, the first tests of quantum error correction on real devices have begun, which is an important step towards building useful quantum computers. Our research focuses on the development of hybrid quantum-classical methods for materials simulation, in particular for sensor materials. We are working on ways to make effective use of current quantum devices, despite their noise problems, by creating new hybrid approaches.

This year we created a quantum circuit dataset for the QM9 molecular database using Automatic Quantum Circuit Encoding (AQCE). This method allows us to convert molecular electronic structure information from exact diagonalisation into quantum circuits. By converting wave function data into quantum circuit format, we have created a useful resource for quantum machine learning with real chemical data.

We have also developed a new method called Quantum Selected Configuration Interaction (QSCI) with Auxiliary Field Quantum Monte Carlo (AFQMC), QSCI-AFQMC for short. QSCI uses quantum computers to find a key subspace and then diagonalises the electronic structure Hamiltonian in that subspace on classical computers. QSCI-AFQMC uses the QSCI wave function as the trial wave function for AFQMC calculations. We tested this method on several molecules, including H_2O and N_2, and achieved chemical accuracy on real superconducting quantum computers at Osaka University and RIKEN.

We also created a local surface energy (LSE) descriptor using neural network potentials to speed up the screening of high-entropy alloy catalysts. By applying both classical and quantum machine learning to this problem, we significantly reduced computation times while maintaining high accuracy, allowing faster exploration of possible catalysts. These advances show how quantum methods can help with practical materials research.

Thermal effects on quantum frustrated magnets

Tokuro Shimokawa
Okinawa Institute of Science and Technology Graduate University, Onna 904-0495, Japan

The properties of quantum frustrated magnets at finite temperatures remain largely unexplored, and there has been a continuous demand for advancements in research based on large-scale numerical calculations. In recent years, with the development in the field of quantum information, several quantum entanglement measures that can be experimentally measured have attracted attention. In this research project, we focused on several quantum entanglement measures that can be witnessed in experiments, and attempted to apply them to a long-standing problem of distinguishing between quantum spin liquid (QSL) and random singlet (RS) states.

As a representative example, we focused on the physics in the S=1/2 random-bond Heisenberg spin chain and J_1-J_2 random-bond triangular-lattice Heisenberg antiferromagnet. We numerically investigated the behaviors of several quantum entanglement measures such as one-tangle, two-tangle, concurrence, and quantum Fisher information, which could be measured by using inelastic neutron scattering experiments. To evaluate the quantum Fisher information at finite temperatures, we developed our non-biased numerical code based on thermal pure quantum state method to calculate the dynamical spin structure factor via real time evolution of thermal pure quantum state [1, 2]. We also have accelerated our computational code using MPI parallelization techniques, and especially, we were able to evaluate the temperature dependence of Quantum Fisher information and dynamical spin structure factor through large-scale parallel computing using F144cpu partitions. Our numerical calculations provided deep insight for understanding the entanglement natures, and qualitative difference in the temperature dependence of the quantum Fisher information could be useful to solve the identification problem in both 1D [3] and 2D [4] cases.

We also tried to study the scaling collapse in the finite-temperature dynamical spin structure factor near quantum critical point for S=1/2 J_1-J_2 triangular lattice magnet, and it's critical exponent for a triangular-lattice material, $KYbSe_2$ [5]. We succeeded in getting semi-quantitative good agreement with experiments [4].

References

[1] H. Ikeuchi, H. De Raedt, S. Bertaina, and S. Miyashita, Phys. Rev. B **92**, 214431 (2015).

[2] H. Endo, C. Hotta, and A. Shimizu, Phys. Rev. Lett. **121**, 220601 (2018).

[3] S. Sabharwal, T. Shimokawa and N. Shannon, arXiv:2407.20797.

[4] T. Shimokawa, S. Sabharwal and N. Shannon, in preparation.

[5] A. O. Scheie et al, Nat. Phys. **20**, 74 (2024).

Dynamic Modes in Active Potts Model

Hiroshi NOGUCHI
Institute for Solid State Physics, University of Tokyo

Various spatiotemporal patterns have been observed in nonequilibrium active systems. Many phenomena are well-captured by a description in terms of nonlinear but deterministic partial differential equations. However, noise effects are not understood so far. We focused on the effects of thermal fluctuations, since they are significant on a molecular scale.

We simulated the nonequilibrium dynamics of Potts models with three and four states, in square lattices [1–3] and meshless membranes [4]. A cyclic flipping energy is introduced in addition to usual nearest-neighbor interactions. Under the cyclically symmetric conditions, the cyclic changes in the dominant phases (called homogeneous cycling) and the spatial coexistence of the all phases are obtained at low and high flipping energies, respectively. In the three-state Potts model, the domains of three states form spiral waves, while waves do not have centers in the four-state Potts model. At a medium flipping energy, two modes temporally coexist, as shown in Fig. 1.

Compared with three-state cycling, the significant characteristics of four-state cycling is that there are no direct flips between the diagonal states ($s = 0$ and 2 or $s = 1$ and 3). Domains in the diagonal-state phase have a long lifetime, and the circular domains slowly shrink to reduce the domain boundary length. This spatial pattern steadily exists under asymmetric conditions. In the homogeneous cycling mode, these long-lived diagonal domains can cause the dominant phase to skip and return to the previous dominant phase. Thus, non-cyclic one-phase modes are formed through growth failure in the four-state cycling, whereas through nucleation failure in the three-state cycling.

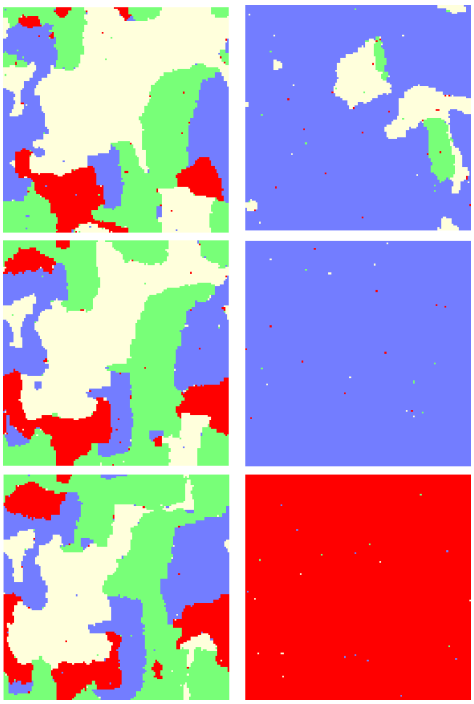

Figure 1: Sequential snapshots of the temporal coexistence of two modes in active four-state Potts model [3]. Each state is represented by a different color. Four states spatially coexist in the first three snapshots, while homogeneous cycling mode emerges in the last two snapshots.

References

[1] H. Noguchi, F. van Wijland, and J.-B. Fournier, J. Chem. Phys. 161, 025101 (2024).

[2] H. Noguchi and J.-B. Fournier, New. J. Phys. 26, 093043 (2024).

[3] H. Noguchi, Sci. Rep. 15, 674 (2025).

[4] H. Noguchi, Soft Matter 21, 1113 (2025).

Dynamical scaling study of three-dimensional XY spin glass

Y. Ozeki and Y. Terasawa
Graduate School of Informatics and Engineering, The University of Electro-Communications

We verified a method for obtaining a high-precision dynamical exponent z from the correlation length in the nonequilibrium relaxation (NER))process to analyze the $\pm J$ XY spin-glass (SG) in three dimensions. Since the Binder parameter exhibits no algebraic divergence in this system, we applied a method to estimate z by using scaling laws for the dynamical correlation function in conjunction with Gaussian process regression [1]. The obtained z yielded consistent and highly accurate results in previous studies for relatively well-studied models—specifically, the three-dimensional (3D) ferromagnetic Ising model and the 3D $\pm J$ Ising model. Building on these previous studies, we obtained highly precise critical temperatures and exponents. These findings support the spin chirality decoupling picture, explaining the experimental spin-glass phase transition.

We calculated the SG susceptibility and chiral grass (CG) susceptibility dynamically with n replicated systems. The calculations were performed with $L = 91$, $n = 256$, and 5 samples. As a result, we obtained $T_{\rm SG} = 0.396(1)$ and $T_{\rm CG} = 0.4460(6)$. In addition, the product of critical exponents $\gamma/z\nu$ and $z\nu$ were estimated as scaling parameters. For $\chi_{\rm SG}$, $\gamma/z\nu = 0.3660(4)$ and $z\nu = 7.67(5)$ were obtained; for $\chi_{\rm CG}$, $\gamma/z\nu = 0.3214(6)$ and $z\nu = 5.70(1)$ were obtained. These results are compared with those reported in previous studies in Table 1 and Table 2. The obtained transition temperature appeared to show good accuracy compared with previously reported values. The results confirmed that the SG transition temperature is lower than the CG transition temperature, supporting the spin chirality decoupling picture in SG systems [2].

Before applying the dynamical correlation method to the present model, we demonstrated the method applying to ferromagnetic (FM) transition in the 3D FM Ising model and SG transition in the 3D $\pm J$ Ising model. We note that the reliability of z obtained from the correlation length estimated by the dynamical scaling law has been established. On the basis of this result, the original objective of analyzing the 3D $\pm J$ XY model was achieved. Using the transition temperatures obtained from the dynamical scaling above, we compute the correlation length. As a result, the value of z is evaluated as $z = 5.86(1)$ for the SG case and $z = 5.24(7)$ for the CG case. These results are compared with those of previous studies in Tables 1 and 2. The obtained results show improved accuracy for both the transition temperature and the critical exponents compared with previously reported findings. The dynamical exponent z was found to be lower in the CG case than in the SG case.

Table 1: Results of the SG transition compared with those in previous studies.

Reference	$T_{\rm SG}$	z	ν
[3]	0.39(2)	4.4(3)	1.2(2)
[4]	0.455(15)	5.6(6)	0.85(8)
[5]	0.435(15)	5.0(1)	1.25(15)
Present work	0.396(1)	5.86(1)	1.30(4)

Table 2: Results of the CG transition compared with those in previous studies.

Reference	$T_{\rm CG}$	z	ν
[6]	0.39(3)	7.4(20)	1.2(2)
[4]	0.467(10)	6.3(5)	0.74(4)
[5]	0.445(15)	5.1(2)	1.05(10)
Present work	0.4460(6)	5.24(7)	1.08(4)

References

[1] T. Nakamura, *Phys. Rev.*E**93** 011301 (2016); **99** 023301 (2019).

[2] H. Kawamura *Phys. Rev. Lett.* **68** 3785 (1992).

[3] E. Granato, *Phys. Rev.*B**69** 012503 (2004).

[4] T. Yamamoto, T. Sugashima and T. Nakamura, *Phys. Rev.*B**70** 0184417 (2004).

[5] T. Nakamura, unpublished.

[6] H. Kawamura and M. S. Li, *Phys. Rev. Lett.* **87** 187204 (2001).

Temperature dependence of specific heat in an extended Kitaev model on a honeycomb lattice

Takafumi SUZUKI
Graduate School of Engineering,
University of Hyogo, Shosha 2167, Himeji, Hyogo 670-2280

Realization of Kitaev spin liquid has been one of challenging tasks in condensed matter physics. As demonstrated by Jackeli and Khaliullin [1], transition metal oxides may have a potential to provide stages for studying the Kitaev spin liquid. So far, α-$RuCl_3$ has been much focused on as a candidate material from both theoretical and experimental aspects. Many effective models for α-$RuCl_3$ have been proposed for this decade, and it is expected that the Kitaev interaction (K) and Γ interaction between the nearest neighbor spins work as the dominant interactions. The details of the ground states in the S=1/2 Kitaev-Γ model has been much investigated by several numerical methods such as numerical exact diagolization, tensor-network scheme, and variational Monte Carlo.

In previous project, we have investigated thermal properties of the S=1/2 Kitaev-Γ model on a honeycomb lattice with the coupling amplitude on the z bond changed (Figure 1) [2]. We found that the two-peak structure in the temperature dependence of the specific heat is confirmed near $d \sim 1$ with the negative K and positive Γ. When $d = 0$, the system is equivalent to the Kitaev-Γ spin chain, where the specific heat shows a single peak structure. This single peak becomes the high-temperature peak in the two-peak structure at $d \sim 1$; the energy scale of the low-temperature peak does not correspond to that of the z bond coupling constant.

In this project, we have focused on the S=1 case. First, we have investigated the ground-state phase diagram by numerical exact diagonalization. We find that the ground-state phase diagram for the S=1 case is similar to that for the S=1/2 case; the isotropically interacting Kitaev-Γ model is located on the phase boundary when $K < 0$ and $\Gamma > 0$ [2], as shown in Figure 2. The different point is that the gapless phase related to the Tomonaga-Luttinger liquid, which appears in the S=1/2 spin chain limit, is replaced by the Haldane gap phase in the S=1 case. Secondary, we have calculated the temperature dependence of the specific heat in the Haldane gap phase by using the thermal pure quantum state [3]. Even in the S=1 case, the two-peak structure also appears at $d \sim 1$. However, the two-peak structure seems to be fragile against the increase of Γ. We find that the single peak in the spin chain limit corresponds to the high-temperature peak.

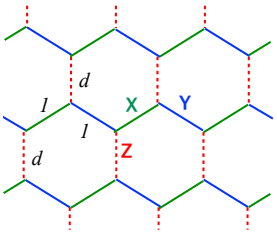

Fig. 1: Anisotropically interacting Kitaev-Γ model. The coupling strength on the X/Y bond is unity, and d is the ratio of the coupling strength on the Z bond against that on the X/Y bond.

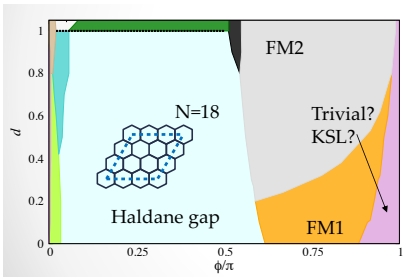

Fig. 2: Ground-state phase diagram for the S=1 anisotropically interacting Kitaev-Γ model. The horizontal axis corresponds to the coupling ratio between the Kitaev interaction and the G interaction; K=-cos ϕ and Γ=sin ϕ. All phase boundaries are decided from the second-derivative of the energy.

References

[1] G. Jackeli and G. Khaliullin, Phys. Rev. Lett. **102**, 017205 (2009).
[2] M. Gohlke, J. C. Pelayo, and T. Suzuki, Phys. Rev. B **109**, L220410; in preparasion.
[3] S. Sugiura, and A. Shimizu, Phys. Rev. Lett. **108**, 240401 (2012).

Level statistics and critical phenomena in non-Hermitian systems

TOMI OHTSUKI[1]
TOHRU KAWARABAYASHI[2]
KEITH SLEVIN[3]
1) Dept. Phys., Sophia University, Chiyoda-ku, Tokyo 102-8554, Japan
2) Dept. Phys., Toho University, Miyama 2-2-1, Funabashi 274-8510, Japan
3) Dept. Phys., Osaka University, Toyonaka, Osaka 560-0043, Japan

Our research over the past year centered on the symmetry classification and spectral statistics of random quantum systems, with a particular emphasis on non-Hermitian Hamiltonians.

We investigated the consequences of relaxing Hermiticity ($H \neq H^\dagger$) on the established tenfold symmetry classification of Hermitian random matrices (which includes three Wigner-Dyson,three Gade-Wegner, and four Altland-Zirnbauer classes). Non-Hermiticity expands the classification framework to 38 classes due to the distinct roles of transposition and complex conjugation.

A key activity was the numerical study of eigenvalue statistics in non-Hermitian systems. While eigenvalues are typically complex, certain symmetry classes permit real eigenvalues. We analyzed the level statistics of these real eigenvalues embedded within the complex spectrum, uncovering novel level repulsion behaviors [1].

Additionally, we studied the singular value statistics of non-Hermitian Hamiltonians. Recognizing that singular values offer different information compared to eigenvalues, we explored their statistical distributions within relevant non-Hermitian symmetry classes [2].

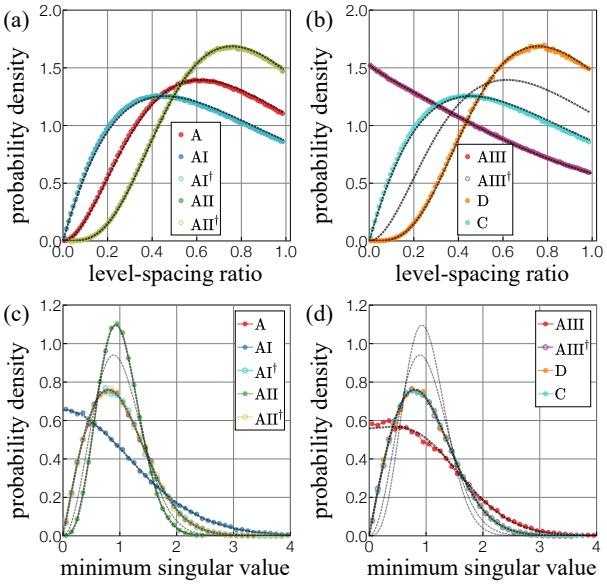

Figure 1: Singular-value statistics of non-Hermitian random matrices. (a, b) Level-spacing-ratio distributions of singular values in classes (a) A, AI, AI†, AII, AII†, (b) AIII, AIII†, D, and C. The black dashed curves are the analytical results for small random matrices. (c, d) Distributions of the minimum singular value $s_{\min}$ in classes (c) A, AI, AI†, AII, AII†, (d) AIII, AIII†, D, and C. The probability distribution functions are normalized such that their averages $\langle s_{\min} \rangle$ are 1. The black dashed curves are the analytical results for small random matrices. Taken from Ref. [2].

References

1. Z. Xiao, K. Kawabata, X. Luo, T. Ohtsuki, R. Shindou, Physical Review Research **4**, 043196 (2022).
2. K. Kawabata, Z. Xiao, T. Ohtsuki, R. Shindou, PRX Quantum **4**, 040312 (2023).

Understanding scrambling dynamics in quantum many-body systems towards realizing the dynamics in quantum computers

Masaki TEZUKA

Department of Physics, Kyoto University, Kitashirakawa, Sakyo-ku, Kyoto 606-8502

The Sachdev-Ye-Kitaev (SYK) model is a model of fermions with independently random all-to-all four-point interactions obeying the Gaussian distribution. The model is solvable, in the sense of random coupling average in the limit of large number of fermions. At low temperatures, the Lyapunov exponent, defined by the out-of-time ordered correlation functions, realizes the universal upper bound.

We previously studied a "sparse" version of the SYK model, in which the number of non-zero interaction terms is reduced to the order of the number of fermions. The sparse model with Gaussian random couplings had been known to reproduce essential features of the original SYK model [1]. In [2], we analyzed the spectral statistics of a further simplification, in which the magnitude of the nonzero couplings is a constant. Towards quantum simulation of such models, in [3] we studied another simplification of the SYK model: a model of Pauli spin operators with all-to-all four-spin interactions. We observed a striking quantitative coincidence between this spin model and the SYK model. In [4], we studied the quantum error correction (QEC) capabilities of the unitary time evolution according to various time-independent Hamiltonians by the Hayden-Preskill protocol. We compared the error estimate, obtained by the decoupling approach, against the one for random unitary evolutions obeying the circular unitary (Haar) ensemble. For the sparse SYK model, the QEC error estimate approaches the Haar value within a short time if the number of remaining couplings is sufficient for a random-matrix like spectral statistics. In contrast, for quantum spin chains often studied in the context of chaotic dynamics, scrambling is not observed in this sense, with the QEC error estimate remaining large.

To better elucidate the conditions for scrambling behavior, we have studied two classes of quantum models with two-local interactions, namely interactions between two distant locations of the system, unlike four in the models studied in [2] and [3]. In the first model, we consider two-local interactions between SU(d) generators. Simulations of this class of models might be accessible with qudit-based quantum devices. In the second model, we consider restricting the interactions in the SYK models to those between two clusters of fermions. By our numerical analysis, we find that these models also show strongly chaotic features. Details will be reported elsewhere.

References

[1] S. Su *et al.*, arXiv:2008.02303; A. M. Garcia-Garcia *et al.*, Phys. Rev. D **103**, 106002 (2021).

[2] M. Tezuka, O. Oktay, E. Rinaldi, M. Hanada, and F. Nori, Phys. Rev. B **107**, L081103 (2023).

[3] M. Hanada, A. Jevicki, X. Liu, E. Rinaldi, and M. Tezuka, J. High Energ. Phys. **2405**, 280 (2024).

[4] Y. Nakata and M. Tezuka, Phys. Rev. Research **6**, L022021 (2024).

Large-Scale Computation for Spin Glasses Using Extended-Ensemble Methods

Koji HUKUSHIMA
Department of Basic Science, University of Tokyo
3-8-1 Komaba, Meguro-ku, Tokyo 153-8902

Markov-chain Monte Carlo (MCMC) methods are the workhorse for sampling high-dimensional probability distributions. However, for systems with rugged, multi-modal energy landscapes –such as spin glasses– standard MCMC suffers from exponentially slow relaxation. Extended ensemble methods, such as Exchange Monte Carlo (or parallel tempering), partially resolve this problem by simulating multiple replicas at different temperatures and allowing configuration exchanges.

On modern supercomputers with $10^4 - 10^6$ cores, however, parallel tempering faces significant scalability issues: to fully utilize available cores, the number of replicas must grow accordingly. In practice, an excessive number of replicas is not only unnecessary but also harmful, at it increases round-trip time in temperature space and degrading sampling efficiency.

To address this issue, we explore Simulated Tempering (ST) as an alternative framework. ST jointly samples configurations and temperatures using a single replica, eliminating the need for inter-replica communication. Once the appropriate temperature weights are learned, independent ST simulations can be launched across thousands of compute nodes, making it well-suited for massively parallel environments.

To further improve ST, we introduce Lifted Simulated Tempering (Lifted ST), which accelerates temperature-space mixing by violating detailed balance in the temperature updates. This method augments the system with a binary lifting variable that indicates the direction of temperature change. Rather than proposing random temperature updates, Lifted ST deterministically continues in the same direction until a rejection occurs, at which point the direction flips. This reduces diffusive backtracking in temperature space and significantly reduces round-trip times.

An additional advantage is that Lifted ST is formulated in the continuous temperature limit, allowing smoother sampling and the use of thermodynamic observables such as the expected energy to guide temperature updates. This continuous formulation also eliminates the need to manually discredited temperature levels.

We applied Lifted ST to the three-dimensional Ising spin glass model as a benchmark. Using this method, we successfully computed the required temperature weights for system sizes up to $N = 64^3$. While equilibrium simulations are currently feasible up to 32^3, our benchmarks suggest that simulations of 48^3 spins are within reach on the ISSP supercomputing platforms. These results demonstrate the practical advantages of Lifted ST over traditional methods, particularly in massively parallel environments where conventional tempering methods struggle to scale.

In summary, Lifted ST offers a promising direction for large-scale sampling in complex systems by combining the strengths of extended ensemble methods with improved parallelized and faster convergence.

Multiscale simulations for complex flows

Yohei MORII and Toshihiro KAWAKATSU

Department of Physics,

Tohoku University, Sendai, Miyagi 980-8578

Macroscopic complex viscoelastic flows usually originate from the microscopic molecular processes such as entanglements of polymer chains or deformations of molecular aggregates. To simulate such complex flows, it is essential to combine macroscopic flow simulation with microscopic molecular simulations to generate local stress field. We are developing a platform for multiscale simulations on complex flows named MSSP (Multi-Scale Simulation Platform for complex flows), where a macroscopic flow simulator based on smoothed particle hydrodynamics (SPH) and microscopic molecular dynamics simulators embedded in each of SPH particles are coupled [1]. In our previous ISSP-supercomputer project (2023-Ca-0111), we studied the Marangoni effect of surfactant adsorbed on an oil/water interface using MSSP. For such a purpose, we implemented an evaluation method of surface tension and a diffusion process of microscopic molecules between adjacent SPH particles. In the present project, we use the above implementation to systematically explore the behavior of an oil droplet shape floating in an aqueous micellar solution.

Figure 1 shows simulation results using 10,000,000 micelles on MSSP. By changing the micellar extensibility (viscoelastic effect) and the surfactant affinity to the oil/water interface, various droplet shapes are observed [2].

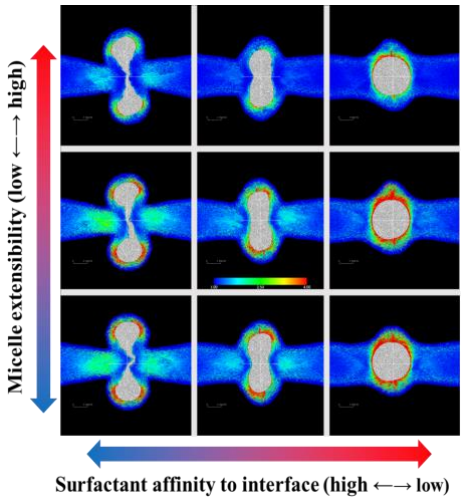

Fig.1 Oil droplet shapes for various conditions of micellar extensibility and surfactant affinity to the oil/water interface.

Acknowledgement

The computation in this work has been done using the facilities of the Supercomputer Center, the Institute for Solid State Physics, the University of Tokyo.

References

[1] Y.Morii and T.Kawakatsu, Phys. Fluids, **33**, 093106 (2021).

[2] Y.Morii and T.Kawakatsu, *in preparation*

Molecular dynamics simulation of protein aggregation

Hisashi Okumura

Exploratory Research Center on Life and Living Systems,
Institute for Molecular Science, Okazaki, Aichi 444-8585

Protein aggregates such as oligomers and amyloid fibrils cause more than 40 diseases. For example, Alzheimer's disease is caused by aggregated amyloid-β (Aβ) peptides. Aβ peptide usually consists of 40 or 42 amino acid residues. Aβ peptide with 40 residues is referred to as Aβ40, and that with 42 residues is referred to as Aβ42. We have performed molecular dynamics (MD) simulations to understand the aggregation and disaggregation mechanisms of Aβ peptides, including dimerization, oligomerization, amyloid fibril structure in bulk solution, conformations at the air-water interface, oligomer structure on the membrane surface, interaction with ganglioside and polyphenols, and disruption by ultrasonic wave and infrared laser irradiation.

During the last few fiscal years, we performed large-scale MD simulations of Aβ peptide aggregation using the supercomputer in ISSP. We have performed all-atom MD simulations of 32 Aβ40 and Aβ42 peptides in explicit water solvent for 2.0 μs. We observed Aβ peptides aggregated with repeating aggregation and disaggregation. They finally formed large oligomers, such as 20-mer and 32-mer. We revealed structural changes in the aggregation process, in particular focusing on the aspect ratio of the oligomers and secondary structure.

We observed that Aβ42 aggregated relatively faster than Aβ40 and formed larger oligomers than Aβ40. This observation is consistent with experimental fact. We revealed the mechanism of this phenomenon. We found that the formation of intramolecular β-sheet structures promotes the formation and aggregation of intermolecular β-sheet structures. In both Aβ40 and Aβ42, Glu22 and Lys28 form hydrogen bonds and the space between them tends to become a loop region. However, in Aβ42, the negatively charged C-terminus comes close to the positively charged Arg5, stabilizing the β-hairpin structure. On the other hand, in Aβ40, the β-hairpin structure is two residues shorter and is less stabilized. Therefore, Aβ42 is easier to take the β-hairpin structure and aggregate.

We also found that small oligomers are relatively spherical, but tend to extend in one way as they get larger. This tendency is also similar to experimental facts. We are currently analyzing this phenomenon in more detail.

Efficient sampling simulation of the soft modes significantly contribute to protein properties

Duy Tran, Wijaya Tegar, Bai Zhen, Sari Hagimoto, Hiroshi Kono, Tatsuki Hori, Masaki Mukaiyama, Yusei Ito, Vi Toan Lam, Yoshito Hasegawa, Reiya Hayashi, Akio Kitao

School of Life Science and Technology,

Institute of Science Tokyo, Ookayama, Meguro-ku, Tokyo 152-8550

Bacterial motility is primarily driven by the rotation of flagella—helical filaments that extend from the cell surface. This rotary motion is powered by a highly efficient, ion-driven molecular motor embedded in the bacterial cell membrane. The stator of this motor consists of a complex formed by five MotA monomers and two MotB monomers [1]. In Escherichia coli and many other bacteria, the MotA/MotB complex acts as the stator unit of the flagellar motor, harnessing the proton motive force (H^+ gradient) to generate torque.

MotA forms a transmembrane channel and contains cytoplasmic domains that interact with the rotor protein FliG, while MotB anchors the stator to the peptidoglycan layer of the cell wall via a conserved peptidoglycan-binding domain. The interaction between MotA and MotB facilitates proton translocation across the membrane, which in turn drives flagellar rotation. MotA contains transmembrane helices and cytoplasmic loops critical for torque generation, whereas MotB possesses a plug domain that regulates ion flow and secures the stator to the cell wall. Despite differences in ion selectivity and environmental adaptation, the MotA/MotB complex represents a remarkable example of convergent evolution, effectively converting electrochemical energy into mechanical motion. Studying this system not only enhances our understanding of microbial motility but also offers insights into bioenergetics and the design of synthetic nanomachines.

In this study, we investigated the ion permeation pathway of the Bacillus subtilis MotA/B complex, focusing on sodium ions. We performed relaxation simulations of the MotA/B structure embedded in a POPE/POPG membrane, using the structure from PDB ID 6YSL [1]. We then calculated the interaction frequency between sodium ions and residues within the MotA/B complex.

Our results revealed that the intracellular regions of MotA exhibit a high propensity for interacting with sodium ions (Figure 1a), while the extracellular regions showed fewer interactions. Among the residues with frequent sodium contact, Ser26, Ser28, and Asn32 were particularly prominent. Additionally, we found that sodium ions are trapped by Thr156 of both MotA1 and MotA2 (Figure 1b, c), located at the interface between MotA and MotB.

We further analyzed the pore architecture of the MotA/B complex using MOLEonline [2]. Two distinct pores were identified: one discontinuous pore extending from the periplasmic domain to the membrane region, and a continuous pore bridging the periplasmic and cytoplasmic domains. Notably, the continuous pore was found to be highly hydrophobic from the periplasmic side down to a bottleneck region within the membrane. This narrowest point, measuring approximately 2.7 Å in diameter, is formed by Ile183 and Phe187 of MotA and Val35 of MotB. Beyond the bottleneck, the pore widens and becomes solvent-accessible.

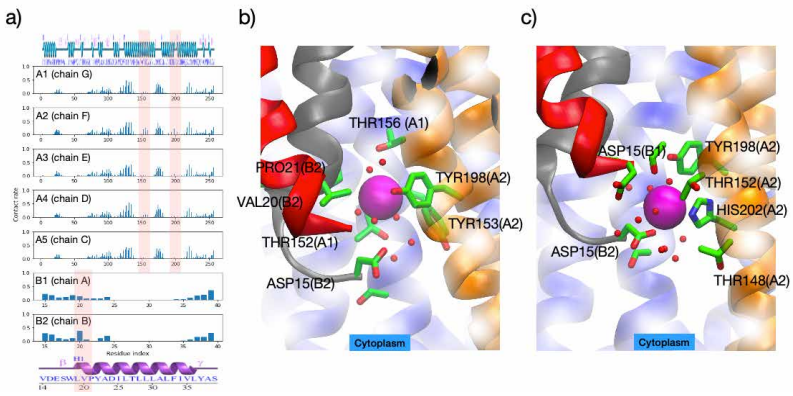

Figure 1. The sodium ions in contact with the residues on MotA, MotB proteins. a) the contact rates. b) the zoom-in of the sodium ion (in purple) in contact with MotA1, MotA2, MotB2. Water molecules are represented by the red spheres.

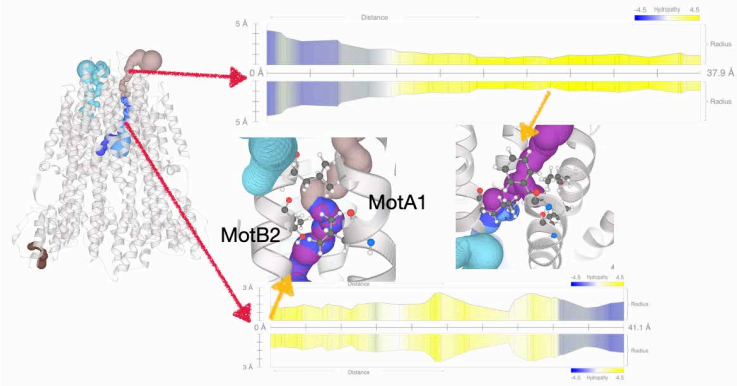

Figure 2. The pores are formed between the interfaces of MotA and MotB proteins of the *Bacillus subtilis* MotA/B complex.

Reference

[1] Deme et al, Nat MicroBiol 5, 1553 (2020)

[2] Pravda et al, Nucleic Acids Res 46, W368 (2018)

Fast free-energy estimation using simulated tempering with Wang-Landau-type feedback

Yoshihiko NISHIKAWA
Department of Physics, Kitasato University
Sagamihara, Kanagawa, Japan, 252-0373

Simulated tempering (ST) [1] is an extended-ensemble Monte Carlo technique that dynamically changes control parameters of the system with maintaining equilibrium at any time. ST can accelerate decorrelation and equilibration of complex systems with rugged free-energy landscapes, by changing temperature (or any other intensive parameters) to bypass the slow dynamical pathways. However, unlike parallel tempering (PT), also known as Exchange Monte Carlo [2], ST needs the free energy of the system to achieve an efficient sampling for a given temperature range. This complicates practical use of ST, since precisely estimating the free energy is in general an exhausting task.

The extended partition function for ST with a set of temperature points $\{\beta_i\}$ ($\beta_1 < \beta_2 < \cdots < \beta_M$) is

$$\mathcal{Z}(\{\beta_i\}_{i=1,2,\cdots,M}) = \sum_{i=1}^{M} Z(\beta_i)\exp(g(\beta_i)), \quad (1)$$

with $Z(\beta)$ the partition function of the system at inverse temperature β and $g(\beta)$ a bias function that controls the marginal distribution of β:

$$\pi(\beta) = \frac{Z(\beta)\exp(g(\beta))}{\mathcal{Z}(\{\beta_i\})} = \frac{\exp(-\beta F(\beta) + g(\beta))}{\mathcal{Z}(\{\beta_i\})}. \quad (2)$$

If we could set $g(\beta) = -\beta F(\beta)$, where $F(\beta)$ is the free energy of the system, then the marginal distribution is flat over $\{\beta_i\}$. ST is thus optimal with $g(\beta) = \beta F(\beta)$ as it can sample from the entire temperature range with equal probability. However, estimating the free energy of a given system needs extensive simulations. One could run PT simulations to estimate the free energy beforehand [3], whereas ST simulations are not needed anymore as PT itself generates equilibrium samples if one employs this approach. Others have proposed on-the-fly estimation algorithms [4, 5], which rely on the naive thermodynamic integration and suffer from slow dynamical relaxation at low temperatures.

Here, we propose an efficient irreversible Monte Carlo algorithm to estimate the free energy of the system. Our algorithm iteratively updates an instantaneous free-energy estimate with the Wang-Landau-type feedback [6, 7], and eventually converges to the true free energy in the long-time limit. We further incorporate a simple yet maximally irreversible dynamical rule in the algorithm. The dynamical rule implements a *lifted* Markov chain [8], which can drastically accelerate the convergence.

Our algorithm needs two additional ingredients compared to conventional ST simulations: A histogram $H(\beta)$ recording the number of visits to each β_i and a parameter f that controls the precision of the free-energy estimate. Suppose the system is currently at $\beta = \beta_i$ and has an energy E. We first sample a *lifting parameter* $v \in \{\pm 1\}$ with equal probability, and propose a change β to β_{i+v} with probability 1. The change is accepted

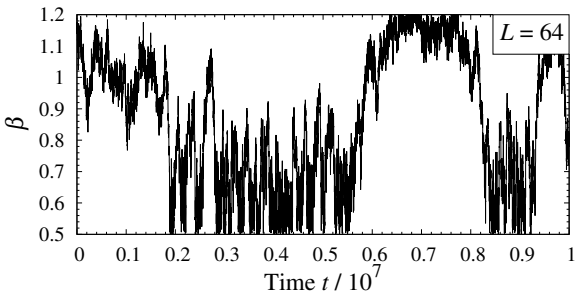

Figure 1: Typical trajectory in the β space during an equilibrium ST simulation for $L = 64$.

with a probability satisfying the balance condition, e.g. the simple Metropolis probability, and update $i \leftarrow i + v$ and $\beta = \beta_i$. We keep proposing the change i to $i + v$ as long as it is accepted. When rejected, we update $v \leftarrow -v$, and repeat the same until the number of attempts reaches a predetermined number ℓ, which is set to $M/2$ in our study. During the β updates, we accumulate the histogram $H(\beta_i)$ and update the current free-energy estimate $g(\beta_i) \leftarrow fg(\beta_i)$. From time to time, we check if the histogram is sufficiently *flat*, and if it is, we reduce f to $\sqrt{f}$ and reset the histogram to zero. Here, we consider the histogram is flat if $\min_i H(\beta_i) > 0.8 \sum_i H(\beta_i)/M$. We stop the estimation when $\log f$ becomes small enough, e.g. 10^{-6}, and can seamlessly move on to production runs using the estimated free energy.

We apply this algorithm to the three-dimensional Edwards-Anderson (EA) spin glass model with Gaussian couplings on a periodic cubic lattice of linear length L. The number of temperature points $M = 401$ and $\beta_i = 0.5 + 0.7(i-1)/(M-1)$ $(i = 1, 2, \cdots, M)$, where the unit of temperature is the standard deviation of the Gaussian couplings. In numerical study of spin glass models, an average of any physical quantity over many random realizations needs to be taken, requiring large-scale numerical resource. We took an advantage of the ISSP supercomputer to perform large-scale parallelized simulations of the model for 512 independent random instances with up to $L = 64$. We numerically find that the mean convergence time τ_c of the algorithm defined as the timescale to reach the optimal performance grows algebraically with L as $\tau_c \sim L^4$. For $L = 64$, our algorithm converges the slowest, most difficult instance within a month, whereas most of the instances take about two weeks. This is in strong contrast with a conventional algorithm [4, 5], which we find takes an exponentially long time to converge. After the convergence of the free-energy estimation, we have run equilibrium ST simulations with fixing the bias function. Fig. 1 shows a typical trajectory in the β space for $L = 64$. Clearly, the system can wander between $\beta_1 = 0.5$ and $\beta_M = 1.2$, indicating our algorithm has precisely estimated the free-energy estimation even with this large L.

This work was done in collaboration with A. C. Maggs and Koji Hukushima.

References

[1] E. Marinari and G. Parisi, EPL **19**, 451 (1992).

[2] K. Hukushima and K. Nemoto, J. Phys. Soc. Jpn. **65**, 1604 (1996).

[3] A. Mitsutake and Y. Okamoto, Chem. Phys. Lett. **332**, 131 (2000).

[4] S. Park and V. Pande, Phys. Rev. E **76**, 016703 (2007).

[5] P. H. Nguyen, Y. Okamoto, and P. Derreumaux, J. Chem. Phys. **138**, 1 (2013).

[6] F. Wang and D. P. Landau, Phys. Rev. Lett. **86**, 2050 (2001).

[7] C. Zhang and J. Ma, Phys. Rev. E **76**, 036708 (2007).

[8] F. Chen, L. Lovász, and I. Pak, Lifting Markov chains to speed up mixing, in Proceedings of the Thirty-first Annual ACM Symposium on Theory of Computing (ACM, New York, 1999), pp. 275 – 281.

Defect structures and their transport properties in thermoelectric chalcogenides

Susumu FUJII
Department of Materials, Faculty of Engineering, Kyushu University
Motooka, Fukuoka 819-0395
Nanostructures Research Laboratory, Japan Fine Ceramics Center
Mutsuno, Atsuta, Nagoya 456-8587

Thermoelectric materials can directly convert heat into electricity. To improve their conversion efficiency, it is necessary to enhance the Seebeck coefficient and the electrical conductivity while simultaneously reducing the lattice thermal conductivity. In recent recent years, strategies such as introducing lattice deffects and nanostructures, as exemplified by nanocrystalline materials, have been actively pursued to effectively reduce lattice thermal conductivity without deteriorating electronic properties [1]. However, the impact of intrinsic point defects, dopants, dislocations, and grain boundaries (GBs) on thermoelectric properties remain unclear at least in a quantitative manner.

In this study, we investigated the effects of intrinsic point defects and GBs on the thermal conductivity of PbTe, a representative thermoelectric material, using MD simulations. We employed an artificial neural network (ANN) potential for the interatomic interactions and also evaluated its accuracy [2]. Most of the computational resources were devoted to the long-time ANN-MD simulations. These calculations were performed using an MD code implemented by a collaborator, with additional codes for perturbed MD for thermal conductivity calculations developed by the author.

First, we examined the reproducibility of phonon properties and lattice thermal conductivity of bulk PbTe using the ANN potential. The ANN potential was found to accurately reproduce the harmonic phonon dispersions, the frequency shifts due to anharmonicity, the linear thermal expansion coefficient, and the temperature dependence of the lattice thermal conductivity. Furthermore, it was confirmed that the ANN potential sufficiently reproduces the energies of intrinsic point defects (such as vacancies, antisites, and interstitials) and grain boundaries, as well as the atomic forces in their vicinity, in good agreements with density functional theory (DFT) calculations.

Using the ANN potential, we calculated the lattice thermal conductivity in the vicinity of point defects. The thermal conductivity was suppressed with a trailing effect behind the point defects (Fig. 1). The extent of the suppression varied depending on the type of point defect, with interstitials causing the significant reduction of thermal conduction. Frequency analysis revealed that the nature of phonons scattered by the defects differed depending on the defect type. The atom-resolved thermal conductivity was found to be strongly correlated with the changes in phonon frequencies induced by the introduction of defects, reflecting alterations in the local potential energy surface [2].

Approximately 20 symmetric tilt GB models of PbTe were also constructed using the ANN potential. Except for the twin boundary, these grain boundaries exhibited relatively

similar GB excess energies. In contrast, the GB excess volumes varied significantly depending on the GB misorientation. The GB thermal resistance among these models differed by up to several times. While the GB thermal resistance showed a correlation with both the GB excess energy and volume, the correlation was weaker compared to the trends observed in MgO and $SrTiO_3$ [3, 4]. The factors governing lattice thermal conduction at PbTe GBs are expected to be elucidated through future structural and phonon analyses.

This study demonstrates that by utilizing highly accurate machine learning potentials, it is becoming possible to quantitatively and microscopically elucidate the effects of lattice defects on thermoelectric properties.

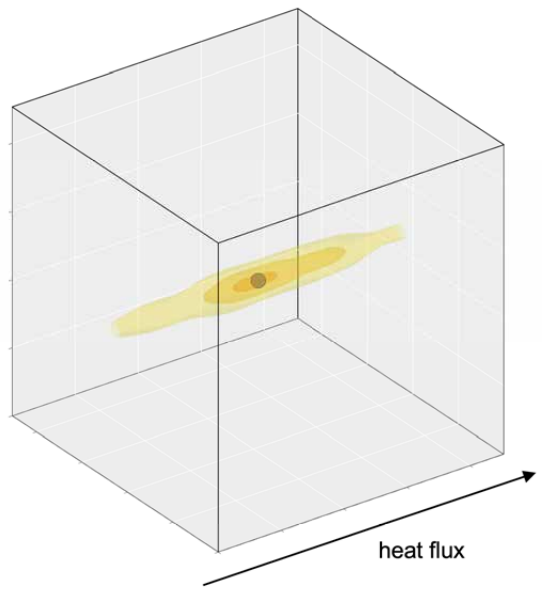

Figure 1: Suppression of lattice thermal conduction near Pb vacancy in PbTe. Black circle indicates the position of the Pb vacancy. The regions where the thermal conductivity is reduced are shown with colored shading, with darker colors indicating greater reductions.

References

[1] K. Biswas, J. He, I.D. Blum et al., Nature **489**, 414-418 (2012).

[2] T. Yokoi, S. Fujii, Y. Ogura, K. Matsunaga, under review.

[3] S. Fujii, T. Yokoi, C.A.J. Fisher et al.m Nat. Commun. **11**, 1854 (2020).

[4] S. Fujii, H. Isobe, W. Sekimoto, M. Yoshiya, Scr. Mater. **258**, 116524 (2025).

Molecular Dynamics Simulation for Studying Polymer Infiltration Process in Nanoporous Materials

Nobuhiko HOSONO

Department of Applied Chemistry, Graduate School of Engineering

The University of Tokyo, Hongo, Bunkyo-ku, Tokyo 113-8656

Metal-organic frameworks (MOFs) are crystalline compounds possessing numerous nano-sized pores, capable of encapsulating molecules ranging from small gas molecules to extremely long polymers, as demonstrated by previous research [1]. Recently, we experimentally discovered that the rate of polymer infiltration and the diffusion pathways within the pores significantly vary depending on the chemical structure and functional groups within the polymer chains, leading to differences in adsorption capacity into the MOFs [2].

From the previous year, we performed all-atom MD simulations of this polymer diffusion process, aiming to gain molecular-level insights into the mechanism behind these phenomena. For this study, we employed the LAMMPS package, which is specialized for large-scale parallel computing of molecular dynamics.

To study how polymer microstructures affect MOF infiltration dynamics, we prepared polyethylene glycol (PEG) chains possessing a xylene unit at the center of their main chain. We modeled three types of PEG chains, which are different in the substitution position at the central xylene unit, namely, *ortho* (***o*-PEG**), *meta* (***m*-PEG**), or *para*-substituted (***p*-PEG**). The molecular weights and other structural characteristics are set to be constant for the three model PEGs. The structure of a MOF was generated based on its single-crystal X-ray diffraction data. Fifteen PEG chains of each type (either ***o*-PEG**, ***m*-PEG**, or ***p*-PEG**) were placed in the simulation box and structurally relaxed. Subsequently, initial structures were obtained by placing the PEG chains in contact with the (001) plane of the MOF. By conducting MD simulations at 393 K for 100 ns each on these structures with MPI processes, we tracked the infiltration and diffusion behavior of the PEGs within the nanopores of the MOF. The center of mass (COM) of the PEG chains was plotted as a function of time, showing infiltration kinetics of the PEG into the MOF nanopores (**Figure 1**). It became evident that differences in conformation due to the positional isomerism significantly influence the infiltration and diffusion behavior (**Figure 1**). This MD-based observation well supported the experimental results that ***o*-PEG** shows significantly slow infiltration kinetics compared to ***m*-PEG** and ***p*-PEG** [3].

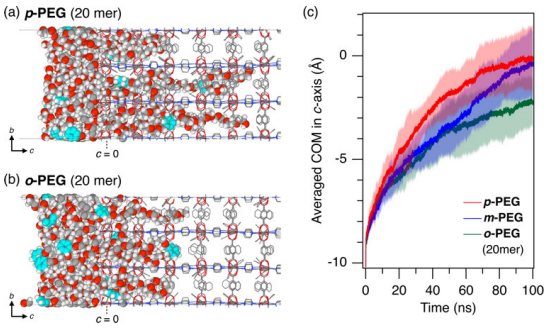

Figure 1. Representative MD snapshots of (a) ***p*-PEG** and (b) ***o*-PEG**. (c) Time evolution of the averaged COM in the c-axis in MOF. Averaged data from the five MD simulation runs are plotted as solid lines with shaded error bands of σ ($N = 5$).

In this study, we also investigated the reverse process using steered molecular dynamics (SMD) simulation. Non-substituted PEG (***n*-PEG**) with methyl group termini was arranged in the nanopores of MOF, then the external force was applied to the terminal C atom near the MOF surface after the 5-ns structural relaxation run, inducing the pullout of the PEG chain (**Figure 2**). It was carried out by "smd" command, pre-installed in LAMMPS. The required force during the pulling event was recorded, which successfully generated a force curve. All the MD run was executed at room temperature (298 K) in the *NVE* condition, and constant pulling speeds of 0.5 m/s or 2 m/s were applied. Interestingly, the force curve obtained by the SMD simulation reproduced the experimental force curve measured by single-molecule force spectroscopy analysis.

We also conducted the same SMD simulation for ***p*-PEG** to see the effect of the xylene unit on the force signals. Interestingly, a characteristic force signal was observed at a certain length in the force curve, which corresponds to the xylene substitution point on the ***p*-PEG** chain.

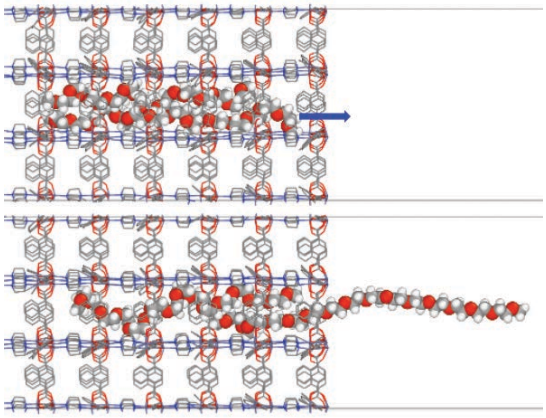

Figure 2. Representative MD snapshots of pulling ***n*-PEG**. The PEG chain was progressively extracted along the *c*-axis.

In summary, we successfully revealed the effect of polymer structure on both infiltration and forced-extraction behaviors in MOF nanopores at the molecular level using the large-scale parallel computing resources.

References

[1] N. Oe, N. Hosono, and T. Uemura, *Chem. Sci.* **12**, 12576 (2021).

[2] N. Mizutani *et al.*, *J. Am. Chem. Soc.* **142**, 3701 (2020).

[3] N. Hosono, Y. Kono, N. Mizutani, D. Koga, and T. Uemura, *Chem. Commun.* **60**, 13690 (2024)

Free energy and phase coexistence in various boundary conditions

Naoko NAKAGAWA
Department of Physics, Ibaraki University
2-1-1 Bunkyo, Mito, Ibaraki 310-8512

We investigate the thermodynamics of simple fluids to describe liquid-gas coexistence under weak gravity during heat conduction.

First, we focused on isothermal systems under weak gravity without heat conduction [1]. We theoretically constructed a global thermodynamic framework incorporating gravitational effects, derived from equilibrium statistical mechanics. The inhomogeneity induced by gravity is summarized by a new intensive variable, mgL, representing the difference in gravitational potential energy between the top and bottom of the container. Consequently, the thermodynamic description is extended from the standard (T, V, N) ensemble to (T, V, N, mgL). The extended free energy exhibits non-analyticity at $g = 0$, which can be interpreted as a first-order phase transition related to the liquid-gas configuration. The Maxwell relations derived from this global thermodynamics predict the behavior of the Virial pressure (the spatial average of the local pressure) as a function of the mean density N/V. We then performed molecular dynamics simulations using LAMMPS for one-component Lennard-Jones fluids. The theoretical predictions align well with the numerical observations, such as the dependence of the Virial pressure on N/V or g.

Next, we drove the system into heat conduction states by connecting heat baths with temperatures T_1 and T_2 to the top and bottom walls of the container, respectively. The heat flow direction was set opposite to gravity, with the top plate colder than the bottom $(T_1 < T_2)$. Thermally, the colder temperature (T_1) favors the liquid phase locating near the top wall above the gas. However, gravity pulls the denser liquid phase towards the bottom. This simple setup leads to rich system behavior. Since the system is conducting heat and thus out of equilibrium, established equilibrium statistical mechanics and thermodynamics do not directly apply. Molecular dynamics simulations provide a means to explore novel phenomena in such non-equilibrium systems, potentially guiding theoretical developments in nonequilibrium thermodynamics. This approach helps circumvent simplifying assumptions that might obscure the system's true behavior. For instance, standard theories might assume local equilibrium or neglect detailed interfacial physics, whereas simulations directly model particle interactions without these constraints.

Gravity and heat flux are the respective mechanical and thermal drivers of inhomogeneity in the system. We define a dimensionless parameter

$$\chi = \frac{k_{\mathrm{B}}(T_2 - T_1)}{mgL}, \tag{1}$$

representing the ratio between the thermal energy difference across the system and the gravitational potential energy difference. This parameter χ quantifies the relative strength of heat conduction versus gravity.

Through careful and elaborate numerical experiments, particularly under non-equilibrium conditions, the observed phenomena were

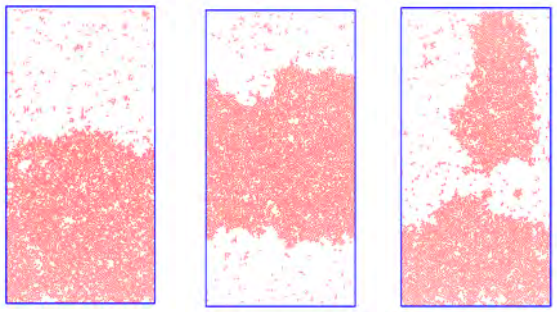

Figure 1: Phase coexistence of liquid and gas in heat conduction under gravity. See text.

found to be highly sensitive to the specific system setup, potentially more so than to the precise value of χ. We focused on the case with 'dry' walls, where the interaction between fluid particles and the top/bottom walls is described by the purely repulsive Weeks-Chandler- Andersen (WCA) potential [2]. When χ is small (i.e., gravity dominates over the thermal gradient effect), the bulk liquid resides at the bottom (Fig. 1, left). For $\chi > 10$, the bulk liquid forms a layer hovering above a gas layer near the bottom (Fig. 1, middle). If gravity is sufficiently weak (corresponding to very large χ), the liquid floats to the top. Furthermore, it was observed that the gas located above the liquid layer (e.g., in the hovering state) becomes supercooled, while the gas below the liquid remains in a normal (non-supercooled) state.

Finally, we changed the wall properties from dry (repulsive) to 'wet' (attractive). With sufficiently attractive (wet) walls, the system's behavior changes significantly; for instance, the hovering state observed with dry walls is no longer found. Instead, the liquid preferentially wets the top wall, residing above the gas, even for χ values as small as 2.0, where thermal effects are comparable to gravity. Furthermore, for slightly smaller χ values (around 1), the system exhibits dynamic behavior: the liquid moves towards the top wall, detaches, and falls back down (Fig. 1, right).

References

[1] N. Nakagawa, S.-i. Sasa, T. Hirao, T. Shiina, K. Tachi, and A. Yoshida, Global Thermodynamics for Isothermal Fluids under Weak Gravity, arXiv 2412.19643.

[2] A. Yoshida, N. Nakagawa, and S.-i. Sasa: Heat-Induced Liquid Hovering in Liquid-Gas Coexistence under Gravity, *Phys. Rev. Lett.* **113**, 117101 (2024)

All-atomic molecular dynamics simulation for vitrimers

Yutaka Oya

Department of Materials Science and Technology,

Tokyo University of Science, Niijuku, Katsushika-ku, Tokyo 125-8585

This study aims to elucidate the damage repair mechanism of vitrimers by molecular simulations. The target material is the reaction-cured product of bisphenol A diglycidyl ether (DGEBA) and 4-aminophenyl disulfide (AFD), which has a dense crosslinked network structure. When the cured product is deformed by external forces, the mechanical properties deteriorate due to the dissociation of numerous covalent bonds that constitute the cross-linked structure, as well as the disulfide bonds contained in AFD. Subsequently, it is considered that the disulfide bonds recombine through thermal pressing, leading to the recovery of mechanical properties.

In this study, the above-mentioned mechanism is reproduced through the integration of quantum chemical (QC) calculations and All-atomic molecular dynamics (MD) simulations. Specifically, quantum chemical (QC) calculations are first conducted to elucidate the recombination pathways of dissociated disulfide bonds. Subsequently, molecular dynamics (MD) simulations incorporating the identified mechanism are performed to derive stress–strain curves and evaluate the degree of mechanical property recovery.

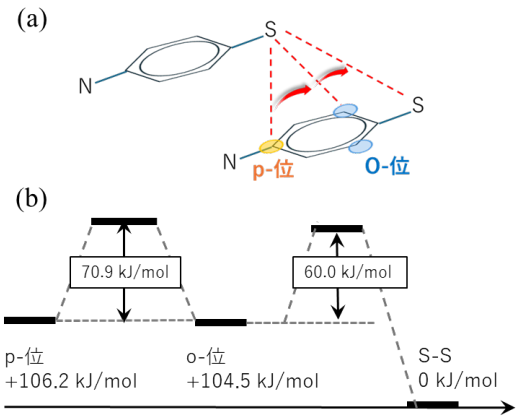

Fig. 1: (a) Stable structures identified by QC calculations, and (b) activation energies associated with disulfide bond reformation.

Reaction pathway searches based on QC were performed using the Global Reaction Route Mapping (GRRM) algorithm [1]. This algorithm interfaces with the quantum chemistry software Gaussian and enables automated exploration of the potential energy surface. As a result, it facilitates efficient identification of transition states even in complex multi-electron systems such as polymers. Furthermore, all molecular dynamics (MD) simulations—including crosslink formation, covalent bond dissociation, and self-healing processes—were carried out using LAMMPS software [2].

Quantum chemical (QC) calculations

revealed two stable structures associated with the reformation of disulfide bonds. As illustrated in Figure 1(a), these structures correspond to configurations in which the carbon atom at either the ortho or para position of the benzene ring bonded to one sulfur atom forms a bond with the second sulfur atom. The activation energies between these three stable structures are shown in Figure 1(b). These activation energies are significantly lower than the previously reported value for disulfide bond exchange (about 192 kJ/mol [3]), indicating that the reactions can readily occur under thermal compression.

To evaluate the impact of the disulfide bond repair mechanism identified by QC on the recovery of mechanical properties in a condensed system, MD were performed. A uniaxial tensile simulation was first conducted on a crosslinked network to induce complete dissociation of all disulfide bonds, followed by compression and relaxation simulations. When the QC-derived repair mechanism was incorporated, approximately 70% of the disulfide bonds were successfully reformed. In contrast, when only direct recombination between sulfur atoms was allowed, the recovery ratio remained around 40%. These results indicate that the reaction pathway identified in this study plays a critical role in enhancing bond reformation.

Finally, the stress–strain curves corresponding to each structure are shown in

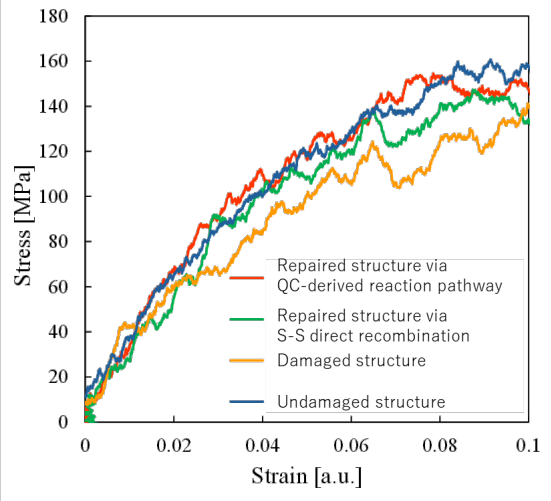

Fig. 1: Stress-strain curves obtained by MD simulations.

Figure 2. The structure repaired via the QC-derived reaction pathway (red) exhibits improved mechanical properties compared to the structure repaired by direct sulfur–sulfur recombination (green) and the fully dissociated disulfide network (yellow). Notably, its mechanical performance comparable to that of the undamaged crosslinked structure (blue), indicating a substantial recovery of properties through the proposed repair mechanism.

References

[1] S. Maeda, K. Ohno, and K. Morokuma, Phys. Chem. Chem. Phys., **15** (11), 3683 (2013).

[2] Large-scale Atomic/Molecular Massively Parallel Simulator, open source code: http://lammps.sandia.gov/ (Last accessed date: 2025/04/30.)

[3] Y.-M. Yang, H.-Z. Yu, X.-H. Sui, and Z.-M. Dang, J. Phys. Org. Chem. **29**, 6-13 (2016).

First-Principles Elucidation of Conducting Mechanisms in OligoEDOT Complexes: Towards Molecular Design Guidelines for High Conductivity

Tomoko FUJINO

Institute for Solid State Physics,

The University of Tokyo, Kashiwa-no-ha, Kashiwa, Chiba 277-8581

Organic conductors are broadly divided into two categories: low-molecular-weight materials and polymers. Low-molecular-weight materials possess well-defined structures but offer limited control over their conductivities. Conductive polymers, on the other hand, feature highly conjugated systems but are challenging to control due to their structural inhomogeneity. To bridge this gap, oligomer-based conductors have been developed as intermediate materials. These conductors, based on oligo(3,4-ethylenedioxythiophene) (oligoEDOT), are modeled after the doped PEDOT family [1–5].

In this study, we systematically investigated the influence of end-cap substituents [6] and the stacking structure in donor–acceptor alternatingly mixed-stack complexes [7]. The effects of these structural factors were quantitatively evaluated using first-principles calculations (QUANTUM ESPRESSO, RESPACK, and H-wave packages; performed at Ohtaka, Supercomputer Center, ISSP). Our calculations revealed that the magnitude of the Coulomb repulsion between carriers, $\boldsymbol{U_{\mathrm{eff}}}$, is the dominant factor determining conductivity. Based on these theoretical findings, we provided electronic insights explaining the superior conductivity of mixed stack complexes compared to previously reported complexes [7]. This work thereby offers a new molecular design guideline for developing highly conducting charge-transfer salts and mixed-stack complexes.

References

[1] R. Kameyama, T. Fujino*, H. Mori*, et al. Chem. Eur. J. **27**, 6696 (2021).

[2] R. Kameyama, T. Fujino*, H. Mori*, et al. Phys. Chem. Chem. Phys. **24**, 9130 (2022).

[3] R. Kameyama, T. Fujino*, H. Mori*, et al. J. Mater. Chem. C **10** (9), 7543 (2022).

[4] K. Onozuka, T. Fujino*, H. Mori*, et al. J. Am. Chem. Soc. **145**, 15152 (2023).

[5] T. Fujino*, H. Mori*, et al. Faraday Discuss. **250**, 348 (2024).

[6] K. Onozuka, T. Fujino*, H. Mori* et al. Higher conductivity in, J. Mater. Chem. C, **12**, 13956 (2024).

[7] T. Fujino*, H. Mori*, et al. Nature Commun. **15**, 3028 (2024).

Field-Induced Spin Liquid Phase of Quantum Spin Chain with Biquadratic Interaction

Tôru SAKAI[1,2], Hiroki NAKANO[1], Masaru HASHIMOTO[1], Tomohide KAWATSU[1], Haruto SUZUKI[1], Tomoki HOUDA[1]Rito FURUCHI[1], and Tokuro SHIMOKAWA[3]
[1]*Graduate School of Science, University of Hyogo, Kouto, Kamigori, Hyogo 678-1297, Japan*
[2]*National Institute for Quantum Science and Technology, SPring-8, Kouto, Sayo, Hyogo 679-5148, Japan*
[3]*Theory of Quantum Matter Unit, Okinawa Institute of Science and Technology Graduate University, Onna-son, Okinawa 904-0495, Japan*

1 Introduction

The quantum spin chains exhibit various interesting phenomena in the magnetization process, for exmaple, the magnetization jump, plateau, and spin nematic state, etc. The density matrix renormalization group analysis of the S=1 antiferromagnetic chain with the biquadratic exchange interaction indicated that the spin nematic liquid phase appears in the magnetization process[1]. It was also supported by the numerical diagonalization and the conformal field theory analysis[2, 3]. In the present work, the magnetization processes of the S=3/2 and S=2 antiferromagnetic chains with the biquadratic exchange interaction are investigated using the numerical diagonalization of finite-size clusters. It is found that the magnetization jump appears just before the saturation magnetization, as well as the classical spin system. This behavior is different from the S=1 chain. In addition it is indicated that the magnetization process where each magnetization step is $2S$ appears for sufficiently large biquadratic interaction. Namely the three-magnon and four-magnon bound states are realized for the S=3/2 and S=2 chains, respectively. In the case of the S=1 chain, the two-magnon bound state corresponding to the spin nematic phase occurs. Thus in general it can be predicted that the 2S-magnon bound state would be induced by the biquadratic exchange interaction in the magnetization process of the spin-S antiferromagnetic chain. The phase diagrams with respect to the biquadratic interaction and the magnetization are also presented for S=3/2 and S=2 antiferromagnetic chains. The three- and four-magnon bound states are expected to correspond the triatic and quatic Tomonaga-Luttinger liquid phases, respectively[4].

2 Model

The systems under the magnetic field are descibed by the Hamiltonian

$$\begin{aligned} \mathcal{H} &= \mathcal{H}_0 + \mathcal{H}_Z \\ \mathcal{H}_0 &= J\sum_{j=1}^{L} \vec{S}_j \cdot \vec{S}_{j+1} + J_{\rm BQ}\sum_{j=1}^{L} (\vec{S}_j \cdot \vec{S}_{j+1})^2 \\ \mathcal{H}_Z &= -H\sum_{j=1}^{L} S_j^z. \end{aligned} \tag{1}$$

Now we consider the cases of $S = 3/2$ and 2, respectively, for $J_{\rm BQ} < 0$ and fix $J = 1$.

3 Results

The $S = 3/2$ and $S = 2$ antiferromagnetic chains with the negative biquadratic interaction are investigated using the numerical diagonalization of the finite-size cluster ($L = 12$). It is found that for sufficiently large negative $J_{\rm BQ}$, the field-induced spin triatic and quatic TLL phases appear in the $S = 3/2$ and $S = 2$ chains, respectively, instead of the spin nematic TLL phase in the $S = 1$ chain. Probably it is expected that the spin-S chain with sufficiently large negative $J_{\rm BQ}$ exhibits the field-induced 2^{2S}-pole TLL phase. In addition it is found that the magnetizaiton jump up to the saturation magnetization occurs for intermediate $J_{\rm BQ}$ in the case of $S > 1$.

References

[1] S. R. Manmana, A. M, Lauchli, F. H. L. Essler and F. Mila, Phys. Rev. B **83**, 184433 (2011).

[2] T. Sakai, AIP Advances 11, 015306 (2021).

[3] T. Sakai, H. Nakano, R. Furuchi and K. Okamoto, J. Phys.: Conf. Ser. 2164, 012030 (2020).

[4] T. Sakai, AIP Advances 14, 015332 (2024).

Spin Nematic Phase of 2D Ferromagnetic Dimer System

Toru SAKAI[1,2], Hiroki NAKANO[1], Masaru HASHIMOTO[1], Tomohide KAWATSU[1], Haruto SUZUKI[1], Tomoki HOUDA[1], Rito FURUCHI[1]

[1]*School of Science, University of Hyogo,, Hyogo 678-1297*

[2]*National Institutes for Quantum Science and Technology, Hyogo 679-5148*

1. Introduction

he spin nematic state is one of interesting topics in the field of magnetism. It is the quadrupole order of spins. It is characterized by the long-range four spin correlation and the two-magnon bound state. In most previous theoretical works, the mechanism of the spin nematic order has been based on the biquadratic interaction[1,2] or the spin frustration[3]. In the recent numerical study on the S=1/2 spin ladder system with the anisotropic ferromagnetic rung interaction, a new mechanism based on the easy-axis anisotropy and the external magnetic field was proposed and the field-induced spin nematic phase was predicted to appear at higher magnetization region[4]. On the other hand, the spin nematic phase was also been predicted for several two-dimensional quantum spin systems. The spin nematic order due to the mechanism based on the anisotropic ferromagnetic interaction proposed in the previous work would be expected to appear even in two dimensional systems. In the present paper, as an example, we focus on a magnetic system on the Shastry-Sutherland lattice, which includes the isotopic antiferromagnetic interaction and the anisotropic ferromagnetic one under magnetic field. Using the numerical diagonalization of finite-size clusters, we investigate the possible field-induced spin nematic phase.

2. Model and Calculation

We consider a spin-1/2 model on the Shastry-Sutherland lattice under magnetic field in Fig. 1. The Hamiltonian is given by the following forms

$$H_{\mathrm{tot}} = H_0 + H_Z$$

$$H_0 = J_1 \sum_{\langle i,j \rangle} \left[S_i^x S_j^x + S_i^y S_j^y + \lambda S_i^z S_j^z \right] + J_2 \sum_{\langle i,j \rangle} \overrightarrow{S_i} \cdot \overrightarrow{S_j}$$

$$H_z = -H \sum_j S_j^z$$

we consider ferromagnetic J_1 and antiferromagnetic J_2, We investigate this model using the numerical diagonalization of the 24-spin cluster under the periodic boundary condition, shown in Fig. 1

3. Results

The S=1/2 spin system on the Shasry-Sutherland lattice with the

anisotropic ferromagnetic interaction under magnetic field is investigated using the numerical diagonalization of the finite-size (24 spins) cluster. It indicates that .the possible field-induce spin nematic phase, which is characterized by the two-magnon bound state, appears at higher magnetization region than m=1/2. Since the numerical study is performed for only one system size in this paper, it would be important to try some other sizes to confirm the present conclusion in the thermodynamic limit. In addition the spin correlation function corresponding to the nematic order should be calculated to reveal the real spin configuration in the future work.

References

[1] H. H. Chen and P. M. Levy, Phys. Rev. Lett. 27, 1383 (1971)

[2] A. V. Chubukov, J. Phys.: Condens. Matter 2, 1593 (1990).

[3] T. Hikihara, L. Kecke, T. Momoi and A. Furusaki, Phys. Rev. B 78, 144404 (2008)

[4] T. Sakai, R. Nakanishi, T. Yamada, R. Furuchi, H. Nakano, H. Kaneyasu, K. Okamoto and T. Tonegawa, Phys. Rev. B 106, 064433 (2022).

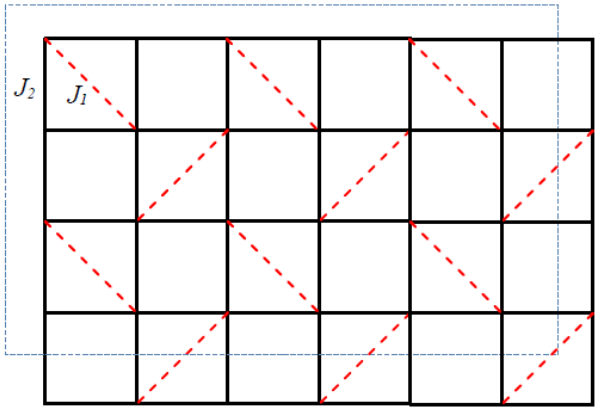

Fig. 1: 24-spin cluster the Shastry-Sutherland lattice under the periodic boundary condition.

Effects of deficit on quantum spin systems

Chitoshi YASUDA
Department of Physics and Earth Sciences, Faculty of Science, University of the Ryukyus, Okinawa 903-0213, Japan

In relation to spin-Peierls materials, the dilution effect of the ground state in a square-lattice antiferromagnetic Heisenberg model with bond-alternating chains of spin size $S = 1/2$ is studied using a quantum Monte Carlo method [1-4]. In the antiferromagnetic long-range ordered phase of the system without bond alternation, the finite staggered magnetization decreases monotonically with increasing the concentration of site dilution, and reaches zero at the percolation threshold. On the other hand, in the dimer phase, the finite staggered magnetization is induced by dilution. Interestingly, near the parameter where a quantum phase transition between the dimer and antiferromagnetic long-ordered phases is driven in the pure system, it has been reported that the staggered magnetization does not decrease due to site dilution but increases once, even though the phase is antiferromagnetic long-ordered phase [1]. It is already known that the spin correlations increase around the diluted site, but the details of this phenomenon and its relation to the magnetization are not clear.

In this project, we investigate deficit effects of the ground state in the antiferromagnetic Heisenberg model consisting of bond-alternated chains on a square lattice using quantum Monte Carlo and exact diagonalization methods. First, we confirmed that the same increase in staggered magnetization is observed in the bond diluted system for the parameters where the increase in staggered magnetization occurs as reported for the site diluted system. Next, the correlation functions at nearest bonds of the diluted bond were examined in the one- and two-dimensional systems, and it was confirmed that the magnitudes of the correlation functions increase in both systems compared to the system without diluted bonds. The increase is larger for the bond alternation parameter close to the phase-transition point to the dimer phase. Furthermore, the correlation functions on the bonds around the diluted bond increase significantly as the bond with the larger exchange integral is diluted. In small-size system with one diluted bond, the ground state itself was investigated by the exact diagonalization method. The ground state consists of a basis with zero eigenvalues for all spin operators, and the weights of the basis, where there is 'no staggeredness' and the spin state on the bond with an enhanced correlation function is antiferromagnetic, are increased due to dilution. Finally, in order to investigate the relationship between the staggered magnetization and the correlation function regarding increase, we examined the change in the distribution of the correlation function with dilution in a randomly diluted bond system. The results show that the change in the correlation function of the nearest-neighbor bond due to dilution contributes significantly to the change in the staggered magnetization.

References

[1] C. Yasuda, S. Todo, M. Matsumoto, and H. Takayama, Phys. Rev. B **64**, 092405 (2001).

[2] C. Yasuda, S. Todo and H. Takayama, J. Phys. Soc. Jpn. **75**, 124704 (2006).

[3] C. Yasuda and S. Miyara, J. Phys. Soc. Jpn. **87**, 014704 (2018).

[4] S. Miyara and C. Yasuda, J. Phys. Soc. Jpn. **87**, 104702 (2018).

Magnetism in the multiple-spin exchange model on a honeycomb lattice

Chitoshi YASUDA
Department of Physics and Earth Sciences, Faculty of Science, University of the Ryukyus, Okinawa 903-0213, Japan

New quantum spin liquid is experimentally observed in the solid ^{3}He layer. This layer is a first monolayer of graphite coated with a bimolecular layer of deuterated molecular hydrogen. It was suggested that there exists a quantum spin liquid with novel dependences of the heat capacity and the magnetic susceptibility on temperature at low density of ^{3}He. This quantum spin liquid has a different behavior from that of conventional two-dimensional solid ^{3}He and is expected to provide new insights into quantum spin liquids. Compared to solid helium thin films that form a triangular lattice, the commensurate solid layer is stabilized at a lower density, suggesting that ^{3}He atoms may form a honeycomb lattice. A commensurate solid layer in conventional two-dimensional solid ^{3}He is well described by the spin-1/2 multiple-spin exchange model on a triangular lattice, and theoretical researches have been done using various methods [1,2,3].

In this project, we research the multiple-spin exchange model with the two-spin and six-body ring exchange interactions on a honeycomb lattice using numerical methods. Ground states are investigated within the mean-field approximation, quantum fluctuations are neglected, and spin operators are treated as a unit vector. Thus, the problem becomes that of minimalization of the classical ground-state energy. The ground-state phase diagram parametrized by the two-spin exchange integral and the external magnetic field with respect to the six-spin exchange integral is investigated using the conjugate gradient (CG) method. In this method, calculations are performed in finite-size systems with a periodic boundary condition. In the CG method, the lowest energy state can be found by continuously searching for spin states from a given initial state. We prepared approximately 500–1000 random spin states as the initial states in addition to some expected states. Thus, we could find unexpected phase transitions by the CG method.

In the region where the contribution of the six-body exchange interaction is large, the eight-sublattice structure with only one nearest-neighbor correlation function and a finite sublattice scalar chirality is stabilized as the ground state in the zero magnetic field system. When the applied magnetic field is increased, the eight-sublattice structure changes to the 5u1d state via the intermediate state. In the 5u1d state, five of the six spins at vertices of a hexagon are parallel to and one is antiparallel to the magnetic field. The phase transition lines between the intermediate and eight-sublattice structure phases and between the intermediate and 5u1d phases depend on the system size. In this project, we examined the dependences of the intermediate phases on the system size in the details.

References

[1] C. Yasuda, D. Kinouchi, K. Kubo, J. Phys. Soc. Jpn. **75**, 104705 (2006).

[2] C. Yasuda, Y. Uchihira, S. Taira, K. Kubo, J. Phys. Soc. Jpn. **87** 104704 (2018).

[3] S. Taira, C. Yasuda, T. Momoi, K. Kubo, J. Phys. Soc. Jpn. **88** 014701 (2019).

Superconducting critical temperature and gap structure of kappa-type BEDT-TTF superconductors

Harald JESCHKE
Research Institute for Interdisciplinary Science, Okayama University
3-1-1 Tsushima-naka, Kita-ku, Okayama 700-8530

We have performed calculations for BEDT-TTF based superconductors with different anions using the fluctuation exchange approximation. The results are not yet fully analyzed, though, and will be reported in a later report. In parallel, we have obtained very good results for the ferromagnet $CrGeTe_3$. Initially, we tried to apply spin fluctuation theory to its sister compound $CrSiTe_3$ to investigate the reported superconducting phase under pressure. However, due to conflicting reports on the high pressure crystal structure, these calculations are incomplete. We investigated the pressure-induced evolution of the electronic and magnetic properties of $CrGeTe_3$. Using density functional theory (DFT) and dynamical mean-field theory (DMFT), we explored the transition from a low-temperature semiconducting ferromagnet to a near room-temperature metallic ferromagnet under pressure (Xu *et al.*, Phys. Rev. B **108**, 125142 (2023)). This was achieved using DCore on System B. We complement our calculations with experimental optical conductivity data, which trace the evolution of electronic correlations through the insulator-to-metal transition. As pressure increases, a distinct mid-infrared (MIR) feature emerges in the optical conductivity, signaling the development of strong orbital-selective correlations. In combination, our results reveal that the double-exchange mechanism plays a key role in stabilizing near room-temperature ferromagnetism in $CrGeTe_3$ [1]. Additionally, we explore the anomalous Hall effect (AHE) in $CrGeTe_3$ [2]. There, a discrepancy between calculations and experiment arises. We conclude that the AHE is primarily driven by extrinsic mechanisms and outline potential scenarios for these extrinsic contributions.

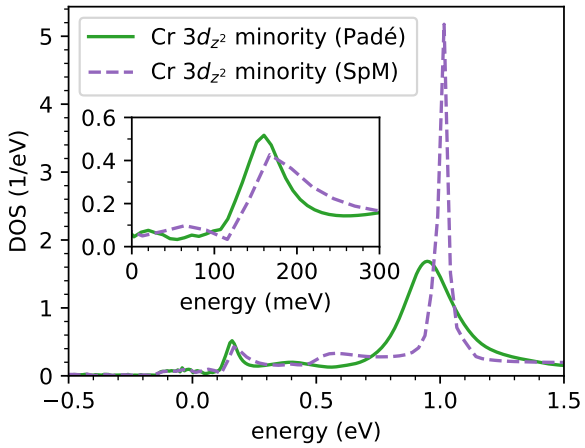

Figure 1: DFT+DMFT spectral function for the minority spin Cr $3d_{z^2}$ orbital of $CrGeTe_3$ at $T = 100\,\mathrm{K}$, $P = 5\,\mathrm{GPa}$ in the ferromagnetic state, explaining the mid-infrared feature.

References

[1] J. Ebad-Allah, D. Guterding, M. Varma, M. Diware, S. Ganorkar, H. O. Jeschke, and C. A. Kuntscher: Phys. Rev. B **111**, L140402 (2025).

[2] G. Scharf, D. Guterding, B. Hen, P. M. Sarte, B. R. Ortiz, G. Kh. Rozenberg, T. Holder, S. D. Wilson, H. O. Jeschke, and A. Ron: Phys. Rev. Res. **7**, 013127 (2025).

Information analysis of complex system with a tensor network formalism

Kenji HARADA
Graduate School of Informatics, Kyoto University
Kyoto 606-8501, Japan

Building on the tensor tree network framework combined with the Born machine approach [1], we propose a general method for constructing a generative model that expresses the target distribution as the amplitude of a quantum wave function represented by a tensor tree [2]. The core idea is to optimize the tree structure to minimize bond mutual information dynamically. This method enhances performance and reveals hidden relational structures within the target data.

Our results indicate that this generative model outperforms conventional methods, particularly in scenarios where the data structure is unknown. Moreover, following the learning and optimization process, the optimized tree structure provides valuable insights into the sometimes obscured relational data structure.

For example, the Global Industry Classification System categorizes stocks into 11 sectors. In our analysis, we input the stock price data of S&P 500 companies into the generative model without prior knowledge of these sector classifications. Figure 1 depicts the optimized network structure with a bond dimension 5. In the figure, the color of each circle represents the sector to which the corresponding company belongs. Companies within the same sector tend to cluster closely, forming predominantly single-colored sub-trees. Importantly, the sector information was not utilized in the learning process; the observed clustering is purely a result of the model's learning.

Therefore, the proposed method automatically learns the hidden relational target data structure and reflects it in the network structure, making it a powerful tool for data analysis even without prior knowledge of the information structure.

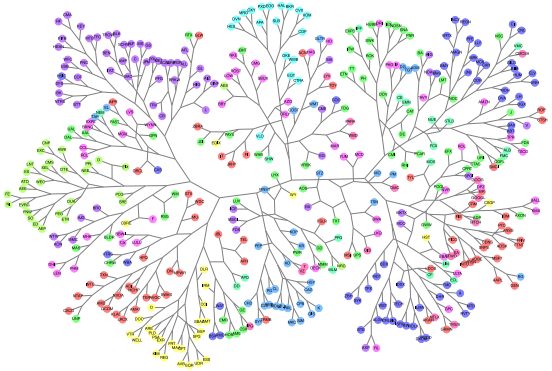

Figure 1: Optimized network structure of S&P 500 companies. The color of each circle indicates the sector to which the corresponding company belongs.

References

[1] Zhao-Yu Han, Jun Wang, Heng Fan, Lei Wang, and Pan Zhang. Unsupervised Generative Modeling Using Matrix Product States. *Phys. Rev. X*, 8(3):031012, 2018.

[2] Kenji Harada, Tsuyoshi Okubo, and Naoki Kawashima. Tensor tree learns hidden relational structures in data to construct generative models. *Machine Learning: Science and Technology*, 6(2):025002, 2025.

Physical properties of crosslinked polymer networks through network topology analysis

Katsumi HAGITA,[1] and Takahiro MURASHIMA[2]

[1]*Department of Applied Physics, National Defense Academy, Yokosuka 239-8686*

[2]*Department of Physics, Tohoku University, Sendai 980-8578*

To elucidate the topological effect on the physical/mechanical properties of the tetra-arm end-link gel/rubber, it is desirable to establish model approaches using coarse-grained MD (CGMD) simulations of the Kremer-Grest model with bond breakage. Here, the bond breakage has a critical importance to describe the behaviors of inhomogeneous networks under stretching.

In this project, the quartic function (1) was used as the bond potential instead of the FENE potential in Kremer-Grest model.

$$U_O(r) = K(r - R_c)^2(r - R_c - C_1)(r - R_c - C_2) + U_0 \quad (1)$$

We performed systematic reparameterization for this quartic function bond in order to realize tunable bond breakage strength (For details on the parameters, see reference [1].) as shown in Fig. 1.

First, we investigated the stress-strain (SS) curves of the diamond lattice with bimodal length between neighboring crosslink points [1]. Figure 2 shows the SS curve for the networks with ($N_s - N_b$, $N_s + N_b$) = (25, 25), (20, 30), (15, 35), (10, 40), and (5, 45). For larger N_b, the SS curve becomes more collapsed shape due to larger the network inhomogeneity.

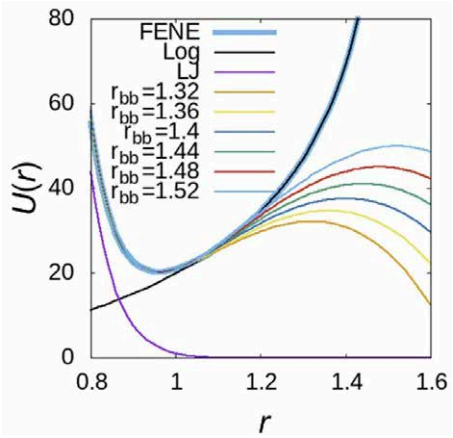

Fig. 1: Bond potential for Kremer-Grest model with bond breakage. r_{bb} is a parameter to characterize the bond breakage strength.

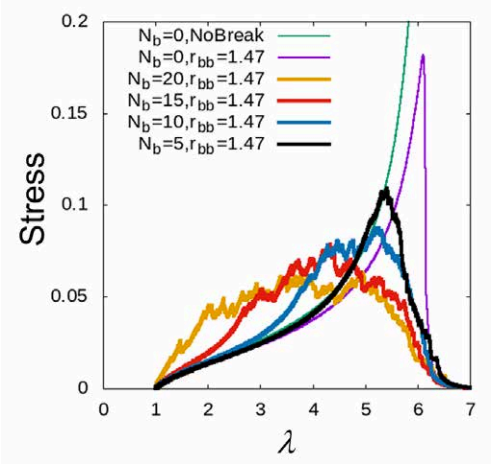

Fig. 2: Stress-strain curves for the networks with ($N_s - N_b$, $N_s + N_b$) = (25, 25), (20, 30), (15, 35), (10, 40), and (5, 45).

Second, we investigate SS curves of AB type tetra-arm gel for various reaction polymer concentrations [2]. For comparison, we obtained the various tetra-functional networks through pseudo reaction process for various pre-polymers. As a result, it was found that when the reaction polymer concentration was lower than the overlapping concentration, the [AB] type had superior toughness compared to the others, as shown in Fig. 3.

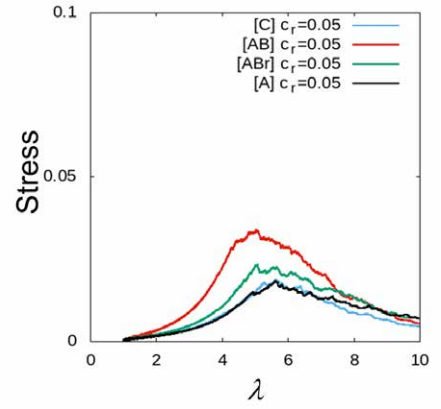

Fig. 3: Stress-strain curves of the various tetra-functional networks.

Thirdly, to study abnormal butterfly patterns of stretched inhomogeneous networks, we evaluated small angle behaviors of two-dimensional scattering patterns (2DSPs) [3]. We studied the calculation method of 2DSPs by using the ISSP supercomputer. Notably, these simulations were performed by using the supercomputer FUGAKU because the huge system size is required for sufficient resolution of 2DSPs. For future basic science, the ISSP supercomputer is used to investigate the basic characteristics of the smaller system size.

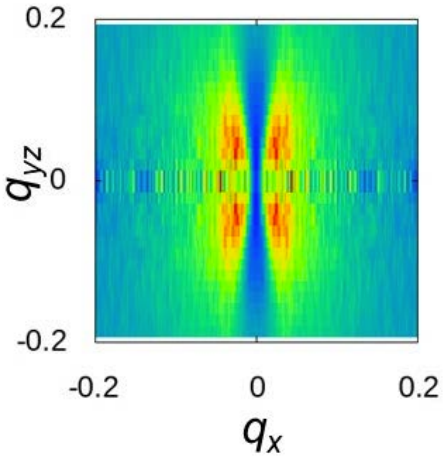

Fig. 4: 2DSP of the AB-type tetra-arm network stretched at the strain of 5.0.

In this project, we aim to quantitatively relate the KG model with the All-atom model in order to improve the connectivity between the KG model and the real world. In order to efficiently measure the correspondence, we have also considered the Martini coarse-grained force field, keeping in mind that large-scale all-atom calculations will be required for the analysis.

References

[1] K. Hagita, T. Murashima, Macromolecules, **57**, 10903–10911 (2024).

[2] K. Hagita, T. Murashima, Macromolecules, in revision.

[3] K. Hagita, T. Murashima, Macromolecules, (2025) doi:10.1021/acs.macromol.5c00207

Study of magnetic excitations in Cuprates and Iridates using MPS-based simulations

Matthias GOHLKE, Jiahui BAO
Theory of Quantum Matter Unit, Okinawa Institute of Science and Technology
1919-1 Tancha, Onna-son, Okinawa 904-0495

Cuprate materials, such as La_2CuO_4, are prototypical examples of two-dimensional antiferromagnetic Mott insulators and serve as parent compounds for high-temperature superconductors [2, 3]. The magnetism in these systems is governed by strong electron correlations, and their low-energy excitations are well described by spin models derived from the Hubbard model in the large-U limit [4, 5]. The basic picture begins with a Heisenberg antiferromagnetic model, but experimental evidence, particularly from inelastic neutron scattering (INS) and resonant inelastic x-ray scattering (RIXS), reveals features such as magnon dispersion along the Brillouin zone boundary and high-energy continua that cannot be captured by simple models alone [6, 7]. These observations have motivated more sophisticated approaches incorporating cyclic four-spin exchange and beyond-linear spin wave corrections.

In our work [1], we have revisited an effective spin model used to describe magnons in cuprate materials such as La_2CuO_4, $CaCuO_2$, as well as the iridate Sr_2IrO_4, which exhibit strong spin-orbit coupling. Although previous works already include higher-order terms such as ring-exchange when deriving an effective spin model from the one-band Hubbard model, these studies are based on linear spin wave theory (LSWT), which is known to have limitations when quantum fluctuations are significant. Here, we instead use the matrix product state (MPS) framework and time domain variational principle (TDVP) to compute the dynamical spin structure factor of an effective spin model that includes cyclic ring exchange and interactions up to third-nearest neighbors. In comparing to LSWT and LSWT with $1/S$ corrections, we are able to quantify the discrepancy of LSWT and estimates based thereon.

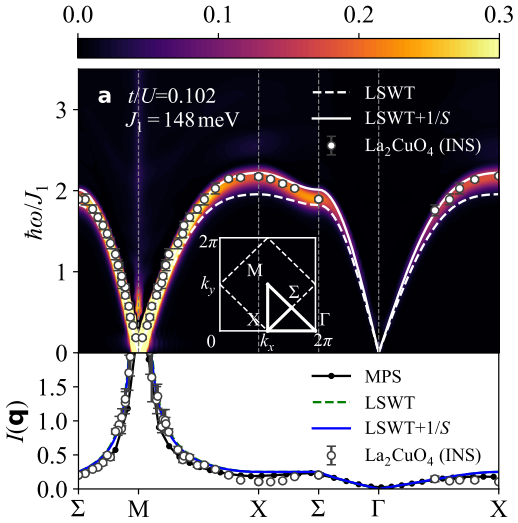

Figure 1: Magnon spectra of La_2CuO_4 compared with LSWT and LSWT+$1/S$ results of an effective spin model derived from a one-band Hubbard model.

Our key findings are: (i) MPS-based calculations provide more accurate predictions for magnon dispersion and intensities, showing very good agreement with experimental data for La_2CuO_4. (ii) LSWT and its variants systematically overestimate exchange parameters and the ratio t/U of Hubbard hopping t and potential U. (iii) We propose an empirical

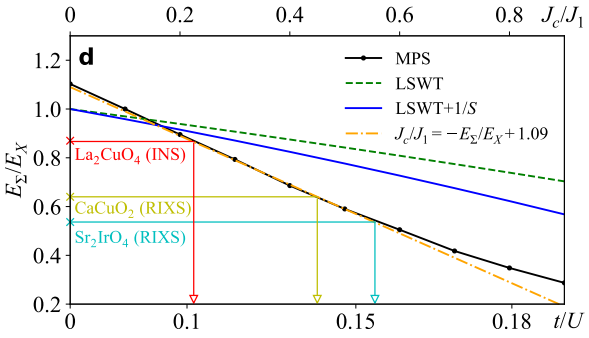

Figure 2: Ratio of excitation energies at $\mathbf{q}_\Sigma = (\pi/2, \pi/2)$ and $\mathbf{q}_X = (\pi, 0)$, showing their scaling with $J_c/J_1 \sim t^2/U^2$.

relation to estimate t/U from experimentally observed magnon energies at high-symmetry points.

Moreover, we find that while the effective spin model, if treated fully quantum, describes the magnon spectrum, it fails to capture the high-energy continuum found in experiments at $q_X = (\pi, 0)$. We argue that this discrepancy is due to limitations of the effective spin model and the underlying one-band Hubbard model. Additional physical phenomena (e.g., higher-order charge fluctuations, spin-phonon coupling, etc.) might be required to explain the observed continuum in cuprate antiferromagnets.

This work has relied heavily on the open source MPS and DMRG package *TenPy* [8] providing parallelization of matrix operations within a single node through optimized LAPACK and BLAS packages.

References

[1] J. Bao, M. Gohlke, J. G. Rau and N. Shannon, PRR **7** L012053 (2025).

[2] J. G. Bednorz and K. A. Müller, Zeitschrift für Physik B **64** 189 (1986).

[3] P. W. Anderson, Science **235** 1196 (1987).

[4] M. Takahashi, J. Phys. C: Solid State Phys. **10** 1289 (1977).

[5] A. H. MacDonald, S. M. Girvin, and D. Yoshioka, PRB **37** 9753 (1988).

[6] R. Coldea et al., PRL **86** 5377 (2001).

[7] N. S. Headings, S. M. Hayden, R. Coldea, and T. G. Perring, PRL **105** 247001 (2010).

[8] J. Hauschild, and F. Pollmann, SciPost Phys. Lect. Notes 5 (2018).

RIXS spectrum of CuO_2 spin chain

Hiroaki ONISHI
Advanced Science Research Center, Japan Atomic Energy Agency, Tokai, Ibaraki 319-1195

Frustrated quantum magnets often exhibit non-trivial ground states that do not have a classical analogue. The spin nematics, which is characterized by spin quadrupoles, is a prominent example. We have studied the excitation dynamics of a spin nematic liquid state in a spin-1/2 J_1-J_2 chain with ferromagnetic J_1 and antiferromagnetic J_2 in a magnetic field using dynamical DMRG [1]. We find gapless longitudinal and gapped transverse spin excitation spectra, in accordance with quasi-long-range longitudinal and short-range transverse spin correlations, respectively. The quadrupole channel exhibits gapless excitations, signaling quasi-long-range antiferro-quadrupole correlations. These properties are useful to identify the spin nematic liquid state by experiments. However, conventional magnetic probes are usually insensitive to spin quadrupoles. In this context, we expect that resonant inelastic x-ray scattering (RIXS) would provide a route to detect spin quadrupole excitations [2].

In this study, we introduce an effective t-J model for an edge-shared CuO_2 spin chain, which gives the J_1-J_2 chain such as $LiCuVO_4$, and analyze RIXS spectra based on the Kramers-Heisenberg formula by Lanczos diagonalization. Parallel computations with OpenMP were done on the system B of the ISSP supercomputer.

In Fig. 1, we present the intensity plot of oxygen K-edge RIXS spectra at zero field. We find excitation continuum above a sinusoidal mode dispersing from $q = \pi/2$, which corresponds to the des Cloizeaux-Pearson mode of the spin excitation. Moreover, we find spectral

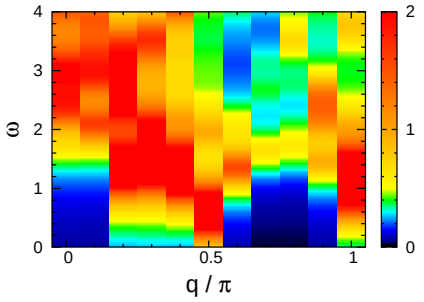

Figure 1: Oxygen K-edge RIXS spectra of the CuO_2 spin chain, by Lanczos calculations with 20 sites, $J_1 = -1$, and $J_2 = 1$ at zero field.

weight in a wide range of ω at $q = \pi$, which is not due to the spin excitation but attributed to spin quadrupole excitations. If we increase the magnetic field, the gapless position of q moves toward zero, while the spectral weight at $q = \pi$ remains large (not shown). These suggest that the RIXS spectra would contain characteristics of both spin and spin quadrupole excitations. To analyze large system sizes, the coding of a dynamical DMRG program is in progress.

References

[1] H. Onishi, J. Phys. Soc. Jpn. **84**, 083702 (2015); J. Phys.: Conf. Ser. **592**, 012109 (2015); Physica B **536**, 346 (2018); J. Phys.: Conf. Ser. **2207**, 012045 (2022).

[2] M. W. Haverkort, Phys. Rev. Lett. **105**, 167404 (2010); L. Savary and T. Senthil, arXiv:1506.04752.

Kinetics of phase transition and polyamorphism

Kazuhiro FUCHIZAKI
Department of Physics, Ehime University, Matsuyama 790-8577

Extensive studies on polyamorphism have been carried out following an astonishing discovery of the liquid-liquid transition (LLT) of black phosphorus (bP) upon increasing pressure [1]. Efforts dedicated to understanding water polyamorphism started in the last century have been a driving force. A first-principles molecular dynamics study predicted that the LLT is a pressure-induced molecular-to-polymerized liquid [2].

Although the thermodynamic understanding of the water-type polyamorphism has been solidified [3], further experimental verification regarding bP's LLT has never been performed. The discovery of the LLT was expected because of bP's unusual melting feature, i.e., a melting maximum [4]. However, a melting maximum is not necessary for exhibiting an LLT. Instead, a singularity at which the slope of a melting curve abruptly changes could be a triple point between two liquid and crystalline phases [5]. Indeed, the most recent experimental research unveiled that the bP's melting curve does not have a maximum but such a singularity. Although the crystalline structures for the ambient- and high-pressure phases have been resolved to be known as A17 and A7 structures, respectively [6], the relationship between those crystalline- and liquid-phase structures has not been clarified yet.

Our research aims to establish the expected relationship between polymorphism and polyamorphism in bP and clarify the melting aspects of crystalline phases. For this aim to be achieved, a system consisting of one component, i.e., P, may be appropriate. The first task should be constructing reliable models that reproduce the A17 and A7 structures. Those models can also determine the phase boundary and the melting curves, which are to be compared with experimentally known results [7] to ensure the reliability of the models.

In FY2024, we aimed to establish the force-field models that can predict the A17–A7 phase boundary as a machine-learning (ML) potential. Such an ML potential is extensively discussed in physics, chemistry, and materials science. Here, considering the high compatibility of the Behler-Parrinello (BP) symmetric functions [8], carrying the intra- and intermolecular interactions, with subsequent molecular dynamics (MD) or Monte Carlo (MC) simulations, we adopted the high-dimensional neural network potential [8], abbreviated as BPNN in the following.

We first carried out the first-principles calculations to prepare a set of learning data using Quantum Espresso installed in System B.

For the A17 structure, we thus obtained the ground state energies for the structures in a pressure range between 0.10 and 6.05 GPa using available CIF files [9]. A combination of the hybrid functionals [10] and PAW [11], giving rise to -55 Ry ($\simeq -750$ eV)/atom, which was almost pressure-independent, was employed for the calculations. In order to obtain the potential energy surface (PES), the BPNN consisting of 24 symmetry functions was trained 2000 times using the QE-based energies calculated for a set of 9720 unit cells, which were made to be compatible with the experimentally found equation of state, as input. The process almost converged at around 1000 times of learning, giving rise to ~ 0.16 eV

per phosphorus atom for the loss function.

Similar QE calculations were also made for the A7 structure in a pressure range between 6.05 and 10.23 GPa using two kinds of CIF files available [12]. However, a pressure at which the energy becomes comparable with that of A17 was not found. Therefore, we constructed the symmetry-adapted A7 structures "by hand" to recalculate the energies. The lattice constants were assumed to vary linearly according to pressure. We could then find the A7 structure, whose energy equals that of A17 at ~ 5 GPa. This pressure almost agrees with the pressure when the experimentally known A17–A7 phase boundary [13] is extended to zero temperature. Thus, we prepared 9882 unit cells around the structure at 5 GPa to be provided to QE to obtain their energies. These energies were input to the BPNN to assess the A7 PES. The result again converged halfway through the whole 2000 processes of learning. The maximum loss was 0.13 eV per phosphorus atom.

Having thus established the PESs for the A17 and A7 structures in terms of BP symmetry functions [8], we are now ready to carry out classical MD or MC simulations to achieve the aim mentioned at the beginning.

Finally, it should be mentioned that we quantum chemically [14] examined the polymerization process of P_4 tetrahedral molecules [15] in the low-density liquid (LDL) phase upon the pressure-induced LLT to the high-density liquid (HDL) phase. The energy barrier for a P_4 molecule to break up a single bond to be radically polymerizable is ~ 4 eV per molecule. Polymerized $(P_4)_n$ is energetically stable and costs negligible energy for polymerization beyond $n = 3$. Therefore, once P_4 molecules are polymerized, the reverse reaction would not occur at around 1500 K, the LLT temperature. Thus, the LDL and HDL comprise not a pseudo-binary but a binary system. Four radical P_4 molecules form, as the energetically stable state, a layered structure, which must share the structural feature with A7.

References

[1] Y. Katayama *et al.*: Nature **403**, 170 (2000).

[2] T. Morishita: Phys. Rev. B **66**, 054204 (2002).

[3] M. A. Anisimov *et al.*; Phys. Rev. X **8**, 011004(2018).

[4] E. Rapoport: J. Chem. Phys. **46**, 2891 (1967).

[5] K. Fuchizaki: J. Chem. Phys. **139**, 244503 (2013).

[6] Y. Akahama *et al.*: Phys. Rev. B **61**, 3139 (2000).

[7] V. L. Solozhenko and V. Turkevich: J. Phys. Chem. C **127**, 6088 (2023).

[8] J. Behler and M. Parrinello: Phys. Rev. Lett. **98**, 146401 (2007).

[9] J. B. Herbert *et al.*: J. Appl. Cryst. **49**, 277 (2016).

[10] J. P. Perdew *et al.*: J. Chem. Phys. **105**, 9982 (1996).

[11] F. Jollet *et al.*: Comput. Phys. Commun. **185**, 1246 (2014).

[12] C. R. Groom *et al.*: Acta Crystallogr. B: Struct. Sci. Cryst. Eng. Mater. **72**, 171 (2016).

[13] D. Scelta *et al.*: Chem. Commun. **54**, 10554 (2018).

[14] M. J. Frisch et al.: GAUSSIAN 09 Revision E.01, Gaussian, Inc., Wallingford, CT, 2009.

[15] P. Ballone and R. O. Jones: J. Chem. Phys. **121**, 8147 (2004).

Mathematical crystal chemistry

Ryotaro Koshoji
Institute for Solid State Physics, University of Tokyo
Kashiwa-no-ha, Kashiwa, Chiba 277-8581

I have developed the algorithm to design structural prototypes of inorganic crystals. The huge coordination space of the spatial order of atoms makes it difficult to predict crystal structures from chemical compositions. While many researchers have pursued the numerical techniques such as mathine learning methods to accelerate the discovery of the most stable structure, I focus on the inorganic structural chemistry that describes the structural principles of inorganic molecules and solids. In 1929, Pauling summarizes the principles of determining the structures of inorganic crystals. As George *et al.* showed that oxides satisfying all the Pauling's rules simultaneously are minority [J. George *et al.*, Angewandte Chemie International Edition **59**, 7569 (2020)], the predictive power of the Pauling rules is limited, but the rules offer the basic concepts for inorganic structural chemistry.

The goal of mathematical crystal chemistry is to give the definite rules to design the structural prototypes of inorganic crystals in place of the Pauling rules [1,2]. The concept is shown in Fig. 1. The rules are mathematically formalized by equality or inequality constraints in mathematical optimization problem, which has the form

$$\begin{aligned} \text{minimize} \quad & f_0(\boldsymbol{x}) \\ \text{subject to} \quad & f_i(\boldsymbol{x}) \leq 0 \quad i = 1, \cdots n \\ & h_j(\boldsymbol{x}) = 0 \quad j = 1, \cdots m \end{aligned}$$

Here the vector $\boldsymbol{x}$ is the optimization variable of the problem. The form of mathematical optimization problem suits to the expression of crystal structures that are the global optimum satisfying all the constraints corresponding to the competitive rules.

The first rule of mathematical crystal chemistry is the definition of interatomic forces. Since interatomic forces stabilize a crystal structure by keeping all the interatomic distances within the stable ranges, they are defined as the geometrical constraint G that constrains the feasible interatomic distance as

$$d_{ij\boldsymbol{T}}^{(G)} \leq |\boldsymbol{x}_j + \boldsymbol{T} - \boldsymbol{x}_i| \leq D_{ij\boldsymbol{T}}^{(G)}, \tag{1}$$

where $d_{ij\boldsymbol{T}}^{(G)}$ and $D_{ij\boldsymbol{T}}^{(G)}$ are the minimum and maximum distances between atom i and atom j in lattice $\boldsymbol{T}$, respectively, with $\boldsymbol{x}_i$ and $\boldsymbol{T}$ being the cartesian coordinate of atom i in the original cell and the lattice vector, respectively. The second rule is the definition of $d_{ij\boldsymbol{T}}^{(G)}$ and $D_{ij\boldsymbol{T}}^{(G)}$. Since inorganic structural chemistry estimates a chemical bonding distance as the sum of atomic radii, mathematical crystal chemistry defines the minimum and maximum interatomic distances as

$$d_{ij\boldsymbol{T}}^{(G)} = r_i^{(G)} + r_j^{(G)}, \tag{2}$$

$$D_{ij\boldsymbol{T}}^{(G)} = R_i^{(G)} + R_j^{(G)}, \tag{3}$$

where $r^{(G)}$ and $R^{(G)}$ are the minimum and maximum atomic radii depending on the type of the geometrical constraint G, respectively. The third rule describes how to create chemical bonds between atoms, for exaple, an ionic bond is formed if the interatomic distance between an anion and a cation satisfies the inequality constraint of Eq. (1). The previous study [2] introduces the creatability function

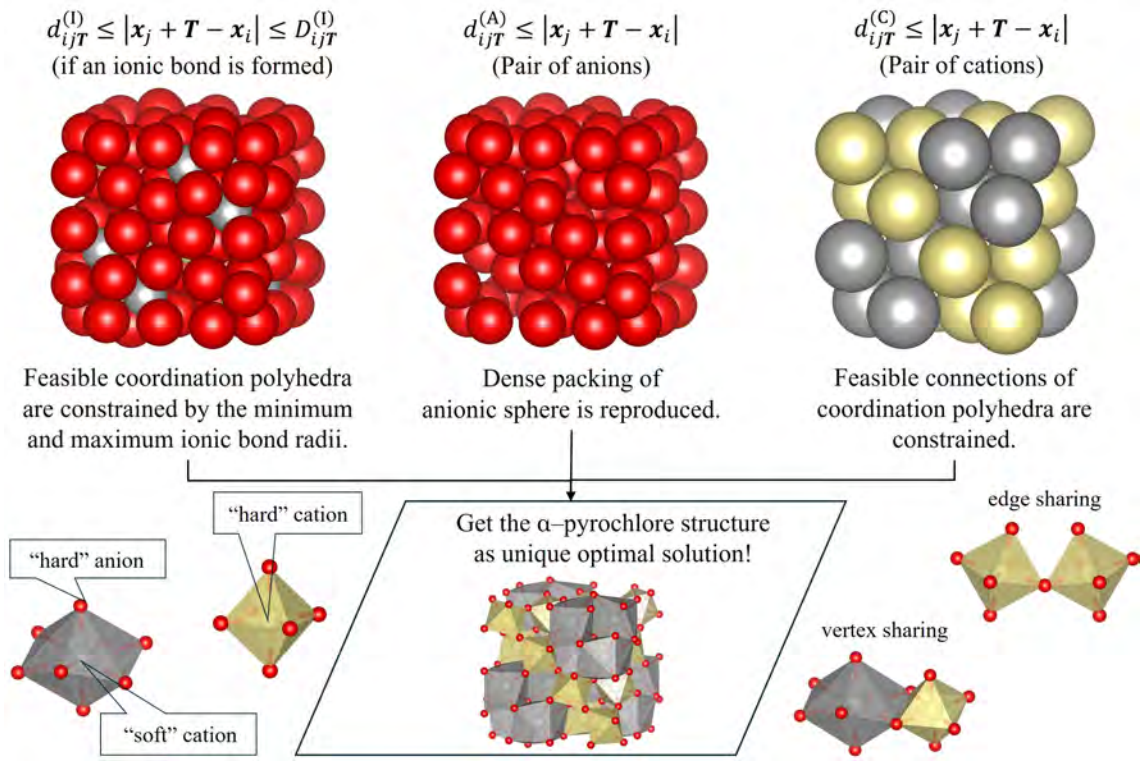

Figure 1: Concept of mathematical crystal chemistry.

$\Lambda_{ij\boldsymbol{T}}^{(\mathrm{G})}$ that returns one or more if the geometrical constraint G is creatable. Accordingly, the putative mathematical optimization problem [1,2] to design structural prototypes of inorganic crystals are given by

$$
\begin{aligned}
\text{minimize} \quad & \Omega \\
\text{subject to} \quad & (1-\varepsilon)\, d_\sigma \le x_\sigma \le (1+\varepsilon)\, D_\sigma \\
& d_\sigma = \max_G \left[n_\sigma^{(G)} \left(r_i^{(G)} + r_j^{(G)} \right) \right] \\
& D_\sigma = \min_G \left[n_\sigma^{(G)} \left(R_i^{(G)} + R_j^{(G)} \right) \right]. \\
& \sum_G n_\sigma^{(G)} = 1 \\
& n_\sigma^{(G)} \in \{0, 1\} \\
& n_\sigma^{(G)} \le \Lambda_\sigma^{(G)} (\boldsymbol{\Phi}, \varepsilon)
\end{aligned}
$$

Additionally, in the previous study [1,2], the coordination number of each cation is fixed as

$$\sum_{j,\boldsymbol{T}} \chi_j^{(\mathcal{E})} n_\sigma^{(\mathrm{I})} = N_{i\mathcal{E}}^{(\mathrm{I})}. \tag{4}$$

First, supercomputer Ohtaka was mainly used to apply the mathematical model to crystal structure prediction. As a result, it identified unique optimal solutions corresponding to the structures of spinel, pyrochlore (α and β), pyroxene, quadruple perovskite, cuprate superconductor $YBa_2Cu_3O_{7-x}$, and iron-based superconductor LaFeAsO. Second, oxide crystals registered in ICSD are analyzed whether they can be the optimal solutions. Notably, up to 95% of oxide crystal structure types in ICSD align with the optimal solutions preserving experimental structures despite the discretized feasible atomic radii. The successful results strongly imply that the mathematical optimization problem deserves to be the mathematical foundation of the principles determining the structures of inorganic crystals.

References

[1] R. Koshoji and T. Ozaki: Phys. Rev. Mater. **8**, 113801 (2024).

[2] R. Koshoji: arXiv:2503.20273 (2025).

Analyses on the Potential-dependent Dynamics of Ionic Liquid Electrolytes Forming Electric Double Layers Facing the Electrodes

Ken-ichi FUKUI

Department of Materials Engineering Science, Graduate School of Engineering Science, Osaka University, Machikaneyama, Toyonaka, Osaka 560-8531

Ionic liquids (ILs) are promising electrolytes for electrochemical devices such as secondary battery, capacitor, etc., due to their high chemical stability with negligible vaporization. Structuring and dynamics of the interfacial IL faced to charged graphite electrodes have been analyzed by molecular dynamics (MD) calculations [1], but the transport of Li^+ ion inside EDL formed at negatively charged electrode is not apparent because Li^+ coordinated with anions has negative charge in total. In the present study, we have analyzed the transport of Li^+ ion inside EDL of BMIM-TFSI electrolyte at the negatively charged graphite electrode by MD calculations, which is closely related to charging process of Li-ion battery composed of these components.

All MD simulations were conducted by classical MD package of LAMMPS. A simulation cell in Fig. 1(a) contains 650 ion pairs of BMIM-TFSI with randomly distributed 150 pairs of Li-TFSI ($9\times8\times11$ nm^3) sandwiched with 5-layer graphite electrodes from top and bottom separated with vacuum layer. Same amounts of positive and negative charges were assigned to the top and bottom electrode, respectively at the graphene layer faced to the electrolyte reproducing the electrified interfaces. Two different applied potential sequences were compared in the present study; (i) firstly stabilized the interface structure by annealing the cell at the surface charge equivalent to ±1.8 V and then the surface charge equivalent to ±3.5 V was applied (lower case in Fig. 1(b)) and (ii) the surface charge equivalent to ±3.5 V was directly applied (upper case in Fig. 1(b)). 10 ns MD trajectories at 350 K were analyzed.

Apparent difference was found for the interface structure at the electrode potential of -3.5 V depending on the applied potential sequences (Fig. 1(b)). By the sequence (ii), no Li^+ was present at the electrode. By analyzing the MD trajectories, it was due to the dense BMIM cation layers already formed by equilibrium at -1.8 V, which prevent the exchange of Li^+ at least during 10 ns. In the sequence (i), the interface is rather randomized and provide the chance for some Li^+ to be attach to the electrode by deforming the coordination with TFSI anions in 10 ns.

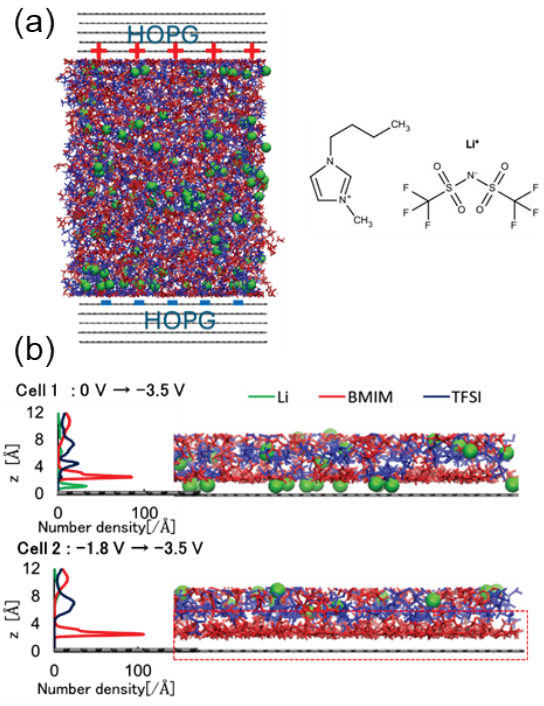

Fig. 1 (a) Simulation cell. (b) Interface structure at -3.5 V vs. PZC depending on the deferent applied potential sequences.

Reference

[1] H. Miyamoto, Y. Yokota, A. Imanishi, K. Inagaki, Y. Morikawa, K. Fukui, *Phys. Chem. Chem. Phys.* **20**, 1940 (2018).

Calculation of high dimensional systems at finite temperature using random quantum states of general variational wavefunctions

Toshiaki IITAKA

Center for Computational Science,

RIKEN, 2-1 Hirosawa, Wako, Saitama, 351-0198 JAPAN

Calculation of the thermal average of an observable of a closed quantum many-body system in its thermal equilibrium at an inverse temperature has two major computational difficulties. The number of quantum states to be included and the dimension of each quantum state vector both exponentially increase as the temperature and the system size increases, respectively. Each difficulty has been independently attacked using *random state method* [1, 2] and *variational wave function*, respectively.

Thermal average of observable *A* at inverse temperature β is calculated using *random state* $|\Phi\rangle$ as

$$\langle A\rangle = \frac{tr[e^{-\beta H}A]}{Z} = \frac{\langle\langle\langle\Phi|A|\Phi\rangle\rangle\rangle}{Z}$$

where

$$Z(\beta) = tr[e^{-\beta H}] = \langle\langle\langle\Phi|\Phi\rangle\rangle\rangle$$

is the *partition function* and the double bracket indicates statistical average over random states. The *thermal state* is defined by the imaginary time evolution of the random state.

$$|\Phi(\beta)\rangle = e^{-\beta H/2}|\Phi\rangle$$

Thermal energy E and specific heat C are expressed as $E(\beta) = \langle H\rangle$ and$C(\beta) = \frac{dE(\beta)}{dT}$, respectively.

Variational wave function is a point on a manifold embedded in the Hilbert space,

$$|\psi(w)\rangle = \sum_{\boldsymbol{\sigma}} c(w,\boldsymbol{\sigma})|\boldsymbol{\sigma}\rangle$$

which is parameterized with variational parameters, $w = \{w_i\}$, whose number is much less than the dimension of the Hilbert space.

Thermal variational wave function has been introduced

$$|\Psi(\beta;w)\rangle = e^{-\beta H/2}|\Psi(w)\rangle$$

where $|\Psi(w)\rangle$ is a *linear* variational wave functions such as product state,

MPS, PEPS [3-6] String-Bond States and Entangled Plaquette States [7].with random parameters w. The imaginary time evolution was calculated with stochastic reconfiguration[8, 9]. The program is written with NetKet [10] as well as JAX[11] and Python.

In this project, the formulation has been extended to the product of a random variational wavefunction and a generic variational wavefunction (see Fig. 1).

Scaling up of the calculation up to around 10x10 lattice is planned.

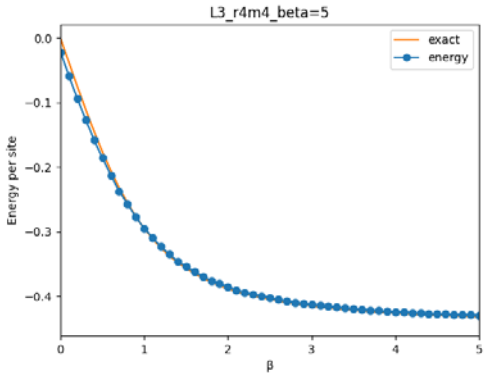

Fig 1. Inverse temperature dependency of the energy of 3x3 square lattice Heisenberg model calculated with 16 samples of the product of restricted Boltzmann machine (α =4) and random phase product states[3].

References

[1] T. Iitaka, and T. Ebisuzaki, Phys. Rev. Lett. **90**, 047203 (2003).

[2] T. Iitaka, and T. Ebisuzaki, Phys. Rev. E **69**, 057701 (2004).

[3] T. Iitaka, arXiv:2006.14459 (2020).

[4] S. Garnerone, T. R. de Oliveira, and P. Zanardi, Phys. Rev. A **81**, 032336 (2010).

[5] A. Iwaki, A. Shimizu, and C. Hotta, Phys. Rev. Res. **3**, L022015 (2021).

[6] S. Goto, R. Kaneko, and I. Danshita, Phys. Rev. B **104**, 045133 (2021).

[7] I. Glasser *et al.*, Physical Review X **8**, 011006 (2018).

[8] S. Sorella, Phys. Rev. Lett. **80**, 4558 (1998).

[9] K. Takai *et al.*, J Phys Soc Jpn **85**, 034601 (2016).

[10] G. Carleo *et al.*, SoftwareX **10**, 100311 (2019).

[11] JAX, https://docs.jax.dev/en/latest/.

Polarized Spin Magnetization Accumulation on Semiconductor Surfaces Under Intense Light Irradiation

Tomohiro Tamaya

Institute for Solid State Physics,

The University of Tokyo, Kashiwa-no-ha, Kashiwa, Chiba 277-8581

This study aims to elucidate the fundamental principles governing polarized spin magnetization that accumulates on semiconductor surfaces under intense terahertz irradiation. Recent progress in high-intensity terahertz sources has reignited interest in strong-field light–matter interactions in semiconductors. The applicant has developed a theoretical framework that concurrently treats intraband and interband transitions of Bloch electrons, uncovering nonlinear optical mechanisms in the nonperturbative regime [1–4]. A central insight is that Bloch electrons, when driven by terahertz fields, remain in a coherent superposition of valence and conduction bands—a quantum pure state—that gives rise to ultrafast, frequency-dependent electric polarization. Unlike conventional spintronics, which typically involves thermally mixed spin states subject to scattering, this approach enables spin magnetization originating from quantum coherence and free from thermal relaxation. This research seeks to clarify and demonstrate the nature and controllability of such quantum-driven spin magnetization through real-space simulations.

To pursue this objective, we conducted large-scale simulations on a representative semiconductor, GaAs, with open boundary conditions imposed along one spatial direction. A strong terahertz electric field was applied, and

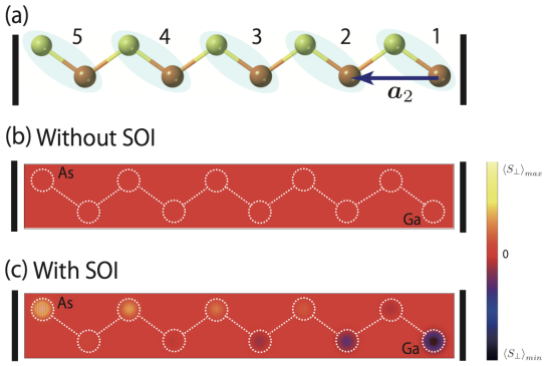

Fig.1: (a) Schematic illustration of the simulation model with five unit cells along the open boundary directions. Orange and green spheres represent As and Ga atoms, respectively. (b) Spatial distribution of spin magnetization at each atomic site without spin–orbit interaction (SOI). (c) Spatial distribution of spin magnetization with SOI.

the resulting spin magnetization accumulation was computed. Figures 1(a)–(c) illustrate: (a) a schematic of the model comprising five unit cells along the open boundary direction; (b) the spatial distribution of spin magnetization at atomic sites in the absence of spin–orbit interaction (SOI); and (c) the corresponding distribution in the presence of SOI. These results reveal that spin magnetization clearly accumulates at the GaAs surface when SOI is present, indicating the emergence of a light-induced spin Hall effect. Additionally, Figure 2 shows the time evolution of spin magnetization components in each unit cell. The observed ultrafast temporal dynamics, synchronized with the incident terahertz field, confirm the generation of dynamically induced polarized spin magnetization.

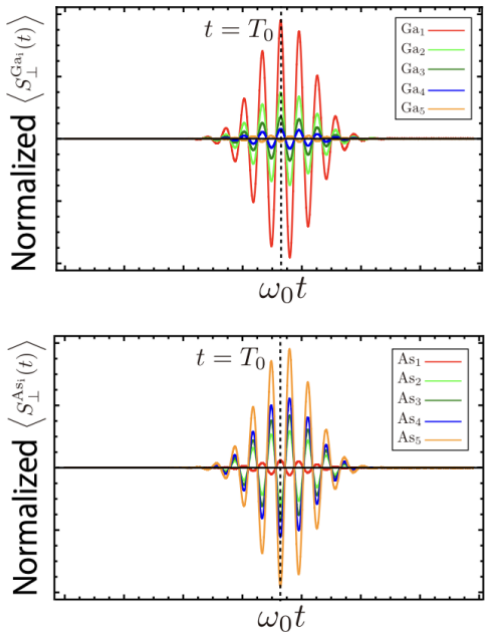

Fig.2: Time evolution of the normalized spin magnetization at each Ga and As atomic site for i=1–5 along the direction with open boundary conditions.

Building upon these results, further analysis reveals that the light-induced spin magnetization directly reflects the material's nonlinear optical response in the spin channel. These findings open the door to novel spintronic functionalities driven by polarized spin magnetization, which we intend to explore in future simulation studies.

References

[1] T. Tamaya and T. Kato, Phys. Rev. B 100, 081203(R) (2019).

[2] N. Yoshikawa, T. Tamaya, and K. Tanaka, Science 356, 736 (2017).

[3] T. Tamaya, A. Ishikawa, T. Ogawa, and K. Tanaka, Phys. Rev. B 94, 241107(R) (2016).

[4]. T. Tamaya, A. Ishikawa, T. Ogawa, and K. Tanaka, Phys. Rev. Lett, 116, 016601 (2016).

Numerical study on low-energy states of quantum spin systems

Hiroki NAKANO
Graduate School of Science, University of Hyogo
Kouto, Kamigori, Hyogo 678-1297, Japan

The many-body problems that researchers encounter in condensed matter physics pose a challenge in accurately estimating physical quantities. The problem of quantum spin systems is a typical one. In the study of a quantum spin system, numerical approaches have been widely and effectively utilized. Valueful information about the target systems has been provided by computational studies.

In the field of quantum spin systems, three methods have been successfully employed. The numerical-diagonalization method is the standard and traditional method. The second method is based on quantum Monte Carlo (QMC) simulation. The density matrix renormalization group (DMRG) method is the third method. Even though there are benefits to each of these methods, they also have drawbacks. QMC simulations are able to handle systems that are significantly bigger, regardless of their spatial dimensions. On the other hand, this approach faces the negative sign problem when we try to accurately evaluate physical quantities in frustrated systems. Regardless of whether or not the target system has frustration, the DMRG method is quite useful when its spatial dimension is one. Regrettably, this method is still being developed for cases where the spatial dimension exceeds one. The numerical diagonalization method can be utilized in various systems regardless of spatial dimension or the presence of frustrations. However, the method can only be used to treat systems that are very small. To overcome this drawback of the numerical diagonalization method, we developed a hybrid-type parallel code for Lanczos diagonalization[1]. By using this code, we can treat various large systems that have not been treated yet. We use this method to analyze various quantum spin systems as our primary approach in this project.

In 2024, this project reported our achievement concerning the spin-S Heisenberg antiferromagnet on the orthogonal dimer lattice [2] in addition to our previous studies of spin-1/2 case[3]. In this study, we successfully carried out Lanczos diagonalizations of this system 16 and 20 sites for $S = 1$ and $S = 3/2$ cases. It is for the first time that within Lanczos-diagonalization studies, numerical results of this model had been presented for $S = 1$ and $S = 3/2$ cases to the best of our knowledge. We clarified the change of the behavior of this model when the ratio of two interaction amplitudes denoted by $r = J_2/J_1$, where J_1 denotes the amplitude of the Heisenberg interaction at the orthgonal dimer and J_2 denotes the amplitude of interaction forming the square lattice. Consequently, we successfully captured the edge of the exact-dimer phase. At the same time, we also detected the edge of the Néel-ordered phase at a different r from the edge of the exact-dimer phase. We confirmed that differences between systems of the 16 and 20 sites are small in our results with respect to the values of r corresponding each of the edges. Our results strongly suggest that the existence of

an intermediate phase between both the edges irrespective of spin-S. Our studies contribute greatly to our deeper understanding of quantum magnetism. Further investigations would shed light on the nontrivial quantum effects in these systems.

References

[1] H. Nakano and A. Terai: J. Phys. Soc. Jpn. **78**, 014003 (2009).

[2] H. Nakano and T. Sakai: J. Phys.: Condens. Matter **36**, 455805 (2024).

[3] H. Nakano and T. Sakai: JPS Conf. Proc. **38**, 011166 (2023).

Universality of Johari-Goldstein relaxation in supercooled liquids and glasses

Takeaki ARAKI[a] and Makina SAITO[b]

[a]*Department of Physics, Kyoto University, Sakyo-ku, Kyoto 606-8502*

[b]*Department of Physics, Tohoku University, Sendai Miyagi 980-8578*

Johari-Goldstein (JG) relaxation, also known as slow β-relaxation, is a relaxation phenomenon observed in supercooled liquids and glasses [1–2]. It plays a crucial role in determining various properties of these materials-particularly their impact strength below the glass transition temperature. Despite its significance, the precise physical mechanism underlying JG relaxation remains unclear, primarily due to the challenges associated with both experimental observation and numerical simulation.

By combining microscopic experiments with molecular dynamics simulations of the ionic glass $CaKNO_3$, we discovered that most particles contribute to the JG process through unexpected, collective non-jumping motions involving angstrom-scale displacements. These subtle movements are activated by the jumping motions of a small fraction of particles [3].

To verify the universality of this physical picture of the JG mode, we conducted molecular dynamics simulations with LAMMPS on metallic glasses ZrCuAl and LaCeNiP, both of which are known to exhibit JG relaxation.

For ZrCuAl, we utilized an embedded atom method (EAM) potential. In contrast, since a suitable EAM potential was not available for LACeNiP, we developed a machine learning potential. We first performed ab initio molecular dynamics simulations on a small atomic system using Quantum ESPRESSO, and subsequently trained a deep learning potential using DeepMD-kit.

Our results revealed that both metallic glasses exhibit fundamentally the same JG relaxation behavior as observed in $CaKNO_3$, supporting the universality of the proposed mechanism.

References

[1] G. P. Johary and M. Goldstein, J. Chem. Phys. **53**, 2327 (1970).

[2] K. L. Ngai, Relaxation and diffusion in complex systems, Springer, Berlin, 2011.

[3] M. Saito, T. Araki, Y. Onodera, K. Ohara, M. Seto, Y. Yoda and Y. Wakabayashi, Acta Materialia **284**, 120536 (2025).

The Physical Origin of the Emerging Ferroelectric Nematic Phase

Matheus DE MELLO and Takeaki ARAKI

Department of Physics,

Kyoto University, Kitashirakawa-oiwake-cho, Sakyo-ku, Kyoto 606-8502

The century-long search for the ferroelectric nematic liquid-crystalline phase reached a major milestone when Nishikawa *et al.* [1] and Mandle *et al.* [2] independently discovered this phase using two distinct rodlike, low-molecular-weight compounds: DIO and RM734, respectively. This novel phase of matter exhibits exceptionally high dielectric permittivity, nonlinear electro-optical properties, and fluidity—making it a promising alternative to conventional ferroelectric solids for advanced technological applications.

This study explores the influence of charge distribution and molecular shape on the stability of ferroelectric nematic liquid crystalline phases through atomistic simulations of 1024-2048 DIO molecules by using GROMACS. We found the role of dipole–dipole interactions and molecular shape in achieving polar ordering by simulating charged and chargeless topologies and analyzing positional and orientational pair-distribution functions. The charged DIO molecules exhibit head-to-tail and side-by-side parallel alignments conducive to long-range polar order, whereas the chargeless molecules show no polar ordering. The 2D x–y cross-section of the correlation pair-distribution function shows that lateral local dipoles in the molecular structure are critical for the formation of the ferroelectric phase.

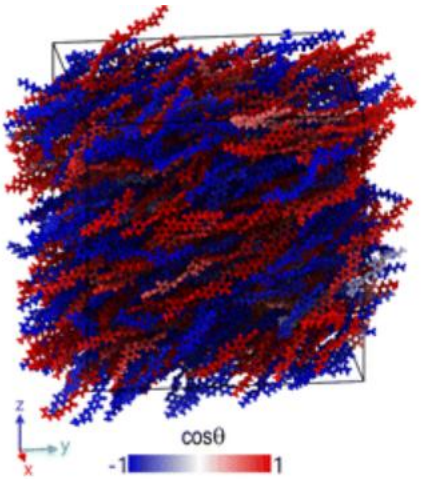

Fig. 1: Configuration snapshot at T = 330 K of the charged DIO.

References

[1] H. Nishikawa, *et al*. Advanced Materials **29**, 1702354 (2017).

[2] R. J. Mandle, *et al.*, Chem. Eur. J. **23**, 14554 (2017).

[3] M. de Mello, M. R. Wilson, and T. Araki, Soft Matter, **21**, 1479 (2025)

Calculating entanglement dynamics in free boson systems by random sampling

Ryui KANEKO
Physics Division, Sophia University
Chiyoda, Tokyo 102-8554, Japan

We analyze the time evolution of entanglement in bosonic systems and explore how quantum information propagates within these systems. This entanglement evolution can be experimentally measured in ultracold atom systems in optical lattices [1, 2]. However, accessible sizes are small in experiments. Comparing experimental results with numerical simulations on classical computers is essential for future experiments to validate the findings. Unfortunately, numerical simulations for the long-time evolution of soft-core boson systems are challenging. Conventional methods, such as exact diagonalization and matrix-product-state methods, can typically compute dynamics for only about 10 sites [3].

Recently, we provided a formal analytical solution for the time evolution of Rényi entanglement during a quench to a noninteracting boson system with a product initial state [4]. Even with this approach, calculations are restricted to around 50 sites at half-filling [4–7], and the computation time grows exponentially with the matrix size n as $\mathcal{O}(n \times 2^n)$. To extend our calculations to larger systems, we employ a random sampling method and investigate how the propagation of quantum information changes with dimensionality.

We specifically focus on the Bose-Hubbard model on a chain and a square lattice and calculate the time evolution of the Rényi entanglement $S_2(t)$ after quenching the system to a noninteracting parameter point $U = 0$, starting from a $010101\cdots$-type charge-ordered state at half-filling. S_2 is given by

$$S_2(t) = -\ln \mathrm{perm} A(t), \tag{1}$$

$$A(t) = \begin{pmatrix} Z(t) & I - Z(t) \\ I - Z(t) & Z(t) \end{pmatrix}, \tag{2}$$

where I is the identity matrix, and $Z(t)$ is a matrix calculated from the time-dependent single-particle correlation functions obtained from the noninteracting Hamiltonian [4]. We evaluate S_2 using the random sampling method up to 100 sites.

According to previous studies [8, 9], the permanent is evaluated as $\mathrm{perm} A = \mathbb{E}\left[\prod_{i=1}^{n} r_i^* \left(\sum_{j=1}^{n} a_{ij} r_j\right)\right]$ using independent and identically distributed random variables r_i with a mean of 0 and a variance of 1. Here, a_{ij} is the (i, j) component of the matrix A. Therefore, the permanent can be calculated by evaluating the expectation value as

$$\mathrm{perm} A \approx \frac{1}{N_{\mathrm{smp}}} \sum_{m=1}^{N_{\mathrm{smp}}} p^{(m)}, \tag{3}$$

$$p^{(m)} = \prod_{i=1}^{n} r_i^{(m)*} \left(\sum_{j=1}^{n} a_{ij} r_j^{(m)}\right), \tag{4}$$

which is the sum of samples for N_{smp} random numbers $\boldsymbol{r}^{(m)}$. Note that, when the entanglement follows the volume-law scaling, the permanent decreases exponentially with the size, and thus the required number of samples increases exponentially with the size. However, when the entanglement satisfies the area-law scaling, the permanent is closed to 1, and thus

the sampling cost is lower than the straightforward computational cost. Although the computational cost of the permanent is still exponential using the random sampling method, it can be reduced to $\mathcal{O}(2^{\alpha n})$ with $\alpha \ll 1$.

We successfully calculate the time evolution of the Rényi entanglement entropy $S_2(t)$ for one-dimensional and two-dimensional systems up to 100 sites by using the number of samples $N_{\rm smp} = 2^{0.2N_{\rm s}+12}$ with $N_{\rm s}$ being the number of sites [10]. The coefficient 0.2 is determined by the scaling of the statistical error of the permanent with the number of samples and the system size. It is found to be universal for both one-dimensional and two-dimensional systems that we studied. After the long-time evolution, the entanglement entropy density approaches a constant value, which is consistent with the volume-law scaling of the entanglement entropy. Remarkably, the entanglement entropy density is independent of the dimensionality and converges to ≈ 0.3 for both one-dimensional and two-dimensional systems. Although performing sufficiently large-scale quantum simulations in experiments is challenging, it is valuable to compare the results of quantum simulations with our numerical results, which can be used to validate the accuracy of the quantum simulations.

References

[1] R. Islam et al., Nature **528**, 77 (2015).

[2] A. M. Kaufman et al., Science **353**, 794 (2016).

[3] S. Goto and I. Danshita, Phys. Rev. B **99**, 054307 (2019).

[4] D. Kagamihara et al., Phys. Rev. A **107**, 033305 (2023).

[5] A. Neville et al., Nat. Phys. **13**, 1153 (2017).

[6] J. Wu et al., Natl. Sci. Rev. **5**, 715 (2018).

[7] P.-H. Lundow and K. Markström, J. Comput. Phys. **455**, 110990 (2022).

[8] D. G. Glynn, Eur. J. Comb., **31**, 1887 (2010).

[9] R. Berkowitz, P. Devlin, Isr. J. Math. **224**, 437 (2018).

[10] R. Kaneko, D. Kagamihara, and I. Danshita, Phys. Rev. A **111**, 032412 (2025).

Dynamic mode decomposition of time-series data in quantum many-body systems

Ryui KANEKO
Physics Division, Sophia University
Chiyoda, Tokyo 102-8554, Japan

Predicting the dynamics of quantum many-body systems over long timescales is a significant challenge. For instance, when using time-dependent variational Monte Carlo methods or tensor network methods to analyze the quench dynamics of isolated quantum many-body systems, calculations often break down within a short time, roughly on the order of the inverse of the energy scale multiplied by Planck's constant $\hbar$ [1–5].

In contrast, instead of trying to determine the wave function at each time step during dynamics calculations, one may predict the long-time dynamics of specific physical quantities by relying solely on accurate short-time time-series data. One such method is dynamic mode decomposition (DMD) [6–9], initially used in fluid dynamics, which has recently proven effective for the dynamics of quantum many-body systems [10–12].

DMD can forecast long-time dynamics up to approximately an order of magnitude longer than the input time-series data [12]. Furthermore, the latest time-dependent variational Monte Carlo methods can compute dynamics for about $100\hbar$ times the inverse of the energy scale [13]. Combining both approaches would make it possible to predict dynamics for durations up to about 1000 times longer than what is achievable with conventional methods applied to quantum many-body systems.

In this study, we have explored the potential of applying DMD to short-term time series data derived from the state-of-the-art time-dependent variational Monte Carlo methods [14] motivated by simulations of superconductivity dynamics under laser irradiation [15]. We trained our model on simulation results of the time evolution of superconducting correlations, utilizing data up to approximately time 200, where we define the time unit as the inverse of the hopping parameter multiplied by $\hbar$. Our predictions successfully extended to time around 400, twice the duration of the input data. We are investigating whether we can achieve high-precision predictions over longer timescales.

References

[1] G. Carleo *et al.* Sci. rep. **2**, 243 (2012).

[2] G. Carleo *et al.* Phys. Rev. A **89**, 031602(R) (2014).

[3] A. Kshetrimayum *et al.*, Nat. Commun. **8**, 1291 (2017).

[4] P. Czarnik *et al.*, Phys. Rev. B **99**, 035115 (2019).

[5] C. Hubig and J. I. Cirac, SciPost Phys. **6**, 31 (2019).

[6] P. J. Schmid and J. Sesterhenn, 61st Annual Meeting of the APS Division of Fluid Dynamics (2008).

[7] C. W. Rowley *et al.*, J. Fluid Mech. **641**, 115 (2009).

[8] P. J. Schmid, J. Fluid Mech. **656**, 5 (2010).

[9] J. H. Tu *et al.*, J. Comput. Dyn. **1**, 391 (2014).

[10] I. A. Luchnikov *et al.*, Phys. Rev. Res. **4**, 043002 (2022).

[11] J. Yin *et al.*, J. Comput. Sci. **64**, 101843 (2022).

[12] R. Kaneko *et al.*, Phys. Rev. Research **7**, 013085 (2025).

[13] K. Ido *et al.*, Phys. Rev. B **97**, 045138 (2018).

[14] T. Misawa *et al.*, Comp. Phys. Commun., **235**, 447 (2019).

[15] K. Ido *et al.*, Sci. Adv. **3(8)**, e1700718 (2017).

Screening in concentrated electrolytes

Takamichi TERAO

Department of Electrical, Electronic and Computer Engineering,

Gifu University, Yanagido 1-1, Gifu, 501-1132

Recently, concentrated electrolyte solutions have attracted considerable attention. In recent studies, surface force measurements have demonstrated that the screening length in concentrated electrolytes becomes considerably large [1], which contradicts the prediction of the Debye–Hückel theory. A theoretical analysis has been performed based on the physical intuition that concentrated electrolytes are analogous to ionic crystals. Because it is difficult to experimentally obtain detailed information on the spatial configurations of ions, molecular dynamics (MD) simulations have been performed as an effective method for clarifying these problems. The results were compared with previously reported experimental studies on the screening length in concentrated electrolytes. To date, the agreement between simulation and experimental results remains under debate.

In this study, MD simulations of aqueous NaCl solutions based on the all-atom model were performed to quantitatively clarify the configuration of monovalent cations and anions in concentrated electrolytes (Fig. 1). Some cations and anions were clustered together by a heteroaggregation process [2]. The results demonstrated that, in concentrated electrolytes, as the electrolyte concentration increased, the fraction of isolated ions diffusing without clustering decreases, whereas the density of isolated ions did not change significantly. Because the total charge of clustered ions approached neutral, these clustered ions may contribute less to the screening effect than isolated ions. These results suggest that, in contrast to dilute electrolytes, the screening length does not change significantly with increasing electrolyte concentration.

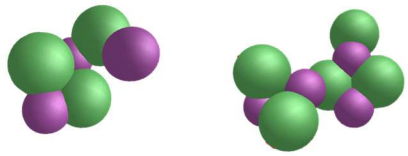

Fig. 1: A snapshot of ions in a system with an electrolyte concentration of 3.8 M. The purple and green spheres represent sodium and chloride ions, respectively.

References

[1] A.M. Smith, A.A. Lee, and S. Perkin, J. Phys. Chem. Lett. **7**, 2157 (2016).

[2] K. Komori and T. Terao. Chem. Phys. Lett. 825, 140627 (2023).

Simulations of polar active fluids under geometrical confinements

Hiroki MATSUKIYO, Jun-ichi FUKUDA

Department of Physics, Kyushu University, Motooka 744, Nishi-ku, Fukuoka 819-0395

We have studied the behavior of polar active fluids under geometrical confinements (The part of the study already mentioned in the previous report has been published in 2024 [1]). The behavior of polar active fluids can be described by a continuum equation, called the Toner-Tu-Swift-Hohenberg (TTSH) equation. In previous studies using the TTSH equation, the nonslip boundary condition was employed. However, the nonslip boundary condition cannot describe the edge current (i.e. edge-localized flow of active fluids observed in several experiments). In ref. [1], we have proposed a new numerical method to calculate the TTSH equation under a slip boundary condition and successfully realized the edge current. Furthermore, we have discovered the temporal oscillation of the edge current direction.

As a further development of this study, we have added a chiral term to the TTSH equation and investigated the behavior of the "chiral TTSH equation" by means of the numerical simulation. The chiral term made the edge current oscillation asymmetric (Fig.1). (We had an oral presentation on this study in the 79th Annual Meeting (2024) of the Physical Society of Japan.)

Throughout the above studies, we have performed simulations for many sets of parameter values, using System B, Ohtaka. The large number of threads of Ohtaka made it possible for us to perform the simulations in parallel for large number of combinations of parameter values, keeping the computing performance.

References

[1] Matsukiyo, H., & Fukuda, J. (2024) Oscillating edge current in polar active fluid. *Physical Review E*, *109*(5), 054604.

(a)

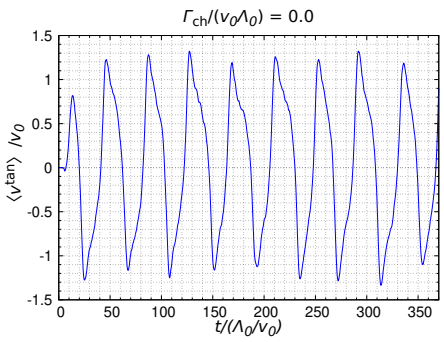

(b)

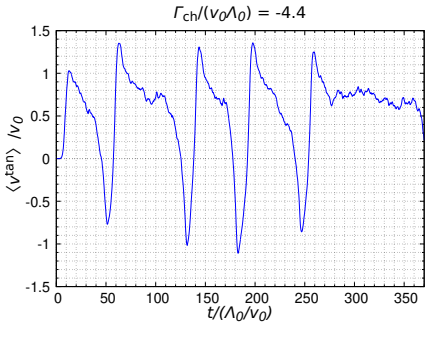

Fig.1. An example of the time evolution of the edge current direction ($\langle v^{\tan}\rangle/v_0$) in the TTSH simulation (a)without and (b)with a chiral term.

Numerical Study of One Dimensional Frustrated Quantum Spin Systems

Kazuo HIDA
Professor Emeritus, Division of Material Science,
Graduate School of Science and Engineering,
Saitama University, Saitama, Saitama 338-8570

1 Model

We investigate the ground-state phases of $(1/2, 1/2, 1)$ mixed diamond chains with single-site anisotropy described by the following Hamiltonian:

$$\mathcal{H} = \sum_{l=1}^{L} \Big[(1+\delta)\boldsymbol{S}_l(\boldsymbol{\tau}_l^{(1)} + \boldsymbol{\tau}_{l-1}^{(1)}) + (1-\delta)\boldsymbol{S}_l(\boldsymbol{\tau}_l^{(2)} + \boldsymbol{\tau}_{l-1}^{(2)}) + \lambda \boldsymbol{\tau}_l^{(1)}\boldsymbol{\tau}_l^{(2)} + D\tau_l^{(2)z2} \Big], \quad (1)$$

where $\boldsymbol{S}_l, \boldsymbol{\tau}_l^{(1)}$ and $\boldsymbol{\tau}_l^{(2)}$ are spin operators with magnitudes $S_l = \tau_l^{(1)} = 1/2$ and $\tau_l^{(2)} = 1$, respectively. The number of unit cells is denoted by L. The lattice structure is depicted in Fig. 1. We consider the region $\lambda \geq 0$ and $1 \geq \delta \geq -1$. The isotropic case ($D = 0$) is investigated in [1].

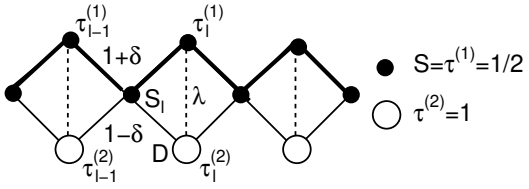

Figure 1: Structure of the diamond chain investigated in this work.

2 Limiting Cases

2.1 $\lambda = 0$

The system is unfrustrated. In the isotropic case $D = 0$, the ground state is the quantized ferrimagnetic (QF) phase with spontaneous magnetization $m_{\rm sp} = 1$ per unit cell according to the Lieb-Mattis (LM) theorem.[1, 2] In the presence of easy-axis anisotropy $D < 0$, this state remains as the QF phase with $m_{\rm sp}^z = 1$. This phase is called the LM1 phase. On the other hand, in the presence of easy-plane anisotropy $D > 0$, the XY component of the magnetization cannot order due to U(1) symmetry. Hence, the ground state turns into the nonmagnetic Tomonaga-Luttinger liquid (TLL) phase.

2.2 $\delta = 1$

If $\lambda > 0$, the system is unfrustrated. The ground state in the isotropic case is the QF phase with $m_{\rm sp} = 1$ according to the LM theorem.[1, 2] For $D < 0$, this state remains as the QF phase with $m_{\rm sp}^z = 1$. We call this phase is the LM2 phase to distingush from the LM1 phase with a different spin configuration. On the other hand, for $D > 0$, the XY component of the magnetization cannot order due to U(1) symmetry. Hence, the ground state turns into the TLL phase.

2.3 $\delta = -1$

The system is unfrustrated and the ground state in the isotropic case is the nonmagnetic phase with $m_{\rm sp} = 0$ according to the LM theorem.[1, 2] This phase is expected to be the TLL phase as discussed in [1]. For $D < 0$, this

parameters	$\mathcal{H}^{\rm eff}$	GS
$\delta > \delta_c, D > 0$	XY-like	TLL
$\delta_c > \delta > 0, D > 0$	Ising-like AF	Néel
$\delta < 0, D > 0$	XY-like	TLL
$\delta > \delta_c, D < 0$	Ising-like F	LM2
$\delta_c > \delta > 0, D < 0$	XY-like	TLL
$\delta < 0, D < 0$	Ising-like AF	Néel

Table 1: Ground-state (GS) phases in the large λ limit. $\delta_c = 0.6(1 + 2D/5\lambda)$. F and AF stand for ferromagnet and antiferromagnet, respectively.

state turns into the Néel phase. On the other hand, for $D > 0$, the ground state remains in the nonmagnetic TLL phase.

2.4 $\lambda \gg 1$

The spins $\boldsymbol{\tau}_l^{(1)}$ and $\boldsymbol{\tau}_l^{(2)}$ are strongly coupled to form a single spin $\boldsymbol{T}_l$ with magnitude 1/2. The effective Hamiltonian for $\boldsymbol{S}_l$ and $\boldsymbol{T}_l$ is a spin-1/2 XXZ Hamiltonian given by

$$\mathcal{H}^{\rm eff} = \sum_{l=1}^{L} \Big\{ J_{\rm eff}^{z} \hat{T}_l^z (S_l^z + S_{l+1}^z) + \frac{1}{2} J_{\rm eff}^{xy} \left[\hat{T}_l^+ (S_l^- + S_{l+1}^-) + \text{h.c.} \right] \Big\} \quad (2)$$

with

$$J_{\rm eff}^{z} \simeq 1 - \frac{5\delta}{3}\left(1 - \frac{32D}{45\lambda}\right) \quad (3)$$

$$J_{\rm eff}^{xy} \simeq 1 - \frac{5\delta}{3}\left(1 - \frac{4D}{45\lambda}\right) \quad (4)$$

within the lowest order in λ^{-1}. Considering that the ferromagnetic ground state of (2) corresponds to the LM2 ferrimagnetic state in (1), the ground states in the large λ limit are classified as tabulated in Table 1.

3 Numerical Results

We have carried out the numerical exact diagonalization (NED) calculation for $L = 6$ to obtain the ground-state phase diagram of Fig. 2 for $D = 1$ and $D = -1$. For $D = 1$, an extremely narrow Néel region is found within the TLL phase. It is not clear whether this phase remains in the thermodynamic limit. For $D = -1$, the Néel phase in the shaded region of Fig. 2(b) shrinks with the system size comparing the present data and those for $L = 4$. The preliminary NED calculations for $L = 8$ also support this tendency. Hence, in the thermodynamic limit, we expect that this region will be replaced by the partial ferrimagnetic (PF) phase with $0 < m_{\rm sp} < 1$ as in the isotropic case.[1]

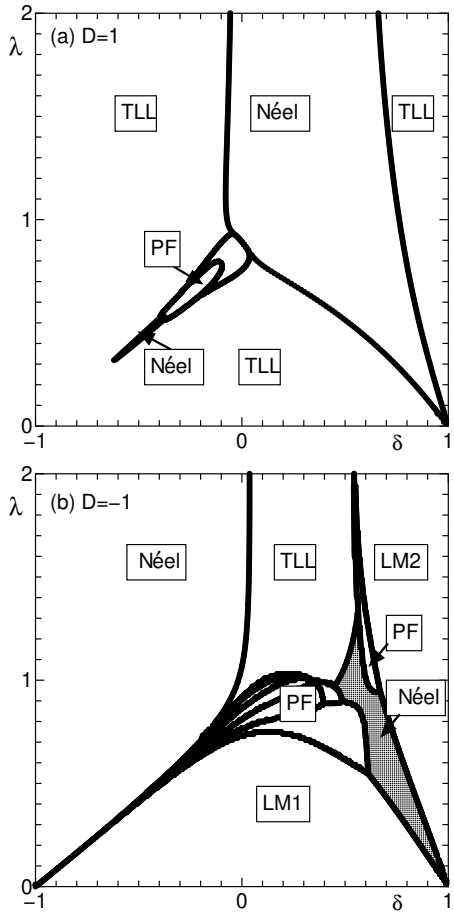

Figure 2: Ground-state phase diagrams based on the NED data with $N = 18$ for (a) $D = 1$ and (b) $D = -1$.

References

[1] K. Hida, J. Phys. Soc. Jpn. **93**, 044703 (2024).

[2] E. Lieb and D. Mattis, J. Math. Phys. **3**, 749 (1962).

Investigation of efficient methods for introducing long-range interactions in the cluster expansion method

Yoshiyuki Fukumoto
Department of Physics and Astronomy, Faculty of Science and Technology, Tokyo University of Science, 2641 Yamazaki, Noda, Chiba 278-8510

In spin-1/2 frustrated systems with magnetic order, the observation of spinon excitations, in addition to magnon excitations, has attracted much interest [1]. The dispersion relation of the magnon excitations provides important information for identifying the spin model, and the linear spin-wave theory (LSWT) is often used for the analysis. However, the application of LSWT is not always justified in frustrated systems because of the smallness of the magnetization. In this case, the series expansion method based on the linked cluster algorithm [2] is useful, and has been successfully applied to the triangular lattice model [3] and the kagome lattice model with Dzyaloshinskii-Moriya interaction [4].

In practical analyses, we often encounter situations where interactions between sites beyond nearest neighbors play some role to determine the shape of magnon dispersion relations. In the LSWT, it is not difficult to introduce such interactions. However, in the series expansion method, the introduction of the such interactions is accompanied by the difficulty of an explosive increase in the number of clusters.

In this study, we performed a series expansion in a stacked triangular lattice system realized in $Ba_3CoSb_2O_9$, where the interlayer interaction is expected to be about 10% of the in-plane interaction [1]. The introduction of three-dimensionality rapidly increases the number of clusters, but to deal with this, we set an order for the clusters and perform the search for them using a binary search algorithm to speed up the process.

When calculating the nth order series exactly, we have to treat all connected clusters with up to n perturbation links. On the other hand, in order to reduce the total number of clusters, it is also possible to restrict the cluster and obtain an approximate series. We previously performed such calculations for a two-dimensional triangular lattice by restricting the total number of sites contained in a cluster to an upper limit of $n+1$ sites. We set $n \leq 8$ and confirmed that we could obtain the same level of accuracy as previous research [3].

In the present study on stacked triangular lattice systems, calculations were first performed using clusters with up to 6 links and 7 sites. As a result, it was found that the excitation energy was negative in part of the wavenumber space. To address this, the number of sites was increased by one and calculations were performed considering clusters with up to 6 links and 8 sites. Then, we found that the problem of negative excitation energy was resolved. Using the latter clusters, calculations were performed for all paths in the experiment and a comparison was made with the experiment. Although some discrepancies were observed in the fine structure, good agreement was obtained for all paths, including the interlayer direction.

[1] S. Ito *et al.*, Nat. Commun. 8, 235, 2017.
[2] M. P. Gelfand *et al.*, JSP 59, 1093, 1990.
[3] W. Zheng *et al.*, PRB 74, 224420, 2006.
[4] S. Kogure *et al.*, JPSJ 92, 113703, 2023.

Analysis for absorption- and fluorescence-spectra of seMpai by quantum chemical calculations, Analysis for *in situ* absorption spectra in firefly bioluminescence by quantum chemical calculations

Miyabi HIYAMA
Gunma University
Tenjin-cho, Kiryu, Gunma 376-8515

Because firefly bioluminescent substrate analogs are attracting attention as next-generation luminescent probes for *in vivo* imaging techniques of animal tissues and cells, the analogs have been developed. seMpai is a soluble chemical species and one of firefly bioluminescent substrate analogs, of which bioluminescence color is red[1].

In this year, the quantum chemical calculations for seMpai were performed to elucidate the absorption and fluorescence property of this compound. Using these calculation results, the experimental absorption and fluorescence spectra of seMpai in aqueous solutions of pH 2-10 were assigned.

The ground-state structures of seMpai and its conjugate acids and bases expected to exist in aqueous solution were obtained using the density functional theory (DFT) method. The excitation energies, oscillator strengths, and free energies of these species were estimated from the time-dependent (TD) DFT calculations.

Using these free energies the relative concentrations in the aqueous solutions at various pH values were obtained. The excitation energies and oscillator intensities of the most abundant chemical species at each pH solutions revealed the assignments of experimental absorption spectrum. The fluorescence energies of these chemical species were determined using TDDFT calculations. The fluorescence pathways of seMpai at each pH solutions were elucidated by the assignments of the experimental spectra.

Quantum chemical calculations of the firefly bioluminescence substrate analog, AkaLumine and its emitter (oxy-AkaLumine) were carried out for the analysis of experimental absorption spectra. The optimized ground state, the oscillator strength and excitation energies at this ground state were obtained for not only the single molecule, but also its dimer using DFT and TDDFT methods. Comparison of the peaks of the experimental absorption spectrum with these excitation energies indicates that there would be the effect of other compounds than those considered in this study.

The computational chemistry software package, Gaussian16, was used for DFT and TDDFT calculations. All calculations were performed on system B of Super Computer Center in ISSP.

References

[1] R. Saito, T. Kuchimaru, S. Higashi, S. W. Lu, M. Kiyama, S. Iwano, R. Obata, T. Hirano, S. Kizaka-Kondoh, and S. A. Maki: Bull. Chem. Soc. Jpn.. **92**, 608 (2019).

Multifractality and topology in monitored quantum dynamics

Yohei FUJI
Department of Applied Physics, University of Tokyo, Tokyo 113-8656

Quantum many-body systems subject to repeated measurements of local observables exhibit measurement-induced phase transitions (MIPTs) [1, 2]. An example of MIPT is the entanglement transition, across which the entanglement entropy of steady states changes from the volume law to area law. Despite its intrinsic nonequilibrium nature, the MIPT bears a close resemblance with equilibrium phase transitions, as it shows critical phenomena with emergent conformal invariance. In this project, we have demonstrated that two other important concepts in equilibrium phase transitions, multifractality and topology, are also revealed in measurement-induced phenomena. To do so, we have used supercomputing facilities (System B) at ISSP, which allow us to perform massive parallel sampling of measurement outcomes required to access measurement-induced phenomena.

First, we considered a single quantum particle evolved under repeated measurements of occupation numbers at random locations [3]. We found that the measurements generally induce multifractality of the single-particle wave function, which is quantified by the scaling properties of moments of the wave-function amplitudes (inverse participation ratios) averaged over measurement outcomes, in analogy with Anderson transitions in disordered systems. Furthermore, we found that a transport property of the particle (diffusive or ballistic) in the absence of measurements qualitatively affects the multifractal properties. It turns out that similar multifractality can also be found

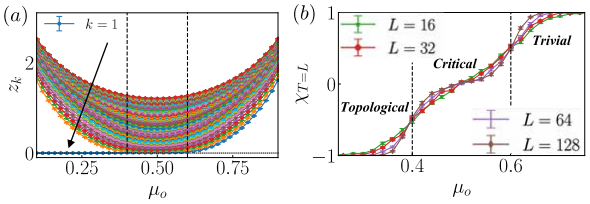

Figure 1: (a) Lyapunov exponents obtained for the monitored Majorana chain of the length $L = 128$ under the open boundary condition. (b) Topological invariant computed at time $T = L$.

for stochastic dynamics of a single classical particle subject to repeated measurements or stochastic resettings, which allows us to obtain some analytical results for measurement-induced multifractality of a diffusive quantum particle.

Second, we considered a monitored version of the famous Kitaev chain [4], a paradigmatic model hosting a topological phase in equilibrium quantum systems. Here, the system is evolved under repeated weak measurements of the fermion parities of neighboring Majorana pairs at every bond. By varying the measurement strengths of even and odd bonds, we can achieve three measurement-induced entanglement phases: topological and trivial area-law entangled phases and a critical phase with subvolume-law entanglement. We showed that the topological area-law phase has a bulk gap and gapless edge spectrum quantified by Lyapunov exponents, as a consequence of Majorana zero modes [see Fig. 1 (a)]. We also constructed a topological invari-

ant to detect the topological area-law phase through the total fermion parity obtained with twisted measurement outcomes at the boundary [see Fig. 1 (b)]. We further showed that a critical phase has gapless bulk Lyapunov spectrum and a vanishing topological invariant at any time $T \leq O(L)$. This study thus establishes the bulk-edge correspondence for measurement-induced topological phases, which certainly goes beyond the equilibrium paradigm.

References

[1] A. C. Potter and R. Vasseur, *Entanglement Dynamics in Hybrid Quantum Circuits*, in Entanglement in Spin Chains: From Theory to Quantum Technology Applications, edited by A. Bayat, S. Bose, and H. Johannesson (Springer International Publishing, Cham, 2022) pp. 211-249.

[2] M. P. A. Fisher, V. Khemani, A. Nahum, and S. Vijay, *Random Quantum Circuits*, Ann. Rev. Condens. Matter Phys. **14**, 335 (2023).

[3] K. Yajima, H. Oshima, K. Mochizuki, and Y. Fuji, *Multifractality in monitored single-particle dynamics*, Phys. Rev. Res. **6**, 043049 (2024).

[4] H. Oshima, K. Mochizuki, R. Hamazaki, and Y. Fuji, *Topology and Spectrum in Measurement-Induced Phase Transitions*, arXiv:2412.11097.

Study on hybrid algorithms for Ising machines

Shu Tanaka

Department of Applied Physics and Physico-Informatics, Keio University

Hiyoshi, Yokohama, Kanagawa, 223-8522

In recent years, Ising machines, which are computers specialized in metaheuristic methods such as quantum annealing, have been actively developed as highly efficient solution methods for combinatorial optimization problems.

In this research project, we have developed a new algorithm that maximizes the hardware performance of Ising machines based on insights from statistical mechanics. This research is expected to provide fundamental technology for the development of existing Ising machine software, as well as contribute to the research and development of new Ising machines based on novel concepts and internal algorithms. Quantum annealing is a promising algorithm for solving combinatorial optimization problems. It searches for the ground state of an Ising model that corresponds to the optimal solution of a given combinatorial optimization problem. The basic principle of quantum annealing is the adiabatic theorem of quantum mechanics. This theorem guarantees that the system remains in the ground state of the Hamiltonian if the time evolution is sufficiently slow. According to the adiabatic theorem, the execution time required for quantum annealing to satisfy adiabaticity is inversely proportional to the square of the minimum energy gap between the ground state and the first excited state during the time evolution. As a result, when the energy gap is small, the search for the ground state becomes extremely difficult, which is a major bottleneck in quantum annealing. Enlarging the energy gap is one strategy to improve the performance of quantum annealing, but its implementation on real hardware remains a difficulty. In this study, we propose a method to efficiently solve instances with small energy gaps by introducing additional local terms into the Hamiltonian and exploiting adiabatic transitions that remain in small energy gaps. The proposed method achieves an approximately quadratic speedup in solution time compared to conventional quantum annealing. Furthermore, we have investigated the transferability of the parameters obtained by the proposed method [1].

References

[1] T. Hattori and S. Tanaka, arXiv:2503.15244 (2025).

Elucidation of critical phenomena by parallelized higher dimensional tensor network RG

Haruki SHIMIZU
Institute for Solid State Physics, University of Tokyo
Kashiwa-no-ha, Kashiwa, Chiba 277-8581

The study of critical systems which lie at the boundary of two distinct phases is crucial in addressing the classification of the phases of matter, which is a central issue of condensed matter physics. By focusing on universality, we can understand the critical behavior of a system, which is characterized by the divergence of correlation length and the emergence of scale invariance.

Conformal field theory (CFT) is a powerful theoretical framework for describing universality, especially for one-dimensional quantum systems and two-dimensional classical systems. It is an important task to identify the underlying CFT of a given critical system. While the central charge plays an important role in CFT, it alone cannot always distinguish between different CFTs. Recent studies of CFT on nonorientable surfaces revealed that the partition function of CFT defined on the Klein bottle contains a universal quantity other than the central charge, so-called Klein bottle entropy, providing an additional tool for discerning different CFTs [1]. Furthermore, the Klein bottle entropy is a universal function of some dimensionless coupling parameter at the region near criticality with its off-critical behavior being useful in extracting the conformal weight of the perturbation operators [2].

Recently, we have proposed a tensor network method for studying critical phenomena on nonorientable surfaces [3]. The key idea involves representing the nonorientable surface topology with the interconnection structure of the tensor network. To be specific, the partition functions on the Klein bottle and real projective plane can be computed by representing the crosscap and rainbow boundaries with renormalized tensors obtained through the higher-order tensor renormalization group (RG) procedure. Our numerical results are consistent with the theoretical predictions.

In this project, we have extended our method to the off-critical regime. Adding thermal and magnetic perturbations to the two-dimensional classical Ising model at criticality, we successfully reproduce the off-critical behavior of the Klein bottle entropy through effectively parallelized calculationss [4]. Our method thus enables efficient computation of the Klein bottle entropy for both critical and off-critical systems, with potential for extension to higher genus surface. Further applications to other models and higher dimensions are in progress.

References

[1] Z.-Q. Li, L.-P. Yang, Z. Y. Xie, H.-H. Tu, H.-J. Liao, and T. Xiang, Phys. Rev. E **101**, 060105(R) (2020).

[2] Y. Zhang, A. Hulsch, H.-C. Zhang, W. Tang, L. Wang and H.-H. Tu, Phys. Rev. Lett. **130**, 151602 (2023).

[3] H. Shimizu and A. Ueda, e-print arXiv:2402.15507 (2024).

[4] H. Shimizu and A. Ueda, in preparation

Numerical Simulation of Anyons in Fractional Quantum Hall Systems

Takeo Kato
Institute for Solid State Physics, University of Tokyo
Kashiwa-no-ha, Kashiwa, Chiba 277-8581

We numerically evaluated the microwave response of edge states in a system composed of a droplet in the fractional quantum Hall state (Laughlin state) coupled to a microwave waveguide. The system considered in this study was theoretically proposed in a previous work [1] as a setup capable of observing the anyonic statistics of excitations in the edge states. Our numerical results are expected to enable detailed comparisons with future experimental results. The effective action of the system was derived by assuming a circular droplet and employing bosonization. The response function to be calculated involves the correlation function of the bosonic field describing the edge states. Since this correlation function cannot be obtained analytically, we performed numerical calculations using the path-integral quantum Monte Carlo method. Large-scale parallel computations were carried out. We numerically evaluated the response functions for two cases: a fractional quantum Hall droplet with Landau level filling factor $\nu = 1/3$, and an integer quantum Hall droplet with $\nu = 1$, for which analytical theoretical construction is possible. In the numerical simulations, we performed 30,000 Monte Carlo steps for thermalization, followed from 1×10^6 to 1.2×10^6 steps for measuring the correlation functions.

The results of our numerical calculations are presented below. Figure 1 shows the temperature dependence of the response function for the case of Landau level filling factor $\nu = 1/3$.

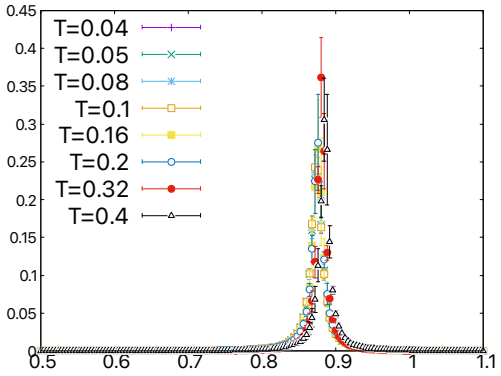

Figure 1: Temperature dependence of the imaginary part of the response function for $\nu = 1/3$ filling.

The results reveal that the peak position shifts and the peak width changes as the temperature varies. This behavior has not been reported in previous studies, including Ref. [1], and thus represents a novel finding. The data shown in Fig. 1 correspond to a quasiparticle tunneling strength of $V = 1.024$. Fig. 3 shows the dependence of the response function on the coupling strength for the integer quantum Hall state with $\nu = 1$. In this case, analytical theoretical calculations are feasible, and the observed peak shift agrees well with the theoretically predicted shift toward lower energies, as shown in the left panel of Fig. 3.

Furthermore, in the case of $\nu = 1$, the peak width shows no significant dependence on the coupling strength and remains nearly constant, as shown in the right panel of Fig. 3. This behavior is consistent with expectations from the theory of chiral Luttinger liquids. Based

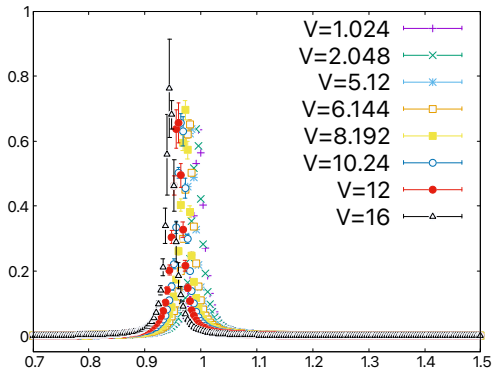

Figure 2: Tunneling-strength dependence of the imaginary part of the response function for $\nu = 1$ filling.

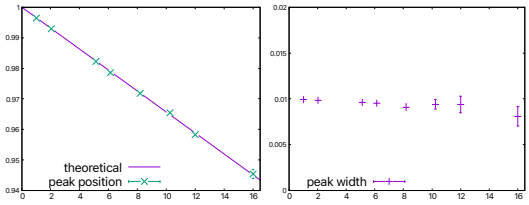

Figure 3: The peak shift (the left panel) and width (the right panel) in the response function for $\nu = 1$ as a function of the quasiparticle tunneling strength.

on these results, we conclude that our numerical calculations successfully reproduce the theoretical predictions for the $\nu = 1$ case.

In the future, we plan to numerically evaluate the microwave response for Laughlin states with filling factors other than $\nu = 1/3$, as well as for droplets with non-circular geometries. At the same time, we aim to improve the numerical accuracy of our simulations and to investigate the detailed temperature dependence of the response functions in Laughlin states.

References

[1] J. Cano, A. Doherty, C. Nayak, D. Reilly. Microwave absorption by a mesoscopic quantum Hall droplet. *Phys. Rev. B*, Vol. 88, p. 165305, 2013.

Tensor learning approaches to computational physics

Hiroshi Shinaoka
Department of Physics, Saitama University, Saitama 338-8570

We have studied quantum impurity problems using physics-informed neural networks (PINNs) [1]. This year, we focused on developing a PINN model that can efficiently predict the self-energy of Anderson impurity models (AIMs) based on the Lehmann representation. The calculations were conducted using the GPU nodes of System C.

The main achievement of this research is the development of a PINN model that combines deep learning techniques with the Lehmann representation and sparse modeling techniques [2]. The model was specifically designed to predict the self-energy of single-orbital AIMs (SAIMs) for noninteracting electron baths with semicircular density of states. As shown in Fig. 1, the key features of our approach include:

- Implementation of physical constraints through the Lehmann representation, which significantly improves the model's accuracy at both high and low Matsubara frequencies
- Use of sparse grids in Matsubara-frequency and real-frequency spaces, reducing the computational cost while maintaining accuracy
- Development of a non-negative projection that ensures the auxiliary spectral function satisfies physical constraints

The PINN model was trained across a wide range of onsite Coulomb interactions U and hybridization strengths V. The results demonstrate high accuracy in both U-V and Matsubara-frequency spaces. For example, the Lehmann representation allows the PINN model to reduce the maximum test error in electron filling by a factor of approximately 7.8.

The calculations were performed using the GPU nodes of System C, which provided the necessary computational resources for training the neural network models.

This research opens up new possibilities for efficient quantum impurity calculations, which are essential for studying strongly correlated electron systems through dynamical mean-field theory (DMFT). The developed PINN model could potentially be extended to more complex systems and integrated into self-consistent DMFT calculations.

References

[1] F. Kakizawa, S. Terasaki, and H. Shinaoka: arXiv:2411.18835 (2023).

[2] J. Li, M. Wallerberger, N. Chikano, C.-N. Yeh, E. Gull, and H. Shinaoka: Phys. Rev. B **101**, 035144 (2020).

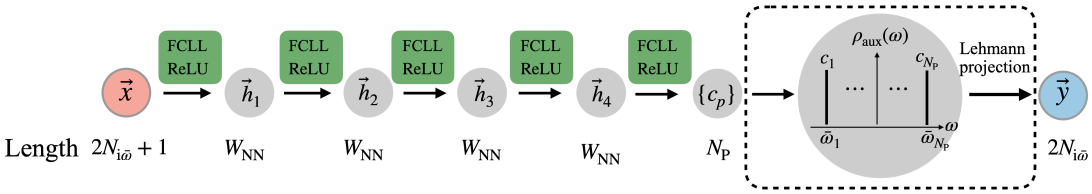

Figure 1: Schematic of the PINN model for predicting the self-energy of Anderson impurity models. The model combines deep learning techniques with the Lehmann representation and sparse modeling techniques to ensure physical constraints are satisfied.

Analysis of Ising model in statistical-mechanical informatics

Yuya SEKI

Graduate School of Science and Technology, Keio University, Kanagawa 223-8522

We have studied properties and performance of factorization machine with annealing (FMA) [1], which is a combinatorial optimization method using simulated annealing (SA) or quantum annealing (QA) combined with factorization machine (FM), a machine learning model whose model equation is in the quadratic form. FMA is a promising approach for combinatorial black-box optimization problems including integer-variable optimization problems [2]. To formulate a Hamiltonian for black-box optimization problems, which is not given analytically, FM is used to estimate interaction coefficients between variables. Then SA or QA is applied to find a low-energy state of the estimated Hamiltonian. Since the Hamiltonian estimated by FM is equivalent to an Ising model, we can apply methods that are developed in the field of condensed matter physics to analyze the properties and the performance of FMA. This year, we have conducted a study to improve the performance of FMA, and that to analyze the performance of FMA for an application to explore a stable structure of crystals.

First, we focused on another surrogate model derived from FM, where interactions between variables are sparsely constrained. Sparse interaction is a common property of actual annealing machines such as D-Wave annealers. In addition, the sparse interaction allows SA to update spin variables with less computation time. Hence, developing the FMA method for a surrogate model with sparsely restricted interactions has the potential to improve the optimization performance. Although this study is still ongoing, we have obtained valuable data, e.g., performance of FMQA for given structures of interactions between spin variables, via parallel computing on the supercomputer.

Second, we studied the performance of FMA for predicting grand canonical crystal structures [3]. In this study, we investigated a wide range of configurations to explore the most stable crystal structure with FMA. By using the supercomputer, we have identified the appropriate configuration.

References

[1] K. Kitai *et al.*: Phys. Rev. Research **2** (2020) 013319.

[2] Y. Seki *et al.*: arXiv:2209.01016 (2022).

[3] Y. Couzinié *et al.*: J. Phys. Soc. Jpn. **94** (2025) 044802.

Scaling law of the partition function ratio

Satoshi MORITA
Graduate School of Science and Technology, Keio University
Yokohama, Kanagawa 223-8522

Tensor network (TN) methods are attracting much attention as powerful tools in various fields including quantum many-body physics, quantum computation, and machine learning. In the classical statistical physics, the state sum in the partition function can be represented in the form of TN. However, the contraction of a large TN still requires an exponentially large computational effort. The tensor renormalization group (TRG) method and its variants calculate a coarse-grained tensor by information compression using the singular value decomposition [1]. Adachi, Okubo and Todo have proposed the bond-weighted TRG (BWTRG) method, which improves the accuracy of TRG by introducing a bond weight and distributing it appropriately [2]. We have proposed the finite-size scaling analysis using TRG results [3]. Our recent study showed that the critical temperature and critical exponent are improved from the previous method by calculating the magnetization using BWTRG [4].

In this study, we consider the ratio of partition functions proposed by Gu and Wen [5], This ratio extracts the structure of the fixed-point tensor in the thermodynamic limit and detects the phase transition. This ratio is a dimensionless quantity and its jump indicates the phase transition, which is similar to the Binder parameter frequently used in Monte Carlo methods. We predict that the finite-size scaling of this ratio is similar to the Binder parameter,

$$X_1 \equiv \frac{Z(L,L)^2}{Z(2L,L)} \sim f(L^{1/\nu}\, t).$$

We demonstrate that this scaling actually holds in a wide size range from $L = 2^10$ to 2^20 by high-precision partition function calculations using BWTRG. We investigate the bond dimension dependence of the critical exponent and critical temperature, and show that it converges to the exact value faster than the method using TRG or matrix product states. Furthermore, we derive that the universal value of X_1 at criticality by the discussion of conformal field theory

$$X_1 = \frac{\left(\sum_\alpha e^{-2\pi x_\alpha}\right)^2}{\sum_\alpha e^{-4\pi x_\alpha}},$$

where x_α is the scaling dimension of the scaling operator ϕ_α, and show that our numerical results are accurately consistent with this [4]. It is known that the partition function can be calculated directly by TRG, and its accuracy is higher than that of the magnetization. We believe that this new scaling law will play an important role in the study of phase transitions using tensor network methods.

References

[1] M. Levin and C. P. Nave, Phys. Rev. Lett. **99**, 120601 (2007).

[2] D. Adachi, T. Okubo, and S. Todo, Phys. Rev. B **105**, L060402 (2022).

[3] S. Morita and N. Kawashima, Comput. Phys. Commun. **236**, 65 (2019).

[4] S. Morita and N. Kawashima, Phys. Rev. B **111**, 054433 (2025).

[5] Z. C. Gu and X. G. W, Phys. Rev. B **80**, 155131 (2009).

A molecular dynamics simulation study for immiscible polymer blends

Takeshi SATO
Advanced Manufacturing Technology Institute, Kanazawa University
Kanazawa, Ishikawa 920-1192

Polymer blends, which are commonly used in polymeric products, are known to exhibit phase-separated structures under specific temperatures and compositional conditions. Thus, from both fundamental and engineering viewpoints, it is critical to understand the phase-separation dynamics and the mechanical properties exhibited by the resulting phase-separated structures. Although these two aspects are closely related to the dynamics of the individual component chains, the detailed mechanisms underlying these relationships have not yet been fully elucidated. This problem occurs because it is difficult to evaluate the dynamics of component chains in detail experimentally. Thus, this project conducted a numerical investigation with a coarse-grained molecular dynamics (CGMD) model. CGMD simulations provide microscopic insights into the dynamics of (CG) polymer chains in blends by directly tracking the motion of chains.

This study employed the Kremer-Grest CGMD model, [1] in which CG beads bonded by finitely extensible nonlinear elastic (FENE) springs represent a polymer chain. A Lennard-Jones (LJ) potential was applied between all bead pairs within a certain cutoff distance. We also incorporated an angle potential to introduce a contrast in the glass transition temperatures of polymers. This study addressed several binary blends of unentangled polymers with different glass transition temperatures. We generated a microscopically phase-separated (PS) structure by varying the LJ interaction strength between beads of the same polymer species. [2] We reset the interaction strength to the standard value after forming the PS structure for simplicity. We also prepared polymer blend systems in a uniformly mixed (UM) state without altering the interaction strength. The systems were thermally equilibrated at a temperature between the glass transition temperatures of the two polymers. We then investigated their shear rheological properties. All CGMD simulations were conducted with LAMMPS.

We computed transient shear viscosity η^+ and the first normal stress coefficient Ψ_1^+ of the prepared blends for several different shear rates. PS and UM blends exhibited a distinct overshoot in η^+ before reaching a steady state. We found that the UM system exhibited larger values of η^+ and Ψ_1^+ compared to the PS system with the same composition as the UM system. Moreover, the shear rheological properties of the PS system corresponded closely to the weighted sum of those of the individual components that consist of the blend at the same temperature. These findings serve as an essential stepping stone for numerically investigating the rheology of blends with PS structures.

References

[1] K. Kremer and G. S. Grest: J. Chem. Phys. **92**, 5057 (1990).

[2] W. Peng, R. Ranganathan, P. Keblinski, and R. Ozisik: Macromolecules **50**, 6293 (2017).

A study of the dynamics of thermal equilibrium and nonequilibrium FFLO states using the nonequilibrium Green's function technique

Taira KAWAMURA
Department of Physics, College of Science and Technology, Nihon University
Tokyo 101-8308, Japan

Among various pairing mechanisms beyond the BCS theory, the Fulde-Ferrell-Larkin-Ovchinnikov (FFLO) state is notable for its unique feature of Cooper pairs with nonzero center-of-mass momentum. It can be realized under an external magnetic field, where Zeeman splitting of the energy bands leads to a thermal-equilibrium FFLO state. Recent studies have also proposed a nonequilibrium counterpart, driven by nonequilibrium quasiparticle distributions [1].

In this project, we studied the dynamics of a superconductor driven out of equilibrium by quasiparticle injection from normal-metal electrodes under an external magnetic field, focusing on the interplay between the equilibrium and nonequilibrium FFLO states [2]. To describe this, we derived a time-evolution equation using the nonequilibrium Green's function technique.

The resulting integro-differential equation includes memory terms, making direct real-space simulations challenging. To overcome this computational difficulty, we developed a method to transform it into a set of coupled ordinary differential equations. We then implemented a parallelized solver using OpenMP on the ISSP supercomputing system, enabling us to track the long-time real-space dynamics following a voltage quench.

From these simulations, we obtained the phase diagram shown in Fig. 1. Notably, we identified a novel reentrant mechanism: while moderate quasiparticle injection destroys the thermal-equilibrium FFLO state, stronger injection gives rise to the nonequilibrium FFLO state. These results highlight the potential for controlling quantum states via coordinated manipulation of band structures and distribution functions.

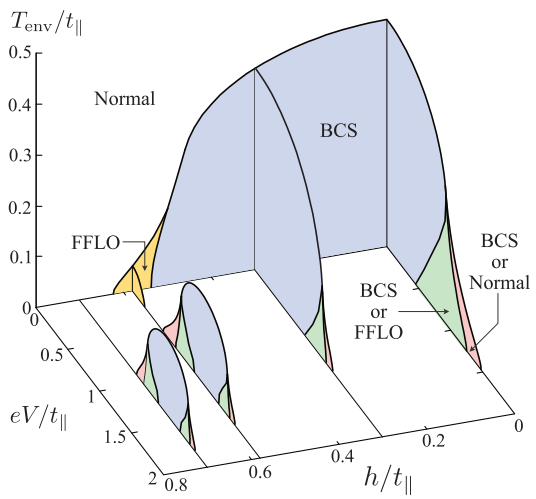

Figure 1: Phase diagram of a superconductor under an external magnetic field h and a bias voltage V [2].

References

[1] T. Kawamura, Y. Ohashi, and H.T.C. Stoof, Phys. Rev. **109**, 104502 (2024).

[2] T. Kawamura and Y. Ohashi, arXiv:2503.04179.

Athermal Simple Shear of Colloidal Gels

Vishnu V. KRISHNAN
RCAST, University of Tokyo
4–6–1 Komaba, Meguro-ku, Tokyo 153–8904

Through our work we aimed to study the mechanical response of colloidal gels to repetitive mechanical deformations. We performed athermal quasistatic shear (AQS) simulations of models of phase-separating colloidal systems in order to probe the evolution of the solid network of the gel. Such a setting models highly overdamped systems at intermediate shear rates where the particles relax to their minima faster than the deformation changes them.

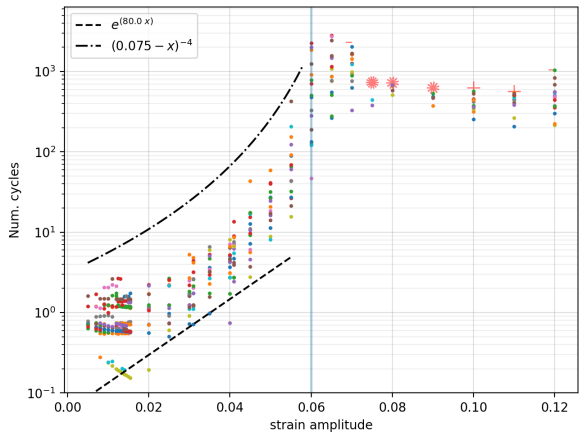

Figure 1: Number of cycles required to achieve steady-state absorption into limit cycles, under *symmetric* AQS. Each color indicates one of 16 distinct samples.

In order to gain a complete understanding of the properties of disordered materials such as gels, one must first comprehend the underlying energy landscape which mediates and dictates both the stable structures and the modes of transformation between them. A crucial feature of amorphous model systems is the existence of limit cycles in this landscape, under AQS deformations. These have been previously utilized, in glasses, to study mechanical properties like yielding. We have made use of similar techniques to better understand corresponding mechanisms in networked materials.

In Figs. 1 & 2 we show the number of strain cycles required by each sample to reach an absorbing state, elucidating the complexity of the energy landscape at each strain amplitude. While the simulations are still on-going, we perceive a maximum in the plots, signifying the existence of a yielding transition in gels. Of even more importance is the existence of absorbing states *after* yield, suggesting the significant role of networks in self-healing.

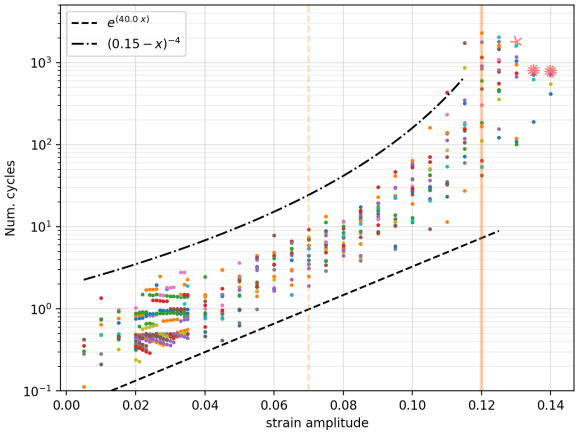

Figure 2: Number of cycles required to achieve steady-state absorption into limit cycles, under *asymmetric* AQS. The spokes in red indicate the number of samples that are yet to be absorbed.

The ISSP infrastructure allowed us to perform extended parallelized simulations using the LAMMPS software.

Performance of uncertainty-based active learning in materials science

Ryo TAMURA
International Center for Materials Nanoarchitectonics,
National Institute for Materials Science,
1-1 Namiki, Tsukuba, Ibaraki, 305-0044

In materials science, materials are synthesized based on information necessary for materials development, such as composition, structure, and processing conditions, and their properties are subsequently measured. This process can be regarded as a function that maps material information as input to material properties as output. This function is called a black-box function because it cannot be described analytically. To optimize a black-box function, black-box optimization methods are developed[1], and most famous one is Bayesian optimization[2]. But, here, we focus on the prediction performance of a black-box function. This is because that obtaining a precise approximation of a black-box function is crucial for understanding and evaluating innovative materials.

Active learning aims to improve such approximations with a limited amount of training data. In this study, we investigate whether uncertainty sampling-based active learning can enable efficient approximation of black-box functions in regression tasks using various materials databases[3]. As materials database, first, we focus on ternary liquidus surfaces where the input space is uniformly distributed and defined in a relatively low-dimensional space. The results demonstrate that uncertainty-based active learning can yield superior black-box functions with higher prediction accuracy compared to random sampling. Furthermore, in cases where the inputs are discretely distributed and imbalanced in a high-dimensional feature space, datasets extracted from inorganic materials, small molecules, and polymer databases are considered. It is shown that uncertainty-based active learning can sometimes be inefficient. Based on the dependence on material descriptors, when the descriptor dimensionality is small, active learning tends to produce better black-box functions than random sampling. The results indicate that active learning is occasionally inefficient in obtaining a better black-box function in materials science.

References

[1] K. Terayama, M. Sumita, R. Tamura, and K. Tsuda, Acc. Chem. Res. **54**, 1334-1346 (2021).

[2] Y. Motoyama, R. Tamura, K. Yoshimi, K. Terayama, T. Ueno, and K. Tsuda, Comput. Phys. Commun. **278**, 108405 (2022).

[3] A. Koizumi, G. Deffrennes, K. Terayama, and R. Tamura, Sci. Rep. **14**, 27019 (2024).

Mechanism of Size Segregation in Granular Media under Vibration: Analysis Based on Effective Interparticle Forces

Fumiaki NAKAI
Department of Earth and Space Science, Osaka University
1-1 Machikaneyama, Toyonaka 560-0043, Japan

When a bidisperse granular mixture is vibrated, particles segregate by size, with particles of similar diameter clustering together—a phenomenon known as size segregation. Several mechanisms have been proposed to account for this behaviour—including convection-driven circulation, void-filling (sinking), depletion-like entropic forces, and segregation caused by gradients in granular temperature (kinetic energy)—yet a comprehensive physical picture has not been established [1]. In this study, we investigated how the steady-state patterns that emerge in a quasi-two-dimensional vibrated bed depend on four key parameters: the partial packing fractions of large and small particles, the size ratio, the acceleration (Γ), and the horizontal system size. The principal results have been published in Granular Matter [2]. We also performed rheological behaviors of a structured granular media [3].

Discrete-element-method (DEM) simulations were carried out with the granular package of LAMMPS. Preliminary test runs were executed on the "i8cpu" partition of the System B supercomputer (Ohtaka) to validate input parameters and estimate computational cost. Production simulations were subsequently carried out on the "F1cpu" partition, using a single compute node with 128 MPI ranks to execute separate runs for each of the 210 distinct parameter sets.

In this study, we investigated a bidisperse granular mixture consisting of 3 mm and 1 mm spheres with a size dispersion of 20 %. The particles were confined between two parallel plates to create a quasi-two-dimensional cell. Structures that developed under vertical vibration were quantified by the radial-distribution

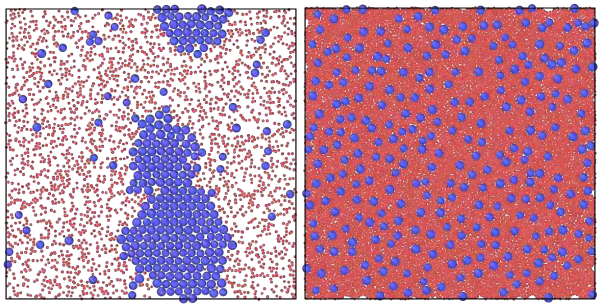

Figure 1: Snapshots of bidisperse granular mixtures in which the packing fraction of large particles (blue) is constant while that of small particles (red) is varied. When the small-particle fraction is dilute (left), the large particles segregate strongly; in contrast, segregation disappears once the small-particle fraction becomes dense (right). This newly observed suppression of segregation is robust across a wide range of size ratios, vibration accelerations, and system dimensions. All segregation simulations were executed on the System B supercomputer (Ohtaka); full details are given in Ref. [2], and related simulations on dislocation-mediated rheology are reported in Ref. [3].

function, the static structure factor, and the hexagonal order parameter over a range of packing fractions. We found that increasing the packing fraction of small particles (ϕ_s) suppresses the segregation of large particles, as illustrated in Fig. 1. This suppression remains robust when the particle-size ratio, system dimensions, or vibration acceleration are varied. The radial-distribution analysis further shows that the effective interaction between large particles depends systematically on ϕ_s: at low ϕ_s an attractive component—reported previously—emerges, whereas at high ϕ_s the interaction becomes predominantly repulsive. The present results have been published in Ref. [2]; a detailed study of the underlying physical mechanism is now in progress.

References

[1] A. D. Rosato and C. Windows-Yule *Segregation in vibrated granular systems*, Academic Press (2020)

[2] F. Nakai and K. Yishii: Granul. Matter **27**, 7 (2025).

[3] F. Nakai, T. Uneyama, Y. Sasaki, K. Yoshii, and H. Katsuragi: arXiv:2410.20308, (2025).

A Large-Scale Molecular Dynamics Simulation Study on the Melt Growth Mechanism of High-Pressure Ice III

Hiroki NADA

Faculty of Engineering, Tottori University, 4-101 Koyama-Minami, Tottori 680-8552

Ice III is one of ice crystal phases that form at high pressure and low temperature conditions. A recent experimental study reported that unknown water, which was different from bulk water, was formed at the interface of ice III during its growth [1]. Thus, in this project, a molecular dynamics (MD) simulation was conducted to elucidate the growth mechanism of ice III from water.

The simulation was performed at 230 K and 315 MPa for a system in which a (100) plane of ice III was in contact with a water phase (Fig. 1). The interaction between pairs of water molecules was calculated using the TIP4P/Ice model. Following a previous study [2], the simulation was carried out with DL_POLY 2.20 using System C of ISSP Supercomputer Center.

The results of the present MD simulation for ice III, which were compared with published results for hexagonal ice (I_h) [3], were summarized as follows. The growth rate was larger for ice III than for I_h. The growth of ice III occurred by a collected molecule process, like in the case for the growth of I_h. The interface for ice III had a diffuse structure, like the interface for I_h. However, the width of the interface was smaller for ice III than for I_h.

Notably, the difference in the density between ice and water was smaller for ice III than for I_h. We speculated that this density difference is correlated with the difference in the growth rate between ice III and I_h. To confirm it, the MD simulation for the growth of ice III was also performed at 400, 500, and 700 MPa. At 400 MPa, the density difference between ice III and water became the smallest, and the growth rate became the largest.

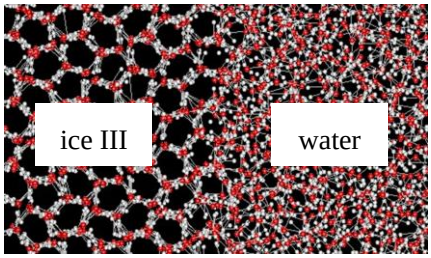

Fig. 1: Snapshots of water molecules near the interface in the simulation system.

References

[1] H. Niinomi, T. Yamazaki, H. Nada, T. Hama, A. Kouchi, T. Oshkiri, M. Nakagawa, and Y. Kimura, J. Phys. Chem. Lett. **15**, 659 (2024).

[2] H. Nada, J. Chem. Phys. **38**, 136 (2022).

[3] P. Montero de Hijes, J. R. Espinosa, C. Vega, and E. Sanz., J. Chem. Phys. **151**, 044509 (2019).

Two variants of discrete-time quantum walk

Manami YAMAGISHI
Department of Physics, The University of Tokyo
Kashiwa-no-ha, Kashiwa, Chiba 277-8581

Naomichi HATANO
Institute of Industrial Science, The University of Tokyo
Kashiwa-no-ha, Kashiwa, Chiba 277-8581

We have considered two non-trivial variants of discrete-time quantum walk. First, we proposed a minimal model of a quantum active particle [1] as a building block of a quantum version of active matter. Active matter is a component that takes up energy from the environment, stores it inside, converts the internal energy into kinetic energy, and thereby moves, or a collection of such components. The introduction of the idea of classical active matter enabled us to unify a variety of studies outside conventional classes of dynamics, dynamics without energy or momentum conservation, that had been investigated separately before and to understand their commonalities and universalities. Some researchers very recently tried to introduce the concept of active matter into quantum systems. Starting with a paper by Adachi *et al.* [2], the research field of quantum active matter is expanding [1, 3, 4, 5, 6, 7].

We proposed a quantum active particle using non-unitary quantum walks in one and two spatial dimensions (1D and 2D). We have observed similarities to a classical active Brownian particle [8] and distinct quantum features at the same time. As a similarity, we observed that dynamics of our quantum active walker becomes more active in a non-trivial way when a non-Hermiticity parameter g, which corresponds to the energy take-up in classical active Brownian particles, becomes larger. As quantum features, we observed ballistic propagation of peaks (1D), particle staying on the constant energy surface (2D) and resonant transition between two energy levels (1D and 2D).

Second, in the hope of eventually proposing quantum active matter in which quantum active walkers interact with each other, we are trying to introduce the Kondo-type interaction [9] between two quantum walkers. We first formulate the standard quantum walk as a massless Dirac particle propagating through a continuum time-space with a series of periodically located delta potentials. This new formulation lets us define the Kondo-type interaction in the following way. We update a delta potential at the origin to one with the inner degree of freedom of a spin. We then introduce a Heisenberg-type interaction between the magnetic impurity spin and the inner degree of freedom of a quantum walker, namely the left-moving and right-moving components.

When we have more than one quantum walker, each quantum walker interacts with the rest through the magnetic impurity spin; which is the Kondo physics. A unique feature of our model is that the inner degree of freedom of the quantum walker is strongly coupled to the spatial movement of the walker, because the left-moving component is shifted to the left in the next time step and the right-moving component to the right. In other words, there is a strong spin-orbit coupling in each quantum walker. This makes the dynamics due to the

Kondo-type interaction quite distinctive from the dynamics of the standard Kondo model.

We have found an exact solution of the bound state of one walker to the magnetic impurity. We then simulated an impact of a second walker colliding to the first walker bounded to the impurity. We discovered that the first walker keeps bounded to the impurity even after the collision of the second walker, which reminds us of the Kondo screening.

We utilized the Supercomputer at ISSP to numerically diagonalize our time-evolution operator, whose maximum size was $(70 \times 70 \times 8)^2$ in two dimensions as well as the case of two interacting quantum walkers. By allocating arrays dynamically, we allowed our system to reach the spatial size of 70×70 (one in the x direction and the other in the y direction).

References

[1] M. Yamagishi, N. Hatano, and H. Obuse: Proposal of a quantum version of active particles via a nonunitary quantum walk, Sci. Rep. **14**, 28648 (2024).

[2] K. Adachi, K. Takasan, and K. Kawaguchi: Phys. Rev. Res. **4**, 013194 (2022).

[3] Y. Zheng, A.P. Antonov, B. Liebchen, and H. Löwen: arXiv:2305.16131 (2023).

[4] R. Khasseh, S. Wald, R. Moessner, C.A. Weber, and M. Heyl: arXiv:2308.01603 (2023).

[5] K. Takasan, K. Adachi, and K. Kawaguchi: Phys. Rev. Research **6**, 023096 (2024).

[6] T. Nadolny, C. Bruder, and M. Brunelli: Phys. Rev. X **15**, 011010 (2025).

[7] A.-G. Penner, L. Viotti, R. Fazio, L. Arrachea, and F. con Oppen: arXiv:2503.07751 (2025).

[8] F. Schweitzer, W. Ebeling, and B. Tilch: Phys. Rev. Lett. **80**, 5044 (1998).

[9] J. Kondo: Prog. Theor. Phys., **32**, 37 (1964).

Deep learning glassy dynamics by graph neural networks

Hayato SHIBA
Department of Information Science, University of Hyogo
Minatojima-Minatomachi, Chuo-ku, Kobe, Hyogo 650-0027

Over the past two decades, the relationship between structure and dynamics in glass-forming liquids has been a subject of intensive discussion. As atomic motion slows down drastically near the glass transition, localized domains of particles that are more likely to undergo rearrangement begin to grow. Recently, machine learning (ML) methodologies have enabled the prediction of where such domains are likely to emerge based on the initial particle configurations. A number of ML models have been proposed for this task, achieving significant improvements in prediction accuracy over the years. The most recent models show comparable performance, though they differ in the details of their predictions. These developments are reviewed in a recent review [1], where the models are compared largely based on a common datasets including that created by our group.

In FY2024, we developed a graph neural network (GNN) model tailored for predicting the dynamics of athermal glasses under quasi-static shear deformation. For training, we used our own simulation dataset of a 3D Kob-Andersen Lennard-Jones mixture, prepared in FY2022. Since external shear breaks the system's rotational symmetry, the resulting deformation evolves anisotropically. To accommodate this, we modified our existing GNN model, BOTAN [2], so that it outputs three-dimensional displacement vectors rather than scalar displacement magnitudes. Inhereting the merit of BOTAN of having another output, changes in inter-particle distances, the model succeded in partially capturing collective motions of particles. We are continuing our efforts to improve the model's prediction accuracy and its consistency with physical aspects highlighted in the direct simluations (training data).

References

[1] G. Jung, R. M. Alkemade, V. Bapst, D. Coslovich, L. Filion, F. P. Landes, A. J. Liu, F. S. Pezzicoli, H. Shiba, G. Volpe, F. Zamponi, L. Berthier, and G. Biroli: Nat. Rev. Phys. **7**, 91-104 (2025).

[2] H. Shiba, M. Hanai, T. Suzumura, and T. Shimokawabe: J. Chem. Phys: **158**, 084503 (2023).

Local structure analysis and non-equilibrium phase transition in self-propelled hard polygon systems

Masaharu ISOBE
Nagoya Institute of Technology
Gokiso-cho, Showa-ku, Nagoya, 466-8555

Hard disk/sphere systems, representing the most fundamental models in statistical mechanics, have been extensively investigated through molecular simulations for both equilibrium and non-equilibrium phenomena [1]. In this project, we investigate the equilibration processes and non-equilibrium phase transitions in self-propelled hard polygon model systems utilizing state-of-the-art computational techniques, specifically Event-Chain Monte Carlo (ECMC)[2, 3], Newtonian Event-Chain Monte Carlo (NECMC)[4], and Event-Driven Molecular Dynamics (EDMD) [5].

Simple and efficient methods for local structural analysis in polydisperse hard disk systems [6]

In nonequilibrium statistical physics, quantifying nearest (and higher-order) neighbors and free volumes of particles is crucial for understanding macroscopic collective phenomena in many-body systems. Conventional techniques using fixed-distance cutoffs or Voronoi constructions have significant limitations, particularly when applied to nonequilibrium, inhomogeneous, and polydisperse systems. These limitations have hindered comprehensive analysis of complex phenomena such as glass/granular jamming transitions and active matter behavior. In this study, we implement several efficient approaches for local structure analysis in nonequilibrium, inhomogeneous, and polydisperse hard disk systems. Through systematic evaluation, we identified limitations in conventional analytical methods when applied to these complex configurations, and confirmed that our "2D SANNex" algorithm effectively overcomes these traditional constraints. Furthermore, we established rigorous mathematical formulations for evaluating higher-order neighbors. We also implemented the neighbors for enclosing local free area ("NELF-A") methodology, which enables precise quantification of local free areas and local pressure in densely packed polydisperse systems. These methodologies provide substantial analytical tools for examining essential local structural information in many-body systems, thereby elucidating slow relaxation dynamics and enabling precise identification and characterization of hopping motion between metastable states in highly packed systems.

Microscopic mechanisms of diffusion dynamics : a comparative efficiency study of event-chain Monte Carlo variants in dense hard disk systems [7]

In molecular simulations, efficient methods for investigating equilibration and relaxation processes in high-density systems are critically important yet challenging. This study examines the diffusional characteristics of monodisperse hard disk systems at equilibrium, comparing novel methodologies of event-chain Monte Carlo methods [3], specifically the Newtonian event-chain [4] and straight event-chain algorithms [2]. We systematically analyze both event-based and CPU time-based efficiency in liquid and solid phases, aiming to elucidate the microscopic mechanisms un-

derlying structural relaxation. Our results demonstrate that NEC frequently exhibits superior efficiency in terms of diffusion coefficient per event and CPU time among ECMC variants, while SEC-xy shows better CPU-time efficiency in certain chain length regimes due to its simplified implementation. The diffusion coefficients display a three-stage behavior with respect to chain length or duration, attributed to increased collision events relative to simple accepted displacements (as in MCMC) and reducible sampling due to finite system size effects. Notably, NEC's diffusion coefficient remains independent of chain duration time in the infinite limit and increases logarithmically with system size, suggesting potential divergence in the thermodynamic limit. These findings provide valuable insights into the optimization of slow equilibrium dynamics in high-density and large-scale systems, particularly for reducing practical computational costs in molecular simulations.

Recursive algorithm to the centroid of free area for inherent structure and hopping motion in deeply supercooled binary hard disk systems [8]

Inherent structures, obtained by removing thermal fluctuations from complex trajectories, reveal fundamental mechanisms of structural relaxation in dense glassy systems. For hard disk/sphere systems, determining these structures is challenging due to discontinuous inter-particle potentials and flat energy landscapes. We introduce the Recursive Centroid of Free Area algorithm (ReCFA), inspired by steepest descent methods, to compute inherent structures in hard disk systems. Our comparative analyses between ReCFA and conventional techniques focused on string-like hopping motions in supercompressed binary hard disks. ReCFA effectively captures entropic contributions and produces physically reasonable particle displacements that identify hopping motions between metastable basins in jammed states. This approach enhances our understanding of relaxation dynamics in highly compressed glassy systems and provides a robust analytical tool for investigating structural characteristics.

Self-organized spatial inhomogeneity in self-propelled quasi-elastic hard disk systems [9]

The freely cooling process in inelastic hard sphere systems has been extensively studied as a fundamental model of granular gases. Here, we investigate the emergence of self-organized spatial inhomogeneities in quasi-elastic hard disk systems through large-scale molecular dynamics simulations. By systematically varying the packing fraction in high-density regimes near the Alder transition point, we identify novel dynamical behaviors and intriguing self-organized spatial patterns not previously reported.

References

[1] M. Isobe: Mol. Sim. **42** (2016) 1317.

[2] E. P. Bernard, W. Krauth, and D. B. Wilson: Phys. Rev. E **80** (2009) 056704.

[3] W. Krauth: Front. Phys. **9** (2021) 229.

[4] M. Klement and M. Engel: J. Chem. Phys. **150** (2019) 174108.

[5] M. Isobe: Int. J. Mod. Phys. C **10** (1999) 1281.

[6] D. Mugita, K. Souno, H. Koyama, T. Nakamura, and M. Isobe: J. Chem. Phys. **160** (2024) 174104.

[7] D. Mugita and M. Isobe: J. Chem. Phys, **161** (2024) 154508.

[8] D. Mugita , K. Souno, and M. Isobe: J. Phys. Soc. Jpn. **94** (2025) 024002.

[9] R. Kitagawa, D. Mugita, N. Murase, and M. Isobe: Proceedings of the 30th Symposium on Traffic Flow and Self-driven Particles, **30** (2024) 9. (in Japanese)

Energy exchange and fluctuations between a dissipative qubit and a monitor under continuous quantum measurement

Tsuyoshi YAMAMOTO

Institute of Pure and Applied Sciences,

University of Tsukuba, Tsukuba, Ibaraki 305-8577, Japan

Quantum measurement can change the state of the measured system, an effect known as *measurement backaction*. Along with this state change, energy can be exchanged between the system and the measurement apparatus. This energy exchange is referred to as quantum heat [1], and it plays a crucial role in the development of quantum thermodynamics and the design of quantum thermal devices.

However, little is known about energy exchange in the presence of dissipation. It has been shown that energy does not flow from the measured system to the measurement apparatus under continuous measurement in the case of a qubit [2]. Nonetheless, the statistical properties remain to be explored.

In this study [3], we focus on the power spectrum, which characterizes the fluctuations in energy flow between a dissipative qubit and a monitor under continuous measurement (see Fig. 1). By solving the stochastic quantum master equation numerically and taking ensemble averaging over 10-100 million trajectories using parallel computation, we find that the fluctuations are unique features of continuous quantum measurement. Notably, the fluctuations can be decomposed into two contributions: quantum jumps and dynamics of measurement backaction. In particular, the latter is a hallmark of continuous measurement and leads to sub-Poisson statistics.

Our findings are expected to guide future developments in measurement-based thermal machines and provide a deeper understanding of quantum thermodynamics in open quantum systems.

This work was supported by the JST Moonshot R&D- MILLENNIA Program Grant No. JPMJMS2061.

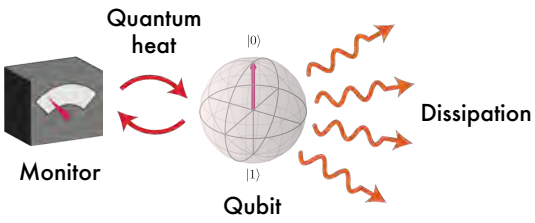

Fig. 1: Schematic of the quantum measurement setup. A measurement apparatus continuously monitors a dissipative qubit.

References

[1] C. Elouard *et al.*, Phys. Rev. Lett. **118**, 260603 (2017).

[2] T. Yamamoto and Y. Tokura, Phys. Rev. Research **6**, 013300 (2024).

[3] T. Yamamoto and Y. Tokura, SciPost Phys. Core **8**, 016 (2025).

Theoretical study of magnetic properties in atomically thin materials

Toshikaze KARIYADO

Research Center for Materials Nanoarchitectonics,

National Institute for Materials Science, Namiki, Tsukuba, Ibaraki 305-0044

We have mainly worked on (1) phonon properties of double wall carbon nanotubes (DWNT) and (2) spin-spin interactions in graphene nanoflakes with decorated edges. The supercomputer is used to perform the first-principles density functional theory (DFT) calculations to analyze structural, electronic, and magnetic properties of DWNT and nanoflakes. We have used Quantum Espresso [1] package for DFT and used Phonopy [2] package for the phonon analysis. Quantum Espresso is well parallelized, and we were able to take advantage of the massive computational resources in the supercomputer.

DWNTs have rich variety in their structures coming from variety in combination of chiralities for inner and outer shells. Experiments show that in some specific combinations of chiralities, there appear new Raman peaks that cannot be explained by superposing Raman spectra from inner and outer shells [3]. Amongst the structures showing new Raman peak, one has relatively small unit cell where the first-principles methods can be applicable. Then, we calculated eigenfrequencies and eigenmodes, and found a mode showing strong hybridization between the inner and outer shells at the frequency of the new Raman peak [3]. The theory suggests that the strong hybridization occurs when the ratio of the radii of the inner and outer shells is close to some simple rational number (in this specific case, 3/5). This well explains the experimental findings.

It is well known that graphene zigzag edges can host magnetism, and it is sensitive to the edge shapes. Then, edge decorated graphene nanofrakes form a promising playground for nanosized spin devices. In this study, we theoretically/numerically proposed a way to have localized spins in nanoflakes, and a way to control the spin-spin interaction between them [4], showing potential of nanoflakes as a foundation for nanoscale spintronics devices.

References

[1] https://www.quantum-espresso.org

[2] https://phonopy.github.io/phonopy/

[3] S. Sun *et al.*, Phys. Rev. Lett., accepted (2025).

[4] T. Kariyado, Materials Today Quantum, accepted (2025).

Dissipative effects on quantum computation

Tatsuhiko Shirai
Waseda Institute for Advanced Study, Waseda University
Nishi Waseda, Shinjuku-ku, Tokyo 169-0051

Thermalization of isolated many-body quantum systems is a fundamental problem in non-equilibrium statistical physics. Although their dynamics follow unitary time evolution, the expectation values of local observables generally relax to those of equilibrium states in the thermodynamic limit. This relaxation can be understood in terms of operator spreading, where a local observable in the Heisenberg picture becomes increasingly delocalized over time, rendering local measurements insensitive to the initial state.

Here, we explore the connection between operator spreading and quantum computation on noisy quantum computers. In recent work [1], we observed that autocorrelation functions in bulk-dissipated many-body quantum systems exhibit accelerated decay during a transient regime before reaching the long-time asymptotic regime. Since noisy quantum computers can effectively be modeled as dissipative many-body systems, we expect this accelerated decay to be observable in such platforms. To investigate this, we consider two-point measurement of a local observable at times $t = 0$ and $t = 2T$, wth the system evolving under noise for the total duration $2T$. The coherent parts of the forward and backward processes (for $0 \leq t \leq T$ and $T \leq t \leq 2T$, respectively) are represented by unitary operators U and $U^\dagger$. We find that the resulting correlation function exhibits the accelerated decay as a function of T. These findings were verified through numerical simulations using OpenMPI (see Fig. 1).

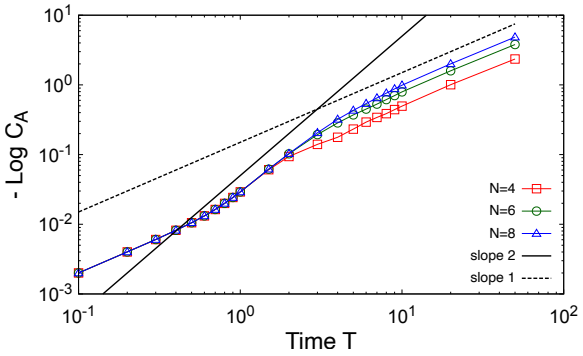

Figure 1: Dependence of the correlation function on execution time T for various system sizes. Accelerated decay is observed in the range $1 \leq T \leq 2$, and the duration of this transient regime increases with system size.

References

[1] T. Shirai, T. Mori: Phys. Rev. Lett. **133**, 040201 (2024).

Long-term reliability assessment of reinforced concrete structures with a surface polymer barrier layer.

T. Ishida[1)], F. Nakai[2)]

1) Department of Materials Physics, Graduate School of Engineering, Nagoya University, Furo-cho, Chikusa, Nagoya 464-8603, Japan

2) Department of Earth and Space Science, Osaka University, 1-1 Machikaneyama, Toyonaka 560-0043, Japan

Low-molecular species (Cl^-, CO_2, O_2, etc.) diffuse through the polymer barrier and concrete cover to reach steel reinforcement and initiate corrosion, which governs the service life of RC structures. To predict the onset of corrosion realistically, we must account for long-term degradation of the polymer coating and model molecular transport through the heterogeneous cementitious matrix. In this project we use coarse-grained molecular dynamics and kinetic Monte Carlo methods to (1) simulate nonequilibrium ageing of the polymer barrier and (2) compute diffusion of low-molecule penetrants in cementitious media, integrating these results to estimate the effective lifetime of coated RC elements.

For polymer degradation simulations, we investigated how the diffusivity of free radicals generated during polymer degradation affects the progression of aging using LAMMPS. The results showed that while low radical diffusivity slightly enhances heterogeneous degradation, its overall impact on the degradation scenario is limited. slightly amplifies localized (heterogeneous) degradation and has a minimal impact on the overall degradation pathway [1].

For the diffusion of penetrants in cement paste, we found that, within a certain short-time regime, the displacement distributions of gas molecules deviate from the Gaussian form, exhibiting heavy tails. The duration of this non-Gaussian behavior depends on both the gas species and the porosity, as shown in Fig. 1 [2].

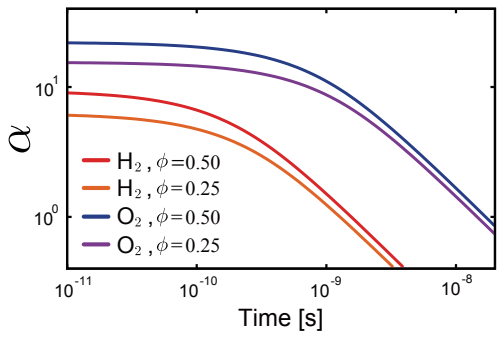

Fig. 1 Duration of the Non-Gaussian Parameter

References

[1] T. Ishida, etal. Polym. J., **56**, 1069–1078 (2024).

[2] F. Nakai, T. Ishida, J Soc Rheol Jpn, **52**(2), 83-89 (2024).

Spin dynamics in J_1-J_3 antiferromagnets on kagome lattices

Kazushi AOYAMA
Department of Earth and Space Science, Graduate School of Science, Osaka University
Machikaneyama-cho, Toyonaka, Osaka 560-0043

Real-space structures of magnetic orders are often reflected in spin dynamics. In this work, we theoretically investigate the spin dynamics in three different types of triple-**Q** states emerging in J_1-J_3 antiferromagnets on the breathing kagome lattice whose Hamiltonian is given by

$$\mathcal{H} = J_1 \sum_{\langle i,j\rangle_S} \mathbf{S}_i \cdot \mathbf{S}_j + J_1' \sum_{\langle i,j\rangle_L} \mathbf{S}_i \cdot \mathbf{S}_j + J_3 \sum_{\langle\langle i,j\rangle\rangle} \mathbf{S}_i \cdot \mathbf{S}_j, \quad (1)$$

where $\mathbf{S}_i$ is a classical Heisenberg spin, J_1 (J_1') is the exchange interaction for the site pair on small (large) triangles, and $J_3 > 0$ is the third nearest neighbor interaction along the bond direction. For strong J_3, a 12-sublattice triple-**Q** state characterized by the three ordering vectors $\mathbf{Q}_1 = \frac{\pi}{2}(-1, -\frac{1}{\sqrt{3}})$, $\mathbf{Q}_2 = \frac{\pi}{2}(1, -\frac{1}{\sqrt{3}})$, and $\mathbf{Q}_3 = \frac{\pi}{2}(0, \frac{2}{\sqrt{3}})$ is favored. It takes a noncoplanar, coplanar, or collinear structure depending on the breathing parameter J_1'/J_1 and temperature T [1]. The noncoplanar state possesses nonzero net chirality $\chi^T \neq 0$, and energetically degenerate two spin configurations can be distinguished by the sign of χ^T.

By numerically integrating the spin-dynamics equation

$$\frac{d\mathbf{S}_i}{dt} = \mathbf{S}_i \times \mathbf{H}_i^{\rm eff}, \quad \mathbf{H}_i^{\rm eff} = -\sum_j J_{ij}\mathbf{S}_j, \quad (2)$$

we calculate the dynamical spin structure factor $S(\mathbf{q},\omega) = |\frac{1}{t_0}\int dt\, \frac{1}{3L^2}\sum_i \mathbf{S}_i e^{-i(\mathbf{q}\cdot\mathbf{r}_i - \omega t)}|^2$ for $t_0 = 1000/J_1$ and $L = 288$, where the initial equilibrium spin configurations are prepared by using Monte Carlo simulations. Although in the collinear and coplanar states, $S(\mathbf{q},\omega)$ is symmetric with respect to the Γ point, it becomes asymmetric in the nonccoplanar case with $\chi^T \neq 0$ (see Fig. 1), suggesting that nonreciprocal spin waves emerge in the chiral phase. It is also found that such an asymmetry flips when the chirality χ^T flips. By further performing the spin-wave expansion, we find that the asymmetry or nonreciprocity microscopically originates from geometric phases acquired in the spin-wave propagation processes [2].

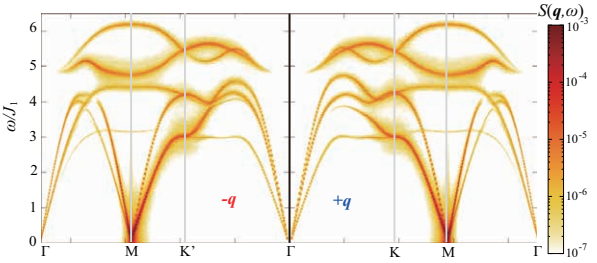

Figure 1: $S(\mathbf{q},\omega)$ obtained in the noncoplanar state for $J_1'/J_1 = 0.8$ and $T/J_1 = 0.08$ [2].

References

[1] K. Aoyama and H. Kawamura: Phys. Rev. B **105**, L100407 (2022); J. Phys. Soc. Jpn. **92**, 033701 (2023).

[2] K. Aoyama and H. Kawamura: Phys. Rev. B **111**, 144413 (2025).

Modeling for interaction between gas-phase reaction with pattern formation and solid surface

Takaki AKIBA

Department of Mechanical Engineering,

The University of Tokyo, Hongo, Bunkyo-ku, Tokyo 113-8656

To understand the coupled physics of gas-solid interactions in reacting flows, methods for chemical reaction simulation were developed.

Three-dimensional combustion models with two variables of temperature and fuel concentrations were designed for GPU acceleration (Fig. 1). Previously the simulation was designed for MPI with multi-node CPU clusters. With the use of GPU resources at ISSP C system through CUDA SDK with a Fortran interface, we achieved comparable performance using a single GPU chip, matching the computing speed of over 2000 MPI processes on CPUs.

Another framework was developed for chemical reaction simulations for quantum computing. As quantum computers can only handle problems described by linear algebra, while the chemical reaction inherently involves non-linearities due to collisions and temperature-dependent reaction rates, we applied Carleman linearization to bridge this gap. Carleman linearization transforms nonlinear systems into high-dimensional linear systems that preserve essential nonlinear behavior. However, the resulting linear systems are often too large to solve efficiently. In this project, the linearization pre-process was performed on CPU, while the solution of the large linear system was accelerated using the CUDA SDK with a C++ interface on GPU. This hybrid approach achieved over a tenfold speedup compared to a CPU-only implementation (Fig. 2).

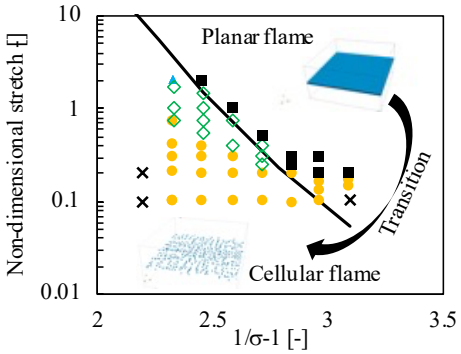

Fig. 1 Flame transition with three-dimensional combustion simulation

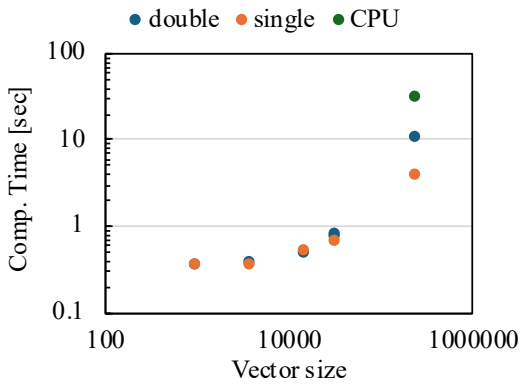

Fig. 2 GPU acceleration for chemical reaction problems with Carleman linearization.

Solitons and phase transitions in quantum chiral spin model in tilted magnetic field

Yusuke MASAKI
Department of Applied Physics, Tohoku University
Sendai, Miyagi 980-8579

Classical spin models of monoaxial chiral magnets predict a continuous phase transition (CPT), known as the Dzyaloshinskii transition, driven by chiral solitons under magnetic fields perpendicular to the helical axis (nucleation-type CPT, Fig. 1). In tilted magnetic fields, two multicritical points, T and M (Fig. 1), emerge, leading to discontinuous phase transitions (DPTs) in intermediate angular regions due to attractive soliton interactions. Recent theoretical investigations of the corresponding quantum spin models (which we call quantum monoaxial chiral magnets) have revealed novel phenomena, such as spin parity effects in small systems with periodic boundary conditions and quantum tunneling across surface barriers in magnetization processes. However, how quantum nature of spins modifies classical phase transitions, such as DPTs and the Dzyaloshinskii transitions in Fig. 1, remains unexplored.

This year, we have numerically investigated magnetization process and phase transitions in quantum monoaxial chiral magnets under tilted magnetic fields using the density matrix renormalization group (DMRG) and tensor renormalization group (TRG). Our DMRG calculations suggest that the first-order behavior persists for $S \geq 1$, but transitions become continuous for $S = 1/2$. DMRG results on the surface-spin modulation indicate attractive soliton interactions, which can explain the origin of the DPTs, consistent with classical results. However, for $S = 1/2$, the order of

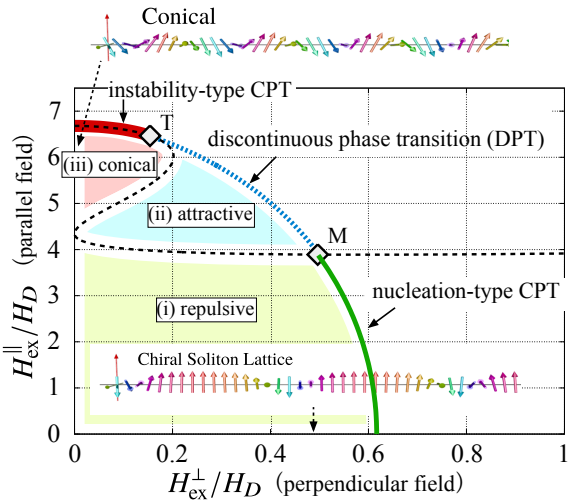

Figure 1: Phase diagram of a classical spin model for a monoaxial chiral magnet under a tilted magnetic field.

the phase transitions is altered probably due to quantum tunneling. We have also studied phase transitions through magnetization curves and energy gaps using tensor network methods, specifically the higher-order TRG, enabling precise calculations for large systems with periodic boundary conditions. Our results identify a distinct point on the CPT line for S=1/2, at which the nature of the CPT changes, while the whole phase boundary remains continuous. This structure is reminiscent of the finite-temperature phase diagrams, where thermal fluctuations compress the DPT region into a single critical point.

Density of States for Selenium Chains Confined in Carbon Nanotubes Through First-Principles Calculations

Md Saiful ISLAM and Hiroyuki IKEMOTO
Department of Physics, University of Toyama, Toyama, 930-8555, Japan

Selenium (Se) is a group 16 element in the periodic table that belongs to the chalcogen family and exhibits unique structural properties. As a chalcogen, selenium naturally forms a hierarchical structure, where the primary structure is a three-turn helical chain and these chains further assemble to form the trigonal selenium (t-Se) crystal structure. Isolated selenium chains are interesting because they are one dimensional system and lack the inter-chain interactions present in the bulk. Our X-ray absorption fine structure measurements showed a temperature-dependent drop in the coordination number of selenium confined in single-walled carbon nanotubes (Se@SWCNT), suggesting a possible Peierls transition—a metal-to-semiconductor phase transition associated with splitting of the covalent bond into two types [1].

We conducted ab-initio calculations employing the Quantum ESPRESSO package, which is based on density functional theory (DFT) with plane-wave basis sets and pseudopotentials. We used the generalized gradient approximation (GGA) with the Perdew–Burke–Ernzerhof (PBE) exchange-correlation functional. Self-consistent field (SCF) calculations were performed to optimize the energy and k-point meshes for each system. The electronic density of states (DOS) was then computed for SWCNT, Se@SWCNT, and various isolated selenium chains including a three-turn helical chain, two collinear chains, and a planar zigzag chain.

Figure 1 compares the DOS of candidate selenium chain structures within SWCNT. The first candidate is a three-turn helical chain, as it is the primary structure for bulk t-Se; the second one is two collinear chains, which was suggested by electron spectroscopy [1], and the third one is a planar zigzag conformation which was expected in sulfur case [2]. According to Figure 1, while the three-turn helical chain exhibits semiconducting behavior, both the two collinear chains and the planar zigzag chain display metallic characteristics. These findings indicate that the electronic properties of selenium are highly sensitive to its structural conformation.

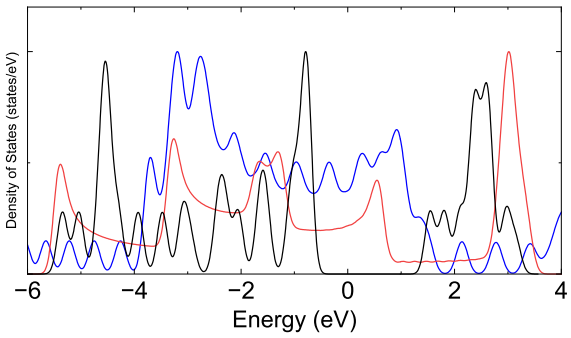

Figure 1: DOS for selenium structures: three turn helical chain (black), two collinear chains (blue), and a planar zigzag chain (red).

We are performing photoemission spectroscopy (PES) measurements on single-wall CNT (SWCNT) and Se@SWCNT to obtain DOS of the selenium confined in single-wall CNTs (SWCNT). PES signals are sensitive to

surface material, so PES of Se@SWCNT was very close to SWCNT. At this stage, we obtained the PES for confined selenium chains by subtracting the PES spectrum of Se@SWCNT from that of SWCNT. However, this method may oversimplify the actual spectral contributions. Therefore, to assess the validity of this approach, theoretical calculations are crucial.

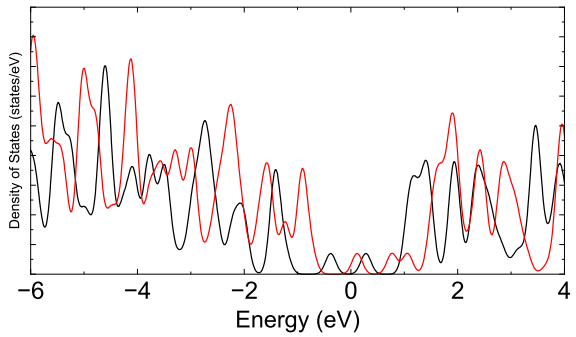

Figure 2: The DOS of SWCNT (black), and Se@SWCNT (red).

Figure 2 presents the DOS of the SWCNT, and the combined Se@SWCNT system. The obtained DOS were clearly different from each other, which was different from PES signal. The difference may come from two reasons, one is that PES signals are sensitive to the surface, and the other is the precision of the calculations.

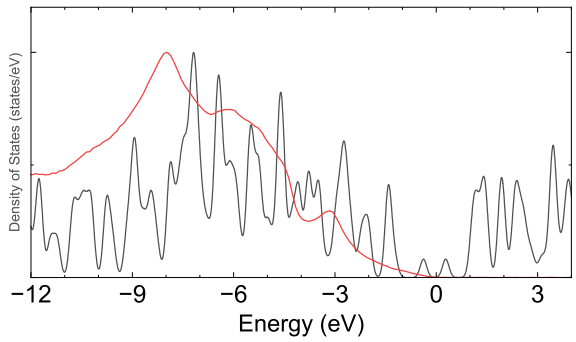

Figure 3: Comparison of the theoretical (black) and experimental (red) DOS of SWCNT.

Figure 3 compares the theoretical and experimental DOS for SWCNTs. The theoretical DOS exhibits sharper features compared to the broad peaks seen experimentally. This discrepancy could be due to differences in chirality, and diameter of the SWCNT model, or insufficient broadening in the theoretical model. Alternatively, it may indicate that the computational parameters require reconsideration.

Therefore, to obtain DOS of confined selenium chain in SWCNT, we have to first focus on improving our calculations. After reconsidering the calculation model and parameters, we will perform new calculations and carry out a detailed comparison with the experimental data to gain deeper insights into the structural–electronic correlations in confined selenium systems.

References

[1] H. Ikemoto, T. Fujimori, T. Miyanaga, R. Kawaguchi, K. Urita, and M. Tabuchi, *Structures of Se chains encapsulated in single-walled carbon nanotubes*, J. Phys. Chem. Solids **185**, 111737 (2024).

[2] T. Fujimori, A. Morelos-Gómez, Z. Zhu, H. Muramatsu, R. S. Sinha, M. Terrones, M. Endo, and K. Kaneko, *Conducting linear chains of sulphur inside carbon nanotubes*, Nature Communications, **4**, 2162 (2013).

Friction law for macroscopic objects driven at high speed

Michio OTSUKI

Graduate School of Engineering Science,

The University of Osaka, Machikaneyama, Toyonaka, Osaka 560-8531

In sliding contact of viscoelastic material, it is known that hysteresis friction occurs due to the delay in deformation caused by viscosity. However, many aspects remain unexplored regarding the behavior of hysteresis friction at high sliding velocities near the elastic wave velocity, such as those observed in airplane tires during landing.

In this study, we investigate hysteresis friction on a rigid indenter in sliding contact with a viscoelastic substrate using finite element simulations. The computational size is 1,000,000 nodes and 100,000,000 time steps. The calculation takes 12 hours using our in-house code compiled with the Intel Fortran compiler and 300 MPI processes on the CPU servers. Here, the Young's modulus of the viscoelastic substrate is E, the density is ρ, and the viscosity coefficient is $\tilde{\eta}$.

As shown in Fig. 1, the friction coefficient μ depends on the sliding velocity V and has a peak at a certain velocity that depends on the viscosity coefficient $\tilde{\eta}$. Furthermore, we find that the friction coefficient μ changes dramatically at sliding velocities near the elastic wave velocity scale $c = \sqrt{E/\rho}$ due to a singular deformation [1].

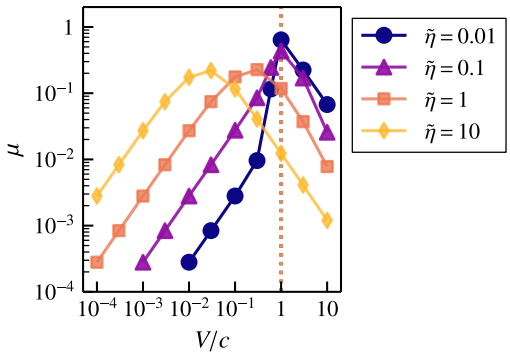

Fig. 1: Dependence of friction coefficient μ on sliding velocity V/c for various viscosity coefficients $\tilde{\eta}$. The vertical dashed line represents the elastic wave velocity scale $V/c = 1$.

References

[1] W. Iwashita and M. Otsuki, The 4th Malaysian International Tribology Conference (MITC2024), 69 (2024).

On the microstructure and loading behavior of graphene-nanospacer structure with molecular dynamics simulation

Mingda Ding, Taiki Inoue, Yoshihiro Kobayashi

Department of Applied Physics, The University of Osaka, Yamadaoka, Suita, Osaka 565-0871

This year, we studied the microstructure of graphene (Gr) stacking structures with nanodiamond (ND) nanospacer and the effect of carbon nanotube (CNT) spacers on the mechanical behavior of using molecular dynamics (MD) simulations. The insertion of nanospacers between Gr layers effectively modulates the interlayer distance and interlayer interaction [1]. The insertion of CNTs can also change the mechanical response of multilayer Gr [2]. By adjusting the inter-spacer distance and the size of CNTs, we gain insight into the deformation mechanisms and energy variations in these nanostructures.

MD simulations were conducted using the open-source software LAMMPS (Large-scale Atomic/Molecular Massively Parallel Simulator). The system sizes ranged from 10,000 to 800,000 atoms, depending on the lateral size of the Gr layers. The AIREBO potential was used to describe the short-range interactions, while the Lennard-Jones (LJ) potential was employed for interlayer van der Waals interactions. Dynamic relaxation was performed using the velocity-Verlet algorithm to obtain energy-minimized structures.

Computational resources were allocated across different systems based on the complexity of the simulation. Large-scale graphene and nanodiamond (Gr-ND) simulations were primarily conducted on System B (Ohtaka) with 2–4 nodes, requiring a computational time of 16–72 hours per simulation. In contrast, the graphene and carbon nanotube (Gr-CNT) stacking structures, which typically required smaller system sizes, were simulated on System C (Kugui) using 1–2 nodes with a computational time of 5–24 hours per simulation.

The MD simulations focused on two types of stacking structures: Gr-ND (Figure 1a) and Gr-CNT (Figure 1b). By applying periodic boundary conditions, systems with different areal densities of NDs and CNTs were examined. Additionally, simulations were performed with various diameters of nanospacers to analyze their influence on the transition between Gr layer separation and interlayer adhesion. The results showed that a decrease in nanospacer areal density led to a transition from Gr layer separation to interlayer adhesio, consistent with our experimental

observations. Moreover, larger nanospacers required a higher critical areal density to maintain suspension. Energy analysis revealed that the difference between deformation energy and adhesion energy of the separation and adhesion structure governs the stability of different configurations [1].

modulation of multilayer Gr structures via nanospacer insertion. The findings contribute to the functional enhancement of multilayer Gr for potential applications in flexible electronics, coatings, and energy storage devices.

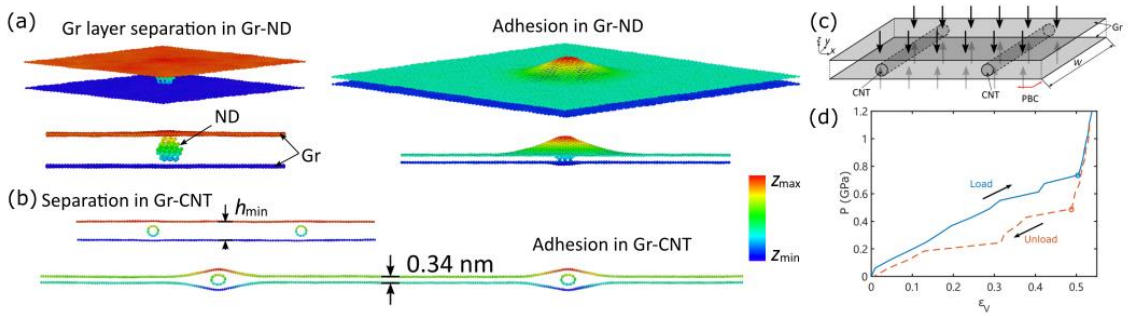

Figure 1 (a) Deformed configuration obtained by MD simulation of graphene (Gr) and nanodiamond (ND) stacking structure (Gr-ND) with Gr layer separation (shorter inter-ND distance) and adhesion (larger inter-ND distance). (b) Gr and carbon nanotube (CNT) stacking structure (Gr-CNT) with Gr layer separation (shorter inter-tube distance) and adhesion (larger inter-tube distance). (c) The schematic of the loading press of Gr-CNT stacking structure. (d) Loading-unloading curve of the Gr-CNT stacked structure with hysteresis.

Then, the loading-unloading pressure (Figure 1c) is imposed on the Gr-CNT system [2]. The hysteresis force curve is observed, which means the loading and unloading curves are inconsistent (Figure 1d). The hysteresis is the symbol of energy dissipation. The energy dissipation is verified by experiment and has application in lightweight damping and energy absorption structures.

Our study provides fundamental insights and mechanism exploration into the mechanical

References

[1] M. Ding, T. Inoue, J. I. Enriquez, H. H. Handoko, Y. Ogawa, Y. Taniyasu, Y. Hamamoto, Y. Morikawa, Y. Kobayashi, Carbon **229**, 119464 (2024).

[2] M. Ding, N. Sakurai, T. Inoue, T. Matsuzaki, T. Mizuno, K. Suzuki, J. I. Enriquez, H. H. Halim, Y. Hamamoto, H. Yoshikawa, Y. Morikawa, Y. Kobayashi, (In preparation).

Development of integrated interface of eigensolvers Rokko and application to quantum spin systems

Tatsuya Sakashita
Department of Physics, The University of Tokyo
7–3–1 Hongo, Bunkyo-ku, Tokyo 113–0033

To establish universal exact diagonalization package for quantum lattice models including the Heisenberg–Kitaev model, we focused on developing integrated interfaces for eigensolvers, "Rokko" [1].

In Rokko, we implemented the integrated interfaces for the following types:

- Serial solvers for dense matrices (Eigen3, LAPACK)
- MPI parallelized solvers for dense matrices (EigenExa [2], ELPA [3], Elemental [4], ScaLAPACK)
- MPI parallelized solvers for sparse matrices (Anasazi in Trilinos [5], SLEPc [6]) to cover matrix representations below:
  - CRS (Compressed Row Storage)
  - Matrix-free method (the method to give matrix-vector product routines to solvers)

Rokko has the following features:

- Integrated interfaces for eigensolvers and matrices, independent of individual eigensolver libraries
- Rokko's interfaces are implemented by utilizing factory. It enables the user to dynamically select a solver.
- C, Fortran, and Python bindings of Rokko
- Automatically detecting libraries by using CMake in building Rokko
- Unit and integrated test programs by GoogleTest
- Install scripts of eigensolvers for various architectures

We prepare a paper to report design policy, software structure, and usage examples of Rokko.

References

[1] T. Sakashita, R. Igarashi, Y. Motoyama, T. Okubo, and S. Todo. Repository of Rokko. `https://github.com/t-sakashita/rokko.git`, 2012.

[2] T. Imamura, T. Hirota, and T. Fukaya. EigenExa web page. `https://www.r-ccs.riken.jp/labs/lpnctrt/projects/eigenexa/`, 2021.

[3] ELPA Consortium. ELPA (Eigenvalue soLvers for Petaflop Applications web page). `https://elpa.mpcdf.mpg.de/`, 2013.

[4] J. Poulson. Distributed-memory dense linear algebra Elemental web page. `https://github.com/elemental/Elemental`, 2013.

[5] M. A. Heroux, R. A. Bartlett, and V. E. Howle. Trilinos Project web page. `https://trilinos.github.io`, 2003.

[6] V. Hernandez, J. E. Roman, and V. Vidal. SLEPc web page. `http://slepc.upv.es`, 2002.

Structure analysis of atomic layer alloy with Rashba effect studied by TRHEPD

R. Takahashi[A], L. Konermann[A], I. Mochizuki[B], K. Wada[B], T. Hyodo[B] and A. Takayama[A,C]

[A]*Department of Physics, Waseda University, Ohkubo, Shinjuku-ku, Tokyo 169-8555*

[B]*IMSS, KEK, Oho, Tsukuba, Ibaraki 305-0801*

[C]*IMRAM, Tohoku University, Katahira, Sendai, Miyagi 980-8577*

Introduction

The superconducting phenomenon that occurs in the spin-split electronic state due to the Rashba effect is theoretically predicted to be an unconventional superconducting state where *s*-wave and *p*-wave superconductivity coexist (Rashba-SC). In order to investigate the details of this Rashba-SC, material exploration and research on its electronic states are being actively conducted. Previous studies have shown that (Bi, Pb) single-atom layer (SAL) alloys on Ge(111) and Si(111) substrates are predicted to exhibit Rashba-type spin-split bands due to the strong spin-orbit coupling of Pb and Bi [1]. We revealed several metallic electronic states exhibit with spin-splitting in the (Bi, Pb)-Ge(111)-2×2 structure by angle- and spin-resolved photoemission spectroscopy.

In this study, we performed structural analysis of several SAL structures exhibiting the Rashba effect in order to discuss the details of the Rashba effect in SAL structures from a structural perspective, using by total-reflect high-energy positron diffraction (TRHEPD). Here, we report mainly on structural analysis of Bi/Ge(111), Pb/Ge(111), and (Bi, Pb)/Ge(111).

Experiments and analysis methods

The TRHEPD measurements were performed at the Slow Positron Facility, KEK. The TRHEPD experiment involves measuring a series of diffraction patterns for a fixed incident azimuthal direction at various glancing angles (θ). In this context, the rocking curve (RC) is defined as the diffraction intensity of the (00) spot plotted as a function of θ.

In the structural analysis, the experimental rocking curves are compared with those calculated for various structural models. The locking curves for each structure were calculated and compared with experimental results using the structural analysis program ODAT-SE (2DMAT) [2]. Specifically, large-scale calculations were performed on supercomputers, including: (i) long-period structure induced by the striped-incommensurate (SIC) phase in Pb/Ge(111), and (ii) structural analysis with multiple parameters set for (Bi, Pb) SAL structure with unclear structural model.

Results and discussion

Figure 1(a) shows the results of structural analysis for Pb/Ge(111)-√3×√3 structure. The RC calculated from the structural model proposed by Otsubo *et al*. [3] reproduced the experimental results relatively well. In this study, structural optimization was performed using Nelder-Mead method, and we concluded that the structural model shown in Fig. 1(a) is the most reliable. Additionally, rocking curves were

calculated for a long-period structure incorporating the SIC phase, which revealed that there were no significant changes in the calculation results. Structural analysis was also performed on Bi/Ge(111)- √3×√3 structure, as shown in Fig. 1(b). The RC calculated from the structural model proposed in previous study [4] reproduced the experimental results very well. In both structures, it was found that there was almost no structural relaxation of Ge in the out-of-plane direction. Furthermore, we also found that slight differences in the in-plane positions of Pb (T_4 site) and Bi (T_1 site) atoms greatly affect the shape of RC.

Figure 2 shows the RCs of (Bi, Pb)/Ge(111)-2×2 structure and the RCs calculated from the structural model proposed in previous studies. The calculated RC from the 2×2 structure model proposed by Mihalyuk *et al*. [1] does not match the experimental RC. Currently, we are performing structural analysis following two different approaches. The first approach is structural optimization based on the Mihalyuk model. In this approach, the structure can be determined by varying the distances and configurations between atoms. The second proposal addresses the fact that the ratio of Bi and Pb in the 2×2 unit cell has not yet been determined. To investigate this, we will investigate structural models by adjusting the atomic densities of Pb and Bi as parameters.

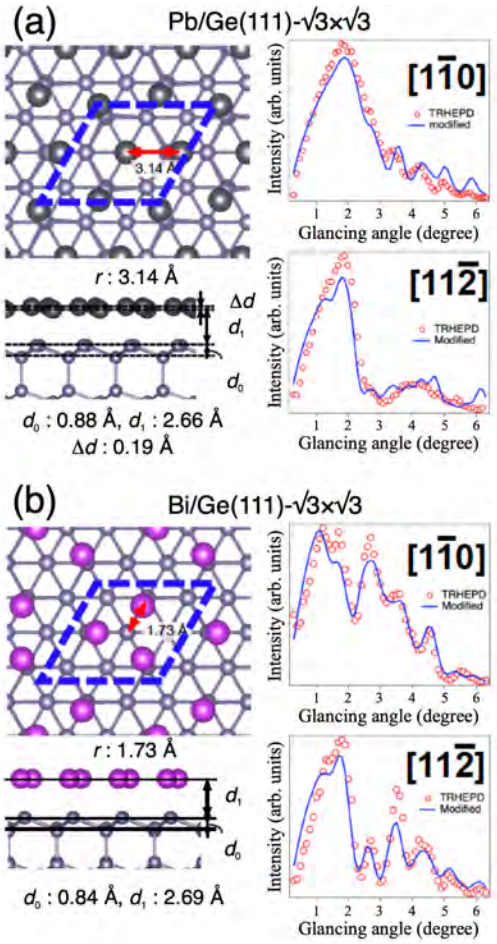

Fig. 1: Results of structural analysis by TRHEPD of (a) Pb/Ge(111)-√3×√3 and (b) Bi/Ge(111)-√3×√3. (left) Determined structural model. (right) RCs with calculated curves under many-beam conditions.

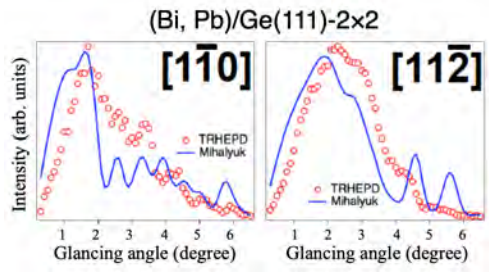

Fig. 2: RCs under many-beam conditions for (Bi, Pb)/Ge(111)-2×2 structure with calculated curves from proposed structural model in previous study [1].

References

[1] A. Mihalyuk, *et al*., Front. Mater. **9**, 882008 (2022).
[2] Y. Motoyama, *et al*., Computer Physics Communications, **280** (2022) 10846.
[3] Y. Ohtsubo, *et al*., J. Phys.: Condens. Matter., **23**, 435001 (2011).
[4] Y. Ohtsubo, *et al*., J. Phys.: Condens. Matter., **21** 405001 (2009).

Molecular spin dynamics study on the multiple-Q orders in Hubbard models

Takashi UCHIDA
Hokkaido University of Science
4-1, 7-15, Maeda, Teine-ku, Sapporo 006-8585

Recently, the magnetic structures of multiple-Q states have attracted attention since the topologically protected magnetic structures such as magnetic skyrmions emerge as 3Q helical orders in the Dzyaloshinskii-Moriya (DM) interaction driven systems under magnetic field. The topologically nontrivial multiple-Q orders can also be realized in centrosymmetric systems where the DM interaction is absent [1]-[3]. The stabilization mechanism of multiple-Q orders in the latter systems, however, is not unique and still under investigation.

The purpose of the present research is to investigate the stability of multiple-Q orders in the centrosymmetric triangular-lattice single-band Hubbard model by means of the molecular spin dynamics (MSD) method [4]. The present formulation of the MSD adopts the static approximation to the functional integral method and the isothermal molecular dynamics technique, and reduces to the generalized Hartree-Fock approximation at the ground state.

In the present MSD scheme, the most time-consuming process in the numerical calculations is the magnetic force calculation at each time step, where the local electronic structures are calculated in real space by means of the recursion method [4]. We have adopted the MPI parallel calculation scheme and found it effective in saving both computing time and CPU resources.

In the present work, we have included the 3rd neighbor hopping integral t_3 in addition to the nearest neighbor hopping integral t_1 in the Hubbard model. We have performed magnetic structure calculations on a hexagonal supercell with 972 lattice points, which is embedded in a large cluster consisting of 6 such supercells, each of which are connected by the periodic boundary condition. Under zero magnetic field and the fixed value of the temperature $T/t_1 = 0.0005$, we have explored the magnetic structures changing the Coulomb interaction strength U/t_1, the hopping integral ratio t_3/t_1, and the electron number n. For $t_3/t_1 = -0.40$, $n = 1.21$ and $U/t_1 = 7.0$, the dominant magnetic order was found to be a 3Q noncoplanar order with commensurate wave vectors $\boldsymbol{Q_1} = (2\pi/a)(1/3, 0)$, $\boldsymbol{Q_2} = (2\pi/a)(-1/6, \sqrt{3}/6)$ and $\boldsymbol{Q_3} = (2\pi/a)(-1/6, -\sqrt{3}/6)$ (a being the lattice constant). The electronic density of states becomes zero in the vicinity of the Fermi energy E_{F}, opening a gap at E_{F}. This suggests that the Fermi surface nesting occurs for the wave vectors $\boldsymbol{Q_1}$, $\boldsymbol{Q_2}$ and $\boldsymbol{Q_3}$, stabilizing the 3Q orders.

References

[1] T. Okubo, S. Chung, and H. Kawamura: Phys. Rev. Lett. **108** (2012) 017206

[2] Y. Kakehashi: J. Phys. Soc. Jpn. **89** (2020) 094710.

[3] K. Kobayashi and S. Hayami: Phys. Rev. B**106** (2022) L140406.

[4] Y. Kakehashi, S. Akbar, and N. Kimura: Phys. Rev. B**57** (1998) 8354.

Proposal of novel superconducting states coexisting/competing with higher-order magnetic multipole order or helical magnetism

Shuntaro SUMITA
Department of Basic Science, The University of Tokyo, Meguro, Tokyo 153-8902

We have theoretically studied a variety of intriguing topological phenomena in strongly correlated electron systems by using numerical methods including first-principles calculations, quantum many-body calculations, and machine learning (project number: 2024-Ba-0030). During the last fiscal year, we have achieved some progress on the following topics.

(1) Superconducting states coexisting with altermagnetism

We conducted a study on spatially non-uniform superconducting states coexisting with altermagnetism [1], which is known as a higher-order magnetic multipole order exhibiting anisotropic spin splitting in the energy bands despite a conventional collinear antiferromagnetic structure. Focusing on the organic salt κ-$(ET)_2X$, a candidate material for altermagnetism, we constructed an effective two-sublattice tight-binding model (cf. Ref. [2]) and performed many-body calculations incorporating a molecular field representing the magnetic order. Specifically, assuming an onsite repulsive Hubbard interaction, we analyzed the linearized Eliashberg equation based on the random phase approximation. In this analysis, we employed the Matsubara Green's function method and utilized the `SparseIR.jl` package [3], which is based on the intermediate representation [4] and the sparse sampling [5], to reduce memory usage and computation time. As a result, we demonstrated that Fulde–Ferrell–Larkin–Ovchinnikov (FFLO) superconductivity, a spatially non-uniform state characterized by a finite center-of-mass momentum, can be stabilized by altermagnetism, obtaining results consistent with several previous theoretical studies [6–10].

Next, to understand this spatially non-uniform state from the perspective of phenomenological parameters, we conducted an analysis based on Ginzburg–Landau (GL) theory. Specifically, within the microscopic tight-binding model, we numerically determined the coefficients of the GL free energy, assuming a superconducting mean-field theory with a d-wave order parameter. Our analysis revealed that as the molecular field of altermagnetism increases, the coefficient κ of the second-order gradient term changes its sign from positive to negative, while the coefficient β of the fourth-order uniform term remains positive. Consequently, the FF state, in which only the *phase* of the order parameter is spatially modulated, is stabilized.

(2) Magnetic resonance peaks in UTe_2

We studied the magnetic resonance peaks in the heavy-fermion superconductor UTe_2 [11], which was discovered in late 2018. Based on a mixed-dimensional periodic Anderson model that reproduces the antiferromagnetic fluctuations observed near $\boldsymbol{q}_{\mathrm{AFM}} = (0, \pi, 0)$ in this material [12], we assumed a spin-triplet superconducting order parameter and calculated the dynamical spin susceptibility within the random phase approximation to investigate the presence of resonance peaks by examining its imaginary part. As a result, we demonstrated that when the order parameter belongs to the B_{2u} representation that changes its sign upon momentum transfer of $\boldsymbol{q}_{\mathrm{AFM}}$, a magnetic resonance peak appears at an energy corresponding to the su-

perconducting gap. Furthermore, we found that while the order parameter belonging to the A_u representation also exhibits a sign change, it vanishes in the $\boldsymbol{k}$-space region that dominantly contributes to the spin susceptibility, thereby preventing the emergence of a resonance peak.

References

[1] S. Sumita, M. Naka, and H. Seo, in preparation.

[2] M. Naka *et al.*, Nat. Commun. **10**, 4305 (2019).

[3] M. Wallerberger, *et al.*, SoftwareX **21**, 101266 (2023); T. Wang *et al.*, Phys. Rev. B **102**, 134503 (2020).

[4] H. Shinaoka *et al.*, Phys. Rev. B **96**, 035147 (2017).

[5] J. Li *et al.*, Phys. Rev. B **101**, 035144 (2020).

[6] S. Sumita *et al.*, Phys. Rev. Research **5**, 043171 (2023).

[7] S.-B. Zhang *et al.*, Nat. Commun. **15**, 1801 (2024).

[8] D. Chakraborty and A. M. Black-Schaffer, Phys. Rev. B **110**, L060508 (2024).

[9] G. Sim and J. Knolle, arXiv:2407.01513.

[10] K. Mukasa and Y. Masaki, arXiv:2409.08972.

[11] K. Shimura, S. Sumita, and Y. Kato, in preparation.

[12] R. Hakuno *et al.*, Phys. Rev. B **109**, 104509 (2024).

Analysis of phase transition in languages based on Combinatory Categorial Grammar

Takehito SUZUKI
Department of Human Science, Takachiho University
2-19-1, Omiya, Suginami-ku, Tokyo 168-8508

Language has been attracted the interests of researchers in the field of physics (e.g., [1, 2, 3]). However, grammar for natural language has not been considered there. We employ the combinatory categorial grammar (CCG) to deal with natural languages mathematically. The definition of CCG is as follows. First, we consider ground categories noun (N), noun phrase (NP), and sentence (S). We also employ operators / and \. These operators combine two categories into a single category. Let us consider two categories A and B. The combination A/B indicates that if the category B emerges just after this category, the category is merged into the category A. The combination A\B indicates that if the category B emerges before this category, the category is merged into the category A. For example, let us write intransitive verb with CCG. If the noun phrase comes before the intransitive verb, the sentence is completed. We therefore conclude that the intransitive verb is a category S\NP. An additional example involves the use of the adjective, which can be expressed as N/N with CCG. Notably, the operators can be utilized recursively. With this framework, all categories are represented by the combinations of N, NP, S, /, and \. The categories other than the ground categories are called syntactic categories.

Actually, we need other rules for representing natural sentences. We write the sequence for the categories A and B as A+B. We require the following rules,

$$\mathrm{A/B} + \mathrm{B/C} \to \mathrm{A/C}, \tag{1}$$

$$\mathrm{B\backslash C} + \mathrm{A\backslash B} \to \mathrm{A\backslash C}, \tag{2}$$

where A, B, and C are categories. Equations (1) and (2) are called forward and backward functional composition rules, respectively. For example, if we employ the rule (1), the sequence with the auxiliary verb ((S\NP)/(S\NP) with CCG) and the transitive verb ((S\NP)/NP) is merged into (S\NP)/NP, which is the same as the transitive verb.

We also assume the following rules.

$$\mathrm{A} \to \mathrm{T/(T\backslash A)}, \tag{3}$$

$$\mathrm{A} \to \mathrm{T\backslash(T/A)}, \tag{4}$$

where A is a category and T is a categorical variable. Any category can be substituted for T. Both the rules (3) and (4) are called the forward and backward type raising rules, respectively.

We now treat CCG mathematically. First, we define W_i^l as the combined category C_i from the beginning of the sentence to the lth word, where l is an arbitrary integer, $i = 1, 2, \cdots, N_C$, and N_C is a number of the categories. We found that $N_C = 19$ for English sentences (see Table 1). Note that the end of the sentence is defined as the category $C_Q = C_{12}$. We then define the category vector, $\boldsymbol{W}^l$, as

$$\boldsymbol{W}^l \equiv (W_1^l \;\; W_2^l \;\; \cdots \;\; W_{N_C}^l). \tag{5}$$

Table 1: All categories

Index	Category	Part-of-speech
1	N	noun
2	NP	noun phrase
3	S	sentence
4	S\NP	intransitive verb
5	(S\NP)/NP	transitive verb
6	N/N	adjective
7	(S\NP)\(S\NP)	adverb
8	(S\NP)/(S\NP)	auxiliary verb
9	(S\NP)\(S\NP)/NP	proposition (adverb-like)
10	(NP\NP)/NP	proposition (adjective-like)
11	NP/N	article
12	Q	-
13	S/NP	-
14	S/(S\NP)	-
15	NP/NP	-
16	NP\NP	-
17	S/N	-
18	(S\NP)\(S\NP)/N	-
19	(NP\NP)/N	-

Using this vector, we found that $\boldsymbol{W}^{l+1}$ and $\boldsymbol{W}^{l}$ are related via the equation

$$\boldsymbol{W}^{l+1} = \boldsymbol{W}^{l} G, \tag{6}$$

where G is a matrix, whose components are categories, not real numbers. Moreover, using Eq. (6) recursively leads to the equation

$$\boldsymbol{W}^{l+1} = \boldsymbol{W}^{1} G^{l}. \tag{7}$$

We now assume that the sentence begins with an article. Therefore, we have

$$\boldsymbol{W}^{1} = (0\ 0\ 0\ 0\ 0\ 0\ 0\ 0\ 0\ 0\ C_{11}\ 0\ 0\ 0\ 0\ 0\ 0\ 0\ 0). \tag{8}$$

Using Eq. (7), we can obtain all patterns consisting of L categories, where L is an integer. We can regard L as the sentence length. In particular, the 12th component of $\boldsymbol{W}^{L+1}$ gives such all patterns; note again that the sentence ends with C_{12}.

Moreover, using G, we can also obtain the probability that the sentence length is L. Therefore, we can obtain the average value of L, $\langle L \rangle$. Though the convergence is found to be slow, we can conclude with numerical calculations that $\langle L \rangle$ takes almost 10, which is near but a little smaller than the observed values. This discrepancy could be attributed to the exclusion of certain representations, such as parallel representations, from the analysis. This study is a basis for the future study related to the phase transition observed in natural languages.

References

[1] E. De Giuli: J. Phs. A: Math. Theor. **52**, 504001 (2019).

[2] T. Yamamoto, S. Yamada, and T. Mizuguchi: Eir. Phys. J. B **94**:200 (2021).

[3] K. Nakaishi, and K. Hukushima: Phys. Rev. Res. **4**, 023156 (2022).

Entanglement analysis for cyclic polymers

Takahiro MURASHIMA

Department of Physics, Tohoku University,

Aramaki-aza-Aoba, Aoba-ku, Sendai, Miyagi, 980-8578

Recent advances in synthetic technology have produced polymers with complex topologies. In particular, the physical properties of complex polymers with many rings have attracted much attention. We have so far clarified the physical properties of linear polymers penetrating into cyclic polymers. On the other hand, there is no easy analytical method for the penetration between cyclic polymers, so a clear relationship with the physical properties has not been clarified. In this study, coarse-grained molecular dynamics simulations were carried out on the ISSP supercomputer to obtain many equilibrium structures, and a method for analysing equilibrium structures was investigated.

The N-dependence of the diffusion coefficient was investigated by determining the mean-square displacement of cyclic polymers using the multiple tau method reported last year[1], and it was found that the power exponent of the N-dependence of the diffusion coefficient decreases around a chain length N above 400. Increased entanglement and penetration between cyclic polymers is to be expected as N increases, but when normal primitive path analysis is performed, the cyclic polymers converge to a single point and the penetration state cannot be correctly captured. Therefore, an attempt was made to carry out primitive path analysis[2] in sequence by fixing all but one ring of interest and scrinking only the ring of interest. Figure 1 shows the penetrated rings resulting from this new primitive path analysis method. It was found that this method can be used to obtain the appearance of rings penetrating each other. A method to automatically determine which rings penetrate which rings needs to be developed.

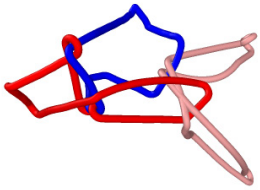

Fig. 1: Three interpenetrating cyclic polymers

References

[1] T. Murashima, ISSP Activity Report 2023, 298.

[2] https://github.com/t-murash/LAMMPS-PPA

General algorithm of calculating the SU(N) symmetry coefficients for a generic N

Masahiko G. YAMADA
Department of Physics, School of Science, University of Tokyo
Hongo, Bunkyo-ku, Tokyo 113-0033

We have studied a general algorithm of calculating the SU(N) symmetry coefficeints. This is problematic in the case N is large, for example $N > 4$. The sophisticated algorithm is necessary and the previous method based on Clebsch-Gordan coeffcients is not efficient enough for a large-scale simiulation, e.g. for the density matrix renormalization group (DMRG).

The calculation of F-symbols (6j-symbols for SU(2)) or R-symbols is done by the method discussed in Chen's textbook [1] based on subduction coefficients. This method is specifically suitable for the case $N > 4$ and the calculation is easily parallelized and made fast by many nontrivial techniques. Calculations for SU(5) and SU(6) are ongoing. SU(5) and SU(6) Heisenberg models are especially interesting for the emergence of many complicated orders, or quantum phases.

The calculation supports MPI parallelization, and suitable for a large-scale computation in the ISSP supercomputers.

References

[1] J. Q. Chen: Group representation theory for physicists (2nd edition) (2002).